Faculty of Civil and Industrial Engineering
Department of Civil, Constructional and Environmental Engineering
Geodesy and Geomatics Division
Ph.D. Course in Infrastructures and Transport
Cycle XXXII

New applications and opportunities of GNSS meteorology

Candidate: Alessandra Mascitelli

Advisor: Mattia Giovanni Crespi
Co-advisors: Stefano Dietrich
Stefano Federico
Augusto Mazzoni

Rome, February 2020

Conosco un posto nel mio cuore
dove tira sempre il vento;
non c'è niente da capire,
basta sedersi ed ascoltare.

Lucio Dalla – *Cara*

Contents

Contents **v**

List of Figures **ix**

List of Tables **xv**

Acronyms **xvii**

Abstract **1**

1 Introduction **3**

2 Atmosphere **7**

2.1 Physics of the atmosphere 7
2.2 Vertical structure 10
2.3 Optical properties and Atmosphere Remote Sensing . . 11
2.4 Chemical composition 14
2.5 Water vapor 15
2.6 Precipitation 16
2.7 Lightning 18
2.8 Numerical weather prediction models 20

3 GNSS Meteorology **23**
3.1 Fundamentals of GPS 24
3.1.1 GPS system 25
3.1.2 GPS measurements 26
3.1.3 Tropospheric refraction and delay 28
3.2 GPS permanent networks 32
3.3 GPS processing 36
3.3.1 Single-frequency data management 36
3.3.2 Bernese 5.2 47
3.3.3 RTKLIB 48
3.3.4 goGPS 49
3.3.5 Software comparison 49

4 PWV measurement sensors **53**
4.1 Radiosounding and Radiometer 53
4.1.1 Instruments 53
4.1.2 Validation test 62
4.2 Sun-sky radiometer 65
4.2.1 Instruments 65
4.2.2 Calibration and validation test 66

5 GPS assimilation **77**
5.1 GPS assimilation by 3D-var 79
5.2 Regional Atmospheric Modelling System 96

6 Near Real-Time transition **99**
6.1 Data processing 99
6.2 Data comparison 101

7 Case studies **107**
7.1 Data assimilation 107
7.1.1 Lazio Region - July 28th/September 28th, 2017 108
7.2 Extreme events data comparison 124
7.2.1 Naples - September 5th, 2015 126
7.2.2 Pineto - September 2nd, 2018 129
7.2.3 Remarks 132

8 Conclusions **135**

References **139**

Acknowledgement **159**

Ringraziamenti **161**

List of Figures

2.1 Vertical structure of atmosphere 8
2.2 SEVIRI channel 09 (IR10.8) 31 October 2003 - 11:30 UTC 13
2.3 Hydrological cycle [49] 15
2.4 Cloud classification [47] 17
2.5 Distribution of charges in a cumulonimbus [101] 19

3.1 Italian dual-frequency GPS network and single-frequency GPS pilot network 33
3.2 LOW1 Single-frequency receiver 34
3.3 LOW2 Single-frequency receiver installation 35
3.4 LOW3 Single-frequency receiver's maintenance 35
3.5 Employed dual-frequency receiver map 39
3.6 Geometry free output by "A New Ground Based Augmentation Strategy (ANGBAS)" 40
3.7 Geometry free output by the original "Satellite-specific Epoch-differenced Ionospheric Delay (SEID)" 41
3.8 Geometry free output by goSEID model 42

3.9 Dual-frequency GPS-ZTD validation by atmospheric sounding 43
3.10 Zenith Total Delay by "A New Ground Based Augmentation Strategy (ANGBAS)" 44
3.11 Zenith Total Delay by the original "Satellite-specific Epoch-differenced Ionospheric Delay (SEID)" 44
3.12 Zenith Total Delay by goSEID model 45
3.13 One day (July 25^{th}, 2016) test carried out comparing outputs (ZTD [m]) obtained by Bernese 5.2 and outputs provided by several research centres 47
3.14 Scatter plot of ZTD output from goGPS and RTKLib software, for ROUN geodetic receiver during the first week of October, 2018 50
3.15 Plot of ZTD output and differences from goGPS and RTKLib software, for ROUN geodetic receiver during the first week of October, 2018 51

4.1 Skew T–logP diagram, including wind characterization and indices, at 0000 UTC October 25^{th}, 2013 for Pratica di Mare [86]. 55
4.2 16245 LIRE Pratica Di Mare Observations at 00 12 Jun 2019; indices shown represent: Atmospheric Pressure, Geopotential height, Temperature, Dew point temperature, Relative humidity, Mixing ratio, Wind direction and speed, Potential temperature, Equivalent potential temperature, Virtual potential temperature. 56
4.3 Interpolation scheme with Natural Neighbor coordinates [96] [82] 59

4.4 Time series of differences between radiometer PWV values and GNSS PWV values 64

4.5 Boxplot of monthly differences between radiometer PWV values and GNSS PWV values 64

4.6 POM-01 Sky Radiometer 66

4.7 Behaviour of the estimated calibration parameters compared to PWV (for the sake of brevity W in plots) classes. The errors bars are the errors affecting the parameters as evaluated using a Monte Carlo method . . 71

4.8 Scatter plot of $PWV2_{GPS}$ and PWV_P (for the sake of brevity WGPS2 and WP in plots). Alternations of black and greys indicate the three water vapor classes 75

5.1 The water vapor mixing ratio (q) and temperature (T) given by the RAMS model (background) are adjusted according to the assimilation of the GPS-ZTD with the purpose of improving the representation of the humidity and temperature fields. 80

5.2 The model and analysis horizontal grids. The thick lines show the analysis grid, while the thin lines show the native model grid. The analysis can be performed on a reduced grid 81

5.3 Graphic representation of the operational phases . . . 85

5.4 Example transformation grid 87

5.5 B_h matrix 91

5.6 $\sigma - z$ relation for the water vapor mixing ratio 94

6.1 12h moving window, which shifts one hour by one, working in batch 100
6.2 Simplified data acquisition scheme 101
6.3 South Africa - Receivers location 102
6.4 Peak smoothing in subsequent processing 103
6.5 No smoothed peaks in subsequent processing 103
6.6 Statistics NRT GPS ZTD - PP GPS ZTD 104
6.7 Statistics PPMW GPS ZTD - PP GPS ZTD 104

7.1 Comparison between ZTD estimation by ROUN and ZTD from EUREF official estimation of M0SE 110
7.2 Comparison between single frequency receivers output during the whole period processed by RTKLIB (top) and goGPS (bottom) 111
7.3 Comparison between ZTD from geodetic receiver (ROUN) and ZTD from single frequency receiver (LOW1) 112
7.4 Domains of R10 (D1), R4 and R4_ ANL (D2) forecasts 113
7.5 Temporal scheme of the simulations. At 6 UTC of each day a 9 h forecast is performed (R4), using the R10 forecast as initial and boundary conditions. At 12 UTC an analysis is made and a short-term forecast (3 h) starting from this analysis is performed (R4 _ ANL) 113
7.6 Comparison between the background (Figure 7.6(a)) and analyses (Figure 7.6(b)) with the observations of the LOW1 receiver. For this experiment none of the single frequency receivers were assimilated 117

7.7 (a) RMSE of the ZTD for the background (R4) computed over the whole period; (b) as in (a) for the analysis (R4_ ANL); (c) RMSE of the IWV for the background (R4) computed over the whole period; (d) as in (c) for the analysis (R4_ ANL). 118
7.8 (a) Correlation between the background and the observations for ROUN for ZTD; (b) as in a) for the analysis; (c) correlation between the background and the observations for ROUN for IWV; (d) as in (c) for the analysis 119
7.9 Time series of the R4, R4_ ANL and observations (OBS) for ZTD (Figure (a)), IWV (Figure (b)) and for the differences between R4 and observations and between R4_ ANL and observations for ZTD (Figure (c)) and IWV (Figure (d)) 121
7.10 Time series of the differences between R4 and observations and between R4_ ANL and observations for ZTD (Figure (a)) and IWV (Figure (b)). Verification at 1 hour forecast 122
7.11 Overview on Naples - September 5^{th}, 2015 09:12 UTC; brightness temperature and strokes 126
7.12 comparison between the IC/CG ratio evaluated over the $1°\times1°$ box centred on GPS receiver and the total strokes detected during the storm 128
7.13 Relationship between ZTD, TB and strokes 128
7.14 Overview on Pineto - September 2^{nd}, 2018 event; brightness temperature and strokes 130
7.15 Overview on Pineto - September 2^{nd}, 2018 event; brightness temperature and strokes 131

7.16 Relationship between ZTD, TB and strokes 131

List of Tables

2.1 International Standard Atmosphere, Mean Sea Level Conditions 11
2.2 Chemical composition of the atmosphere 14

3.1 GF Standard Deviation values related to the different methods applied 42
3.2 ZTD Standard Deviation values related to the different methods applied 46
3.3 Bernese ZTD output statistical analysis [m] 48
3.4 Differences statistical analysis 51

4.1 Statistics of the comparisons between PWV values derived from different sources, in terms of minimum (min) and maximum (max) differences, mean difference (mean) and standard deviation (std) 63

5.1 Statistical indices 83

7.1 Statistics related to the difference between goGPS and RTKLIB results 110
7.2 List of physical parameterizations used for RAMS . . . 115

7.3 Basic parameters of the RAMS (R10, R4) grids. NNXP is the number of grid points in the WE direction, NNYP is the number of grid-points in the SN direction, NNZP is the number of vertical levels, DX is the size of the grid spacing in the WE direction, DY is the grid-spacing in the SN direction. L_x, L_y, and L_z are the domain extensions in the NS, WE, and vertical directions. CENTLON and CENTLAT are the coordinates of the grid centres. D1 refers to the first RAMS domain, D2 to the second domain 123

7.4 Bias, MAE and RMSE for the analysis and for the three hours of forecast. Statistics are computed for the whole period and are shown for ZTD (Table upper part) and for IWV (Table lower part) 124

Acronyms

AERONET	AErosol RObotic NETwork
AIUB	Astronomical Institute of the University of Bern
ANGBAS	A New Ground Based Augmentation Strategy
APs	Application Programs
ASI	Italian Space Agency
BEK	Bayerische Akademie der Wissenschaften
BNC	Bkg NTRIP Client
CAPE	Convective Available Potential Energy
CDDIS	Crustal Dynamics Data Information System
CINH	Convective Inhibition
CODE	Center for Orbit Determination in Europe
CG	Cloud to Ground
EKF	Extended Kalman Filter

EUR	EUREF
GEO	Geosynchronous Equatorial Orbit
GF	Geometry-Free combination
GLONASS	GLObal'naja NAvigacionnaja Sputnikovaja Sistema Russian Global Navigation Satellite System
GNSS	Global Navigation Satellite System
goSEID	SEID approach integrated in goGPS open source software
HD	Hydrostatic Delay
HEO	Highly Elliptical Orbit
HRV	High-Resolution Visible
IC	Intra Cloud
ICAO	International Civil Aviation Organization
IGS	International GNSS Service
ILWC	Integrated cloud Liquid Water Content
IWV	Integrated Water Vapor
IR	InfraRed
IRNSS	Indian Regional Navigation Satellite System
ISA	International Standard Atmosphere

LEO Low Earth Orbit

LINET LIghtning detection NETwork

MEO Medium Earth Orbit

MSG Meteosat Second Generation

MSL Mean Sea Level

NAVSTAR GPS NAVigation Satellite Timing and Ranging Global Positioning System

NIR Near InfraRed

NMAD Normalized Mean Absolute Deviation

NMC National Meteorological Center

NN Natural Neighbours

NWP Numerical Weather Prediction

NRT Near Real Time

NTRIP Network Transport of RTCM data over IP

OOP Object Oriented Programming

PWV Precipitable Water Vapor

PP Post Processed

PPMW Post Processed Moving Window

PPP Precise Point Positioning

RAOBS RAdiosond OBServation

RMSD Root-Mean-Square Deviation

RMSE Root-Mean-Square Error

QZSS Quasi-Zenith Satellite System

RAMS Regional Atmospheric Modeling System

RINEX Receiver INdependent EXchange format

RT Real Time

RTAC Real Time Analysis Centers

RTS Real Time Service

SEID Satellite-specific Epoch-differenced Ionospheric Delay

SEVIRI Spinning Enhanced Visible and InfraRed Imager

SINEX Solution INdependent EXchange format

STD Slant Total Delay

TB Brightness Temperature

TD Tropospheric Delay

TOA Time Of Arrival

UV UltraViolet solar radiation

VSF Very Short-term Forecast

WD	Wet Delay
ZHD	Zenith Hydrostatic Delay
ZWD	Zenith Wet Delay
ZTD	Zenith Total Delay
3D-Var	Three-Dimensional VARiational data assimilation system
4D-Var	Four-Dimensional VARiational data assimilation system

Abstract

Water vapor content of the atmospheric low layer, up to about 18 km, known as troposphere or neutral atmosphere, affects GNSS (Global Navigation Satellite System) signals by lowering their propagation velocities with respect to vacuum. A diminished speed results in a time delay in the signal propagation along the satellite-receiver path, that multiplied by the vacuum speed of light adds an extra-distance to the satellite-receiver geometrical one. This delay defines a parameter which takes the name of Tropospheric Delay (TD) and consists of an Hydrostatic (HD) and a Wet (WD) part. Anyway, if from the positioning point of view this delay is just a systematic error to be removed, it puts forward GNSS as a tool for the remote sensing of the troposphere water vapor content.

The role of GNSS in meteorology is rapidly increasing; water vapor plays a crucial role in atmospheric processes that act over a wide range of temporal and spatial scales, from global climate to micrometeorology [16] and GNSS data can be extremely useful for the purpose of a multi-instrumental investigation; indeed it was used to calibrate and validate other instruments [26] or methodologies [87], but probably

one of the most impactful application is related to the assimilation of GNSS data into the meteorological models [8] [42] [19].
In this study, a global analysis of the role of the GPS data in the field of meteorology was carried out. A focus was kept on the assimilation of data in NWP Models, also according to the cooperation with the Institute of Atmospheric Sciences and Climate of National Research Council of Italy, which included this work in the frame of a collaboration with the Department of Italian Civil Protection.
The main aim of this thesis is to find parameters able to support the analysis and forecast of intense meteorological events.
To do this, a comparative analysis was carried out between GPS outputs and other Precipitable Water Vapor (PWV) measurement instruments; results show great consistency between the data (St. Dev.$\approx$1cm).
Another test was performed on the assimilation in NWP Models, in particular RAMS Model; in this case it has been found a noticeable impact (20-30% improvement) on ZTD and IWV for short term forecast.
As for the Near Real Time (NRT) processing, results obtained are encouraging with a St. Dev.$<$ 1cm with respect to post-processing (PP).
To sum up, results provide an overall assessment of the data quality obtained through GPS post-processing and a milestone for NRT processing, also in view of early warning systems.

Chapter 1

Introduction

"If you want to see valleys, climb to the top of a mountain;
if you want to see the peak of a mountain, go up a cloud;
if instead you aspire to understand clouds, close your eyes and think."

Kahlil Gibran

The main topic of this thesis is the analysis of the support that innovation in GNSS technology can provide in the field of meteorology.
GNSS signal, along its satellite-receiver path, is affected by a multitude of effects. These effects, which from the point of view of positioning are cause of disturbance, are also a source of a considerable amount of information.
One of these effects, known in literature as tropospheric delay, provides interesting information about the state of the tropospheric layer.
Troposphere, the region of the atmosphere that extends from the ground up to 7-18 km [6], is the site of typical weather phenomena, such as

clouds and precipitation and it is therefore the atmospheric layer characterized by the presence of water vapor.

In this study, GNSS is proposed as a tool for measuring the tropospheric content of water vapor [16] [15] [4] [100] [21] [66]; observations from permanent stations can indeed provide important information for the analysis of water vapor and the investigation on the enhancement of weather forecasts and on possible climatic variations [92] [2] [106] [94].

Since more than 25 years, the meteorological community has begun to consider this high-precision positioning by-product as one of the available observations for the analysis of water vapor content data in the troposphere and in this sense a mixed community of meteorology and GNSS experts has explored a dedicated use of GNSS for the tropospheric survey [20] [52] [116].

At present, the study of water vapor through GNSS can be routinely performed by existing permanent networks of geodetic receivers, distributed over the territory for other purposes; these receivers are generally dual frequency (L1/L2), GPS only or multi-constellation GNSS (GPS, GLONASS, Galileo, Beidou).

The observations collected by these regional/national networks are often published on the web and can be used to determine time series of water vapor, sometimes assimilated in weather forecasts by means of numerical models.

However, the high variability of water vapor [78], both in space and time, requires very dense networks with homogeneous distribution in order to map water vapor in high resolution, also suitable for local level forecasting.

The collection of water vapor observations plays an important role in

improving the prediction of the occurrence of convective phenomena and precipitation [118]; therefore the distribution of a dense network of GNSS receivers could be a powerful support in improving the accuracy of analysis and predictions during convective events [110], in particular on areas where observations are otherwise scattered.
The expected impact in assimilating water vapor observations into a high-resolution model is to locally improve the initial moisture fields in convective precipitation regimes.
As far as the type of involved receivers, it was thereby decided to use both geodetic and single-frequency class receivers which, due to their low cost, are well suited to mass distribution in the territory, and therefore to establish dense permanent networks [120].
The research was therefore structured on several fronts:

- Installation and analysis of data provided by the pilot permanent network of single-frequency GNSS receivers located in Rome (Chapter 3)
- GPS data assimilation in numerical weather prediction models (NWP) (Chapter 5/ Chapter 7)
- Near real time data processing and evaluation of results (Chapter 6)
- Use of GPS data for calibration and validation of estimates obtained by other instruments (e.g. radiosounding, radiometer/photometer, Linet network) (Chapter 4/ Chapter 7)

In order to reach the established goals, different software and programming languages were used.

Data from GNSS receivers were processed using renown software (i.e. Bernese, RTKLIB) and a more recently published software (i.e. goGPS), in order to evaluate any analogies/differences, whereas all statistical analysis were performed by Python or Matlab dedicated tools.

Chapter 2

Atmosphere

2.1 Physics of the atmosphere

Atmospheric science deals with structure and evolution of the planetary atmospheres and with the wide range of phenomena that occur within them [6]. As for the Earth, the atmosphere is split into separate layers according to the trend of the vertical temperature profile and according to particular physical or chemical phenomena that characterize it. The use of the vertical temperature gradient is fundamental both because it identifies layers of atmosphere with different characteristics, and because it is a fundamental parameter for hydrostatic equilibrium. In the classification based on temperature profile, four basic layers are identified: troposphere, stratosphere, mesosphere and thermosphere.

Troposphere is the layer of atmosphere closest to the Earth's surface and has an average vertical extension of up to 7-18 km. It is affected by a constant decrease in temperature with altitude, on an average basis of 6.5 $°C/km$. This decrease is due to both the fact that an air

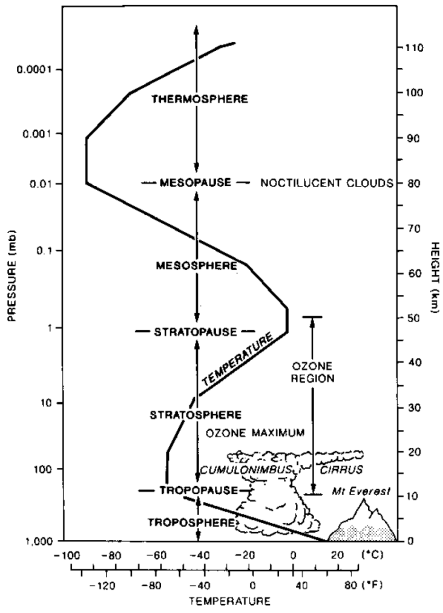

Fig. 2.1: Vertical structure of atmosphere

particle expands adiabatically rising and that the main source of heat is represented by the ground, which consequently heats intensively layers of air close to it. Indeed, the Earth's surface heats up absorbing solar radiation and the heat re-emitted by the Earth is transported upwards thanks to the convection, which characterizes the troposphere. Troposphere contains almost 80% of the total mass of the atmosphere and contains practically all of the atmospheric water vapor; as a result, troposphere is the area where meteorological phenomena occur. Troposphere vertical extension varies greatly with latitude; it is 7-8 km thick above the poles, 10-12 km at mid-latitudes and 16-18 km in tropical regions where the strong warming of the soil promotes intense convective movements that penetrate upwards [6]. Troposphere is lim-

ited above by a thermal inversion that acts as a proper margin limiting the vertical extension of convective motion.
Tropopause separates troposphere from stratosphere.
Stratosphere is characterized by a first layer about 10 km thick in which the temperature is almost constant with the altitude and by a subsequent 25-30 km, in which the temperature increases gradually. Due to the positive vertical temperature gradient, vertical mixing is strongly inhibited, unlike in the troposphere. Stratosphere contains almost all of the atmospheric ozone (about 90% of the total) that absorbs the ultraviolet solar radiation (UV) producing a warming-up.
Stratopause, in which the maximum stratospheric temperature is reached, separates stratosphere from the upper layer, the mesosphere.
Mesosphere extends up to about 80 km of altitude and in it the temperature drops with the height up to the minimum (around -130°C), at the mesopause. Stratospheric ozone layer performs the same function towards the mesosphere that the Earth's surface has for the troposphere: it heats the lower layer generating a negative temperature profile. At mesopause the temperature drop is interrupted due to the warming produced by the absorption of solar radiation by molecular oxygen and ozone.
Thermosphere extends in height for several hundred kilometers and is characterized by significant temperature fluctuations between day and night. Indeed, temperature in thermosphere is closely linked to the intensity of solar radiation and its constant increase with altitude is due to the absorption of the same solar radiation by nitrogen and oxygen molecules dissociating. Above 100 km altitude, cosmic radiation also produces the ionization of atoms, tearing off electrons and leaving ions; this is the basis of the formation of the visible aurora borealis, in

particular conditions, at high latitudes [6].
In any case, the characterization of these layers depends on the purpose for which the subdivision is made; indeed, characterizing the atmosphere by the way radio waves are propagated leads to a subdivision of a troposphere and ionosphere. The *ionosphere*, the upper part of the atmosphere, is a dispersive medium (the propagation delay is frequency dependent), whereas the *troposphere* is nondispersive [64].

2.2 Vertical structure

With a reasonable approximation, the air density at sea level is $1.25 Kg/m^3$ and pressure p and density ρ decrease almost exponentially with altitude:

$$p \sim p_0 * e^{-z/H} \tag{2.1}$$

In the previous equation, H represents the e-folding depth, i.e. the altitude at which the pressure is reduced by a factor equal to e, while p_0 is the pressure at a reference level, usually the pressure at the sea level [64].
Pressure and density vertical variations are much more significant than horizontal and temporal changes. Therefore, it is useful to define a standard atmosphere as a function of height only, representing a horizontal and temporal average of the atmospheric structure.
The first standard atmospheric models were developed in the 1920's in both Europe and the United States. The slight differences between the models were reconciled and an internationally accepted model was introduced in 1952 by the International Civil Aviation Organization (ICAO) [105].

The International Standard Atmosphere (ISA) is defined in ICAO Document 7488/2. The ISA assumes the mean sea level (MSL) conditions as given in Table 2.1 [28]:

Tab. 2.1: International Standard Atmosphere, Mean Sea Level Conditions

Pressure	hPa	1013.25
Temperature	K	288.15
Density	Kg/m^3	1.225
Speed of sound	m/s	340.294
Acceleration of gravity	m/s^2	9.80665

2.3 Optical properties and Atmosphere Remote Sensing

The Earth's atmosphere is relatively transparent to incoming solar radiation (solar constant value of 1366.1 $W * m^2$ [51]) and opaque to outgoing radiation emitted at lower frequency by the Earth's surface [113] [55]. Much of the absorption and reemission of outgoing radiation are due to air molecules and cloud droplets; this emitted radiation provides a basis for remote sensing of various atmospheric constituents using satellite-borne sensors [6].
There are different kinds of satellites, which can be classified by their function [60]:

- Communications Satellite
- Remote Sensing Satellite

- Navigation Satellite
- Drone Satellite
- Ground Satellite
- Polar Satellite
- Nano Satellites, CubeSats and SmallSats

Another way of classifying satellites is according to their orbit; in this sense we can distinguish satellites in:

- Low Earth Orbit (LEO - altitude of 160-2000 km)
- Medium Earth Orbit (MEO - most common altitude is approximately 20000 km)
- Geosynchronous Equatorial Orbit (GEO - about 36000 km above Earth's equator)
- Highly Elliptical Orbit (HEO)

Satellites generally used in the meteorological field are GEO and LEO. These satellites are part of the wider range of remote sensing satellites, giving rise to the branch of meteorology known as "satellite meteorology".
The first European meteorological satellite (Meteosat, belonging to the first generation of weather satellites) was launched in 1977. Since then, there have been other launches and the first generation has moved on to the second generation of satellites (MSG). MSG mounts on board the SEVIRI (Spinning Enhanced Visible and InfraRed Imager) sensor,

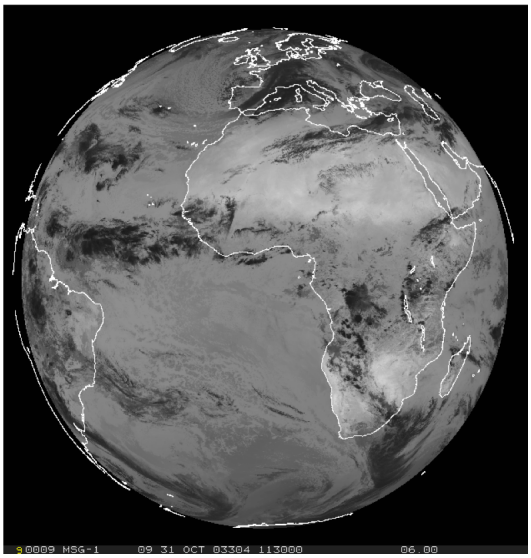

Fig. 2.2: SEVIRI channel 09 (IR10.8)
31 October 2003 - 11:30 UTC

which allows acquisition in 12 continuous cycle channels (two in the visible 0.6 and 0.8 µm; one in the NIR 1.6 µm; eight channels in the IR 3.9, 6.2, 7.3, 8.7, 9.7, 10.8, 12.0 and 13.4 µm; and the last visible in high resolution HRV). Each cycle lasts 15 minutes to acquire the entire full disk from the southern hemisphere to the northern hemisphere; 12 minutes for acquisition and the rest for calibration. Channel resolution is 3 km and 1 km for HRV. The raw data acquired by Meteosat are collected by the EUMETSAT control centre based in Germany, where they are pre-processed and redistributed [81].
They are one of the diagnostic tools from which information on weather and atmospheric conditions of large areas of the planet can be collected; they are, therefore, extremely useful in characterizing meteorological events of intense nature.

2.4 Chemical composition

Atmosphere is composed of a mixture of gases, the main components are nitrogen, oxygen and argon, which alone account for more than 99% of the volume of the entire atmosphere. In the lower part of the atmosphere the composition is almost constant, while in the upper part of the atmosphere the partial pressure of the single constituents decreases more quickly. Various elements, main and secondary, which contribute to the atmosphere, are shown in the table below.

Tab. 2.2: Chemical composition of the atmosphere

Constituent	**Molecular weight**	**volume fraction**
Nitrogen	28.013	78.08%
Oxygen	32.000	20.95%
Argon	39.95	0.93%
Water vapor	18.02	0-5%
Carbon dioxide	44.01	380 ppm
Neon	20.18	18 ppm
Helium	4.00	5 ppm
Methane	16.04	1.75 ppm
Krypton	83.80	1 ppm
Hydrogen	2.02	0.5 ppm
Nitrous oxide	56.03	0.3 ppm
Ozone	48.00	0-0.1 ppm

Troposphere contains both dry air and water vapor; dry air has no significant variation in composition with latitude and height [99], whereas the amount of water vapor varies widely, both spatially and temporally.

2.5 Water vapor

Water vapor represents about 0.25% of the atmospheric mass, but it is a highly variable component with concentrations ranging from values of 10 ppm in volume in cold or desert regions of the earth, up to 5% of the volume in hot and humid air masses. Water vapor enters the hydrological cycle and is almost entirely present in the troposphere, while only modest amounts penetrate the stratosphere. It is produced by the evaporation of oceans, seas and lakes and by the transpiration of plants and is transferred in the atmosphere through turbulent reshuffling [6].
Most of the water vapor is contained in the boundary layer, the lowest 2 km of the troposphere. Two fundamental quantities related to this

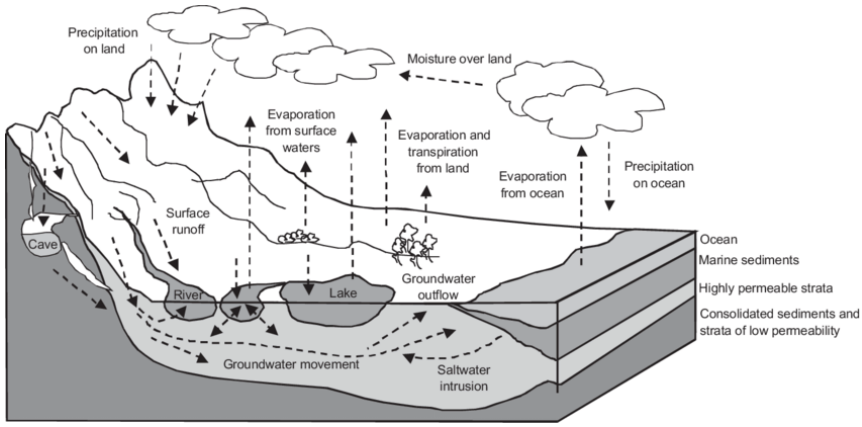

Fig. 2.3: Hydrological cycle [49]

constituent are mixing ratio and relative humidity.
Mixing ratio is a measure of moisture content and is defined as the quotient of water vapor mass per unit mass dry air [54], as explained

in the formula below [64]:

$$w = m_v/m_d = (m_v/V)/(m_d/V) = \rho_v/\rho_d \tag{2.2}$$

where w is the mixing ratio, an adimensional quantity; m_v is the water vapor mass $[kg]$; m_d is mass of dry air $[kg]$; V is the volume $[m^3]$; ρ_v is the water vapor density $[kg * m^{-3}]$ and ρ_d is the density of dry air $[kg * m^{-3}]$.
Relative humidity r_h is defined as the quotient of mixing ratio and saturation mixing ratio [64]:

$$r_h \doteq w/w_{sat} \approx e/e_{sat} \tag{2.3}$$

where r_h is the relative humidity; w is the water vapor mixing ratio; w_{sat} is the water vapor saturation mixing ratio; e is the partial pressure of water vapor $[Pa]$ and e_{sat} is the partial pressure of saturated water vapor $[Pa]$.
Water also appears in the troposphere in liquid phase (fog, clouds, rain) and solid form (snow, hail, ice), and is the most important constituent in relation to weather processes, not only because of rain and snowfall but also because large amounts of energy are released in the condensation process [64].

2.6 Precipitation

Precipitation tends to be concentrated in space and time. Annual-mean precipitation at different points on Earth ranges in almost three orders of magnitude, from some centimeters per year in dry zones to

several meters per year in the belts of heaviest rainfall [6].
Solar heating is the basis for the entire process of forming a thunderstorm, it heats the Earth's surface, which in turn transfers heat via radiation to the air layers close to the ground. Heating the air molecules in the lower layers of the atmosphere increases the molecular excitement, so the air expands and becomes less dense and lighter than the surrounding air. These air molecules tend, therefore, to rise upwards and the atmospheric pressure, decreasing with altitude, favours the further expansion of the air particle. Expansion involves cooling. The saturation vapor pressure of the water decreases with decreasing temperature, so, as the air particle cools, the humidity in it tends to condense. This mechanism gives rise to a multitude of microscopic droplets of water that together generate clouds. If the air particle does

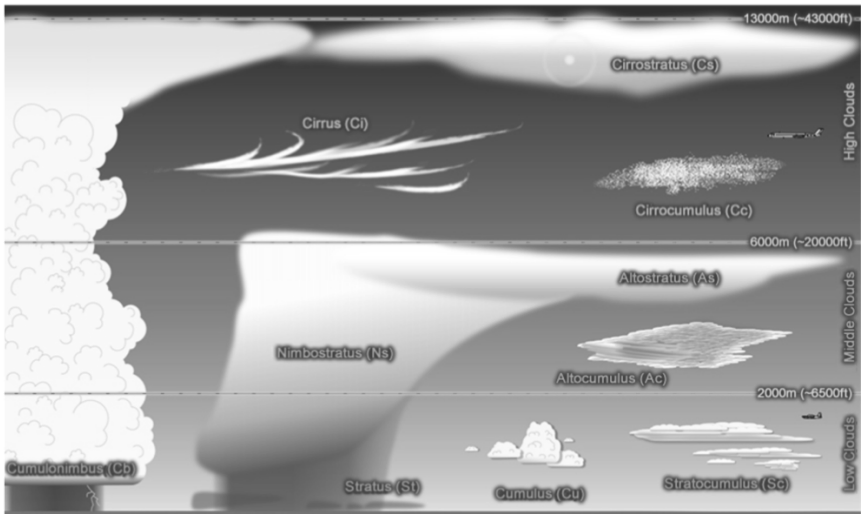

Fig. 2.4: Cloud classification [47]

not contain saturated humidity and the adiabatic condition is assumed

to be true, its temperature drops by 10 °C per kilometre of ascent. This thermal gradient is called dry adiabatic. However, under normal conditions the atmospheric temperature does not decrease so rapidly with altitude and the air particle becomes colder than the surrounding air, stopping it from rising.
If the air particle contains moisture, the heat is released as condensation and the particle continues to rise. Under these conditions, the air temperature decreases by about 5.5 °C per kilometre and is referred to as a wet adiabatic gradient. If the temperature of the atmosphere decreases faster than the humid adiabatic, the particle will continue to rise because it will remain warmer than the surrounding air and the necessary condition for the creation of the thunderstorm will be met. Such an atmosphere is called conditionally unstable.
The ability of the atmosphere to generate thunderstorms is measured by the amount of potential energy available for convection (CAPE). Generally, a CAPE greater than 1500 $J * kg^{-1}$ is considered as generating a high risk for the formation of thunderstorms [81].

2.7 Lightning

There are several theories proposed to explain how the generation of electric charge occurs within the cumulonimbus [30]. However, the most widely accepted theory is based on the collision of graupels (ice particles with a density varying between 0.1 and 0.8 $g * cm^{-3}$) in the presence of drops of overflowing water in the cloud. The theory is based on experiments [102] [61] in which a graupel particle launched at a certain speed inside a cloud of ice crystals and overflowing water

droplets was simulated. During the collisions, the generated charge was measured. Observations reveal that the intensity and polarity of the charging process depend on the water content in the cloud and the ambient temperature [81].

A thunderstorm cloud contains two main charge centers, one positive and one negative, and a third positive center of lower intensity placed at the base of the cloud. A cloud to ground (CG) lightning occurs between a charge center and the ground, and the result is the transfer of charge from the cloud to the ground. When a CG carries positive

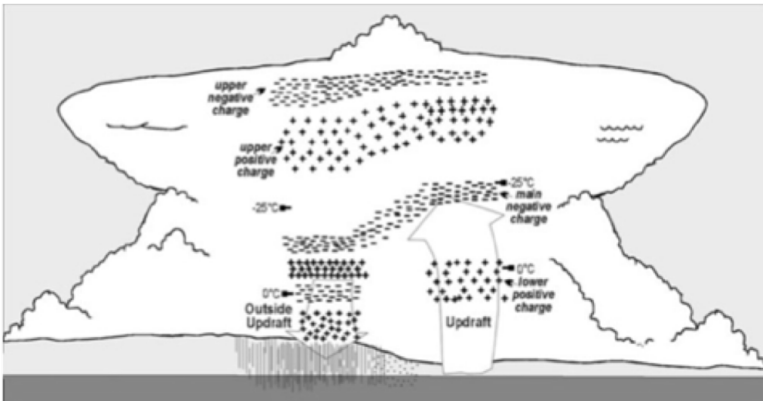

Fig. 2.5: Distribution of charges in a cumulonimbus [101]

charge to the ground it is called positive, vice versa it is called negative. Therefore, the type of CG identifies not only the charge transported but also the origin of the lightning itself.

Instead, the term intra cloud lightning (IC) generally refers to lightning strikes that occur between the main negative charge center and the positive charge center of the cloud; the result is a partial neutralization of the charge centers themselves [81].

A relevant network of lightning detectors is the LINET (LIghtning

detection NETwork) [13]. It was developed by the University of Munich in 2006 and it is composed by about 130 sensors that ensure a minimum distance of 200-250 km in 17 European countries [11].

2.8 Numerical weather prediction models

The most suitable definition to understand the meaning of NWP Models is that provided by Kalnay in 2003: "NWP is an initial/boundary value problem: given an estimate of the present state of the atmosphere (initial conditions), and appropriate surface and lateral boundary conditions , the model simulates (forecasts) the atmospheric evolution. The more accurate the estimate of the initial and boundary conditions, the better the quality of the forecasts" [62].

Data assimilation

Currently, operational NWP centers produce the state of atmospheric flow through a statistical combination of observations and short-range forecasts [62]. This approach is known as "data assimilation" and its purpose is defined as "using all the available information, to determine as accurately as possible the state of the atmospheric (or oceanic) flow" [104].
At present, there are different kinds of data available, including satellite data, radar observations, data from lightning networks and GNSS (Global Navigation Satellite Systems) observations; in any case, before proceeding to the assimilation it is necessary to have an as complete as possible first guess estimate of the state of atmosphere at all the grid points in order to generate the initial conditions for the forecasts

[10]. The first guess, also known as background field, should be the best estimate of the state of the atmophere prior to the use of the observations [62].
In chapter 5 a complete analysis of GPS-ZTD data assimilation is described and some tests and results are given in chapter 7, in order to explain the potential impact of GPS data assimilation on forecasts.

Chapter 3

GNSS Meteorology

The acronym GNSS (Global Navigation Satellite Systems) defines all the constellations of artificial terrestrial satellites for positioning and navigation. Today, this system is used in many fields, ranging from real-time navigation, with accuracy requirements of several meters, to geomatic and geodetic applications, which require accuracy from the decimeter to the best of one centimeter [17].
There are several projects, carried out by different countries, of systems of GNSS-based positioning; the first one to be born was the NAVSTAR GPS project (NAVigation Satellite Timing And Ranging Global Positioning System) by United States Department of Defense, but other GNSS constellations like GLONASS (GLObal'naja NAvigacionnaja Sputnikovaja Sistema - Russia), GALILEO (Europe), QZSS (Japan), BeiDou Satellite Navigation and Positioning System (China) and IRNSS (Indian Regional Navigational Satellite System) appeared later than GPS.
Anyway in this thesis we will refer exclusively to the GPS constellation,

considering its use a well-established topic for the treated applications.

3.1 Fundamentals of GPS

"The Global Positioning System was conceived as a ranging system from known positions of satellites in space to unknown positions on land, at sea, in air and space" [57].
The NAVSTAR GPS project (NAVigation Satellite Timing And Ranging Global Positioning System) is the result of a project launched in the 1973 by the Department of Defense of the United States of America, with the aim of enabling real-time positioning of military assets; indeed, in 1985, this definition of GPS project was given by W. Wooden: "The Navstar Global Positioning System (GPS) is an all-weather, space-based navigation system under development by the Department of Defense (DoD) to satisfy the requirements for the military forces to accurately determine their position, velocity, and time in a common reference system, anywhere on or near the Earth on a continuous basis."
In any case, although the primary goals were military, in the following years also the civil use was promoted [57].
The first satellite of GPS constellation was launched in 1978 and after a gradual development of the project in the following years, in 1995 it was officially declared fully operational and since then, real-time navigation is supposed to be guaranteed h24 everywhere on or near the Earth [17].

3.1.1 GPS system

The GPS system consists of three segments that allow it to function correctly. The first one is the space segment which is composed of a nominal minimum constellation of twenty-four satellites, arranged on six orbital planes. The geometry of the constellation guarantees the simultaneous visibility of at least four satellites from every point on Earth. The main functions of this segment are to provide information to users by means of signals, to receive and store the information sent by the control segment and to maintain an accurate time signal by means of four atomic oscillators placed on board each satellite. The second one is the control segment which consists of five ground stations, whose position is known with extreme precision; these are named Monitor Stations and continuously track satellites. The Master Control Station in Colorado Springs (U.S.A.) is the main control station, where all data recorded in the Monitor Stations are merged and processed, whereas the Ground Control Stations (Ascension, Diego Garcia and Kwajalein) are the connection between the Master Control Station and the space segment. The user segment, consisting of each user, civil and military, equipped with a receiver capable of capturing, decoding and processing the signal transmitted by the satellites [57].
GPS signal is rather complex. The oscillators on board the satellites generate a continuous electromagnetic signal with nominal frequency f_0=10.23 MHz; from f_0 two sinusoids, L_1 (1575.42 MHz) and L_2 (1227.6 MHz) carrier, are generated [17].
The L1 and L2 carriers are modulated using binary codes (pulse sequences with values +1 and -1): C/A (Course Acquisition Code), L2C (L_2 Civilian-Transmitted only by IIR-M Block satellites and public),

P(Y) (EncrYpted Precise Code), M (Encrypted military code transmitted on both carriers) and D (Data). Binary codes are called Pseudo Random, because their impulses are similar to random signals, as for time correlation properties [67].
The Coarse/Acquisition (C/A) code and the precision (P) code modulate the L1 signal. The L2 signal is modulated by the P-code only. To prevent spoofing of P-code signals, an encrypted code W (not available to civilian users) is modulated by the Department of Defense with the publicly known P code on both L1 and L2 to provide the anti-spoofing Y-code. Since L2, unlike L1, does not have the C/A code, its access is denied to all users without knowledge of the W-code; nevertheless there are some techniques that can be used to reconstruct the L2 carrier without knowledge of the W-code, which allow the civilian use [117].
The navigation message D, sent with the pseudo-random codes, is used to communicate the satellite ephemeris, satellite clock offset parameters, parameters for ionospheric disturbance modelling (Klobuchar) and approximate orbital information for the other satellites in the constellation [17].

3.1.2 GPS measurements

The signal coming from the satellites is picked up by the receiver, which makes a replica inside by means of its oscillator; the signal thus reproduced will differ from that received because of a phase shift along the time axis. The GPS signal reception presents the possibility to carry out two different measurement modes: pseudorange measurements (Eq. (3.1)) and phase measurements (Eq. (3.2)).
Pseudorange observation equation and phase observation equation have

the following simplified analytical form:

$$P_R^S(t) = \rho_R^S(t) + c(dt_R(t) - dt^S(t)) + I_R^S(t) + T_R^S(t) \tag{3.1}$$

$$L_R^S(t) = \rho_R^S(t) + c(dt_R(t) - dt^S(t)) - I_R^S(t) + T_R^S(t) + \lambda(N_R^S(t) + \phi_R - \phi^S) \tag{3.2}$$

In both the equations, ρ_R^S is the geometric distance:

$$\rho_R^S = \sqrt{(X_R - X^S)^2 + (Y_R - Y^S)^2 + (Z_R - Z^S)^2} \tag{3.3}$$

in which X^S, Y^S and Z^S are the satellite cartesian coordinates at the observation time, known by ephemeris, and X_R, Y_R and Z_R are the receiver cartesian unknown coordinates at the observation time.
c is the light speed, $dt^S(t)$ is the satellite clock offset, known from the navigational message and $dt_R(t)$ is the receiver clock offset, considered unknown.
Phase observation equation reminds pseudorange observation equation but in this last case appears one more unknown, $N_R^S(t)$, the integer ambiguity which depends on the satellite-receiver optical path. There are also initial fractional phases ϕ_R and ϕ^S, both constant and unknown.
$I_R^S(t)$ and $T_R^S(t)$ represent the atmospheric disturbances; indeed in the Earth's atmosphere, the signal propagation speed changes due to the physical state of the medium which is crossed.
Ionospheric delay is due to the layers of atmosphere between 100 km and 1000 km of altitude, where there are ions and free electrons that interfere with the GPS signal propagation. As it can be seen from the above equations (Eq. (3.1) and Eq. (3.2)), there is a change of sign; in fact, the group speed decreases while the phase speed increases, consis-

tent with the fact that it is a dispersive medium, unlike the troposphere [17].
It is important to remember that the ionospheric disturbance presents great variability; it can be mathematically described by synthetic models, e.g. Klobuchar [65], or removed by Ionospheric Free combination. Tropospheric delay is due to the layers between the ground and 7-18 km above sea level and is basically caused by the presence of gas and water vapor. It will be described in detail below.

3.1.3 Tropospheric refraction and delay

Dry air and water vapor molecules in the troposphere affect GNSS signals by lowering their propagation velocities with respect to vacuum [88] [16]. A diminished speed results in a time delay in the signal propagation along the satellite–receiver path, which multiplied by the vacuum speed of light, adds an extra distance to the satellite–receiver geometrical one. It is worth reminding here that the tropospheric delay due to the dry air and water vapor molecules is just one out of many other systematic errors affecting GNSS observations that must be accounted for in order to achieve sub-centimetre accuracy positions. Local refractive index along the propagation direction of the signal is [17]:

$$n(r) = 1 + k_1 \frac{P(r)}{T(r)} + k_2 \frac{e(r)}{T(r)} + k_3 \frac{e(r)}{T^2(r)} \tag{3.4}$$

where $P(r)$ is the pressure expressed in $mbar$, $T(r)$ is the temperature expressed in K, e is the partial pressure of water vapor expressed in $mbar$ and constants are listed below: $k_1 = 77.624 * 10^{-6}[K * mbar^{-1}]$ $k_2 = -12.920 * 10^{-6}[K * mbar^{-1}]$ $k_3 = 37.19 * 10^{-2}[K^2 * mbar^{-1}]$.

Integrating it is possible to obtain:

$$T_R^S = \int_{Tropo_R^S} (k_1 \frac{P(r)}{T(r)} + k_2 \frac{e(r)}{T(r)} + k_3 \frac{e(r)}{T^2(r)})\, dr = \tag{3.5}$$

$$T_R^S = \int_{Tropo_R^S} k_1 \frac{P(r)}{T(r)}\, dr + \int_{Tropo_R^S} (k_2 \frac{e(r)}{T(r)} + k_3 \frac{e(r)}{T^2(r)})\, dr \tag{3.6}$$

Where the first integral represents the 90% of the total delay and is named *dry component*, and the second one represents the 10% of the total delay and is the most variable fraction named *wet component*. During GNSS data processing it is possible to model the tropospheric delay by models based on hypotesis of standard atmosphere, e.g. Saastamoinen [88], or to use this delay as source of information.
In the first case, under adverse conditions, the residual error may reach values of up to 10% of the total disturbance; despite the fact that the introduction of less used methods such as Niell's has led to improvements [17].
In the second case, contributions of dry air and water vapor to the total delay are separated and estimated [59].
Basically two products are provided for meteorological applications: the slant total delay (STD, i.e. T_R^S), which is the signal delay along each single signal path, and the zenith total delay (ZTD), that is the delay related to the zenith direction, obtained after introducing a mapping function which depends on physical parameters (isotropy assumption to determine the azimuthal symmetric slant delay) [64] [57] [7] [77]. This last parameter leads to the definition of the two delay components: ZHD (zenith hydrostatic delay) and ZWD (zenith wet delay),

related by the equation:

$$ZTD = ZHD + ZWD \tag{3.7}$$

[16]. If from the positioning point of view this delay was just a systematic error to be removed, it suggests GNSS as a tool for the remote sensing of the troposphere water vapor content. The meteorological community considers this by-product of high-accuracy positioning as one of the available observations and time series of GNSS tropospheric water vapor delays can be assimilated into numerical weather prediction models also in a routine way [8] [50].
Starting from meteorological data of pressure and temperature, after appropriate adjustments related to the difference in altitude between meteorological sensors and GPS receivers [85] [9] [5], it is possible to obtain ZWD values, from ZTD values.
Below is given the equation for *pressure* adjustment [9]:

$$P_{GPS} = P_{Sensor} exp(-\frac{gM_d(H_{GPS} - H_{Sensor})}{R^* T_{ISA}}) \tag{3.8}$$

where P_{GPS} and P_{Sensor} are respectively the pressure value adjusted at GPS height and the pressure value measured by the meteorological sensor; $g = 9.80665\ m\ s^{-2}$ is the gravitational acceleration constant, $M_d = 0.0289644\ kg\ mol^{-1}$ is the molar mass of dry air, $R^* = 8.31432\ J\ mol^{-1}\ K^{-1}$ is the gas constant for air, and $T_{ISA} = 288.15K$ is the international standard temperature of the atmosphere at sea level. H_{GPS} and H_{Sensor} are the orthometric heigths [m] of GPS receiver and meteorological station, respectively.

The equation for *temperature* adjustment is shown below [5]:

$$T_{GPS} = T_{Sensor} + 0.0065(H_{Sensor} - H_{GPS}) \tag{3.9}$$

where T_{Sensor} and T_{GPS} are respectively the temperature [K] measured by meteorological sensor and that inferred at the GPS station, whereas H_{Sensor} and H_{GPS} are the orthometric heights of the two stations [m]. The following procedure [16] allows calculating the ZHD and consequently the ZWD, taking into account the variation in gravitational acceleration with latitude φ, and the height h above the ellipsoid [km], by the sufficiently approximated formula [41]:

$$f(\varphi, h) = 1 - 0.00266cos2\varphi - 0.00028h \tag{3.10}$$

At this point it is possible to obtain the ZHD [mm] by the following formula where $Patm$ is the total pressure [mbar] at the Earth's surface.

$$ZHD = 2.2779Patm/f(\varphi,h) \tag{3.11}$$

It is now possible to get ZWD by difference:

$$ZWD = ZTD - ZHD \tag{3.12}$$

Finally, it is possible to obtain the amount of IWV (integrated water vapor)[4]:

$$IWV = K(Tm)ZWD \tag{3.13}$$

where the coefficient K depends on the vertically integrated mean temperature (Tm) [34], following the formula below:

$$1/K = 10^{-6}(K_3/Tm + K_2')Rv \tag{3.14}$$

where $K_3 = 3.776{*}10^5 K^2 mbar^{-1}$, $K_2' = 17 K mbar^{-1}$, $Rv = 461.5 Nm/KgK$ and Tm can be obtained in different ways, in this case by a linear relationships [16]:

$$Tm \sim 70.2 + 0.72Ts \tag{3.15}$$

where Ts is the measured temperature. PWV values are obtained dividing the value of IWV by the water density ($1000 Kg/m^3$).

3.2 GPS permanent networks

The great advantage of using GPS technology lies both in the reliability of the technique and in the availability of GNSS permanent networks, installed on the territory for positioning and navigation purposes. The research described here has employed various permanent networks of geodetic class receivers, both public and private:

- EUREF Permanent GNSS Network (Network of continuously operating GNSS reference stations, covering the European continent)
- RING Network (GPS National Integrated Network by National Institute of Geophysics and Volcanology)
- Abruzzo Region Permanent Network
- Lazio Region Permanent Network

- Campania Region Permanent Network
- SPIN Network (Piemonte Region and Lombardia Region)
- NetGEO Network (Network of Permanent GNSS Stations set up by Geotop)

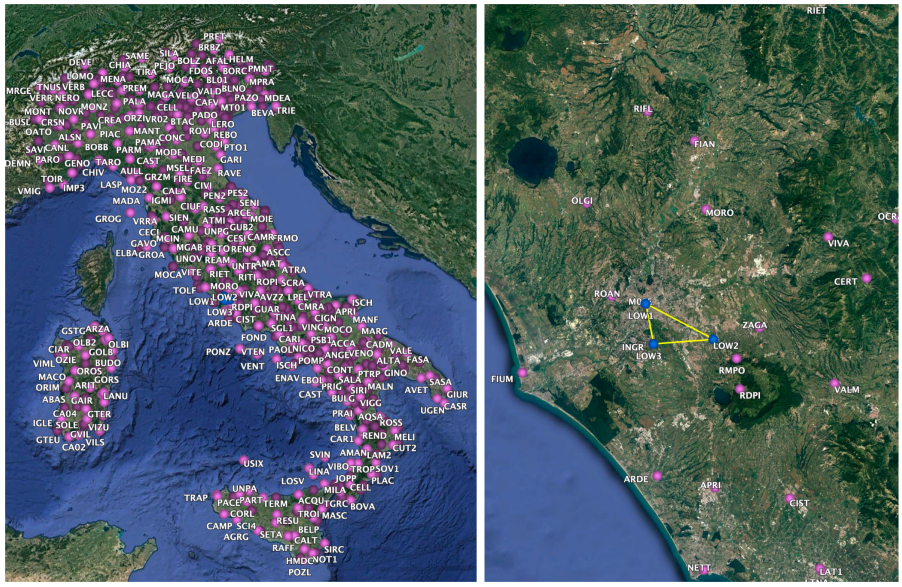

Fig. 3.1: Italian dual-frequency GPS network and single-frequency GPS pilot network

Single-frequency pilot network

As regards the pilot network of single frequency receivers, this has been installed in the hinterland of the city of Rome and consists of three stations composed by u-blox chips, MG700 M2M Wireless Gateway/ Router and antennas by Allis Communications Company (ALLISCOM). The first device is named LOW1 (Figure 3.2) and is located on the roof of Department of Civil, Constructional and Environmental Engineering, Faculty of Civil and Industrial Engineering, Sapienza University of Rome. LOW1 receiver has the great advantage to be located close to M0SE, a dual-frequency receiver belonging to EUREF Permanent GNSS Network, and close to ROUN, a dual-frequency receiver belonging to Lazio Region Permanent Network; this condition allows us to perform several high-value cross-tests. The second one is named LOW2 (Figure 3.3) and it has been installed on the roof of the

Fig. 3.2: LOW1 Single-frequency receiver

Institute of Atmospheric Sciences and Climate of National Research Council of Italy, in the Tor Vergata Research Area (ARTOV). LOW2

Fig. 3.3: LOW2 Single-frequency receiver installation

has been placed so as to be less than 15 km away from LOW1. The last one is named LOW3 (Figure 3.4) and it has been installed on the roof of the National Institute of Geophysics and Volcanology. LOW3 has been placed to complete the short basis GPS network in Rome and its data stream, together with those of LOW1 and LOW2, are managed by Geodesy and Geomatics Division, Sapienza University of Rome.

Fig. 3.4: LOW3 Single-frequency receiver's maintenance

3.3 GPS processing

Starting from the dual-frequency observational files (RINEX Version 3 format) collected by the geodetic receivers at 30 s rate, the PPP technique [121], undifferenced phase observation processing, was applied using ionosphere-free combination in order to estimate both coordinates and ZTD values for each epoch, and only ZTD values for each epoch fixing receiver's coordinates, by daily processing sessions, in order to evaluate conceivable differences. As regards the ancillary products (ephemeris and clocks), we used precise products provided by the Center for Orbit Determination in Europe (CODE) and by International GNSS Service (IGS) with the aim of assessing any potential deviations. For what concerns the software, we opted for three different software: Bernese 5.2, RTKLIB and goGPS, in order to investigate possible discrepancies.
The same procedure was followed for the three single frequency receivers, after the reconstruction of L2 synthetic observations by the New Ground-Based Augmentation Strategy [73], the Satellite-specific Epoch-differenced Ionospheric Delay [35] and the default implementation of the SEID approach integrated in the goGPS open source software (goGPS).

3.3.1 Single-frequency data management

In order to apply the data processing methodology described above also to single frequency receivers, it is necessary to use a method of synthetic L2 observations reconstruction. There are several methods for this purpose and here a comparison between three techniques is

proposed in order to evaluate the different impact on ZTD computation and to pursue a quality assessment of this reconstruction. To achieve this goal, the following three methods were applied to the M0SE, a geodetic receiver, using only one of its frequencies and compared to the reference results obtained using both its frequencies.

- *"A New Ground Based Augmentation Strategy (ANGBAS)"* developed at the Sapienza University of Rome [73].
  This algorithm computes the time variation epoch-by-epoch of the ionospheric delay for each satellite in view from a geodetic class receiver through the geometry-free linear combination to its carrier phase observations (L1 e L2). The use of a mapping function allows to project in zenith direction the ionospheric delay computed on the line of sight. In a similar way, it is possible to reconstruct the ionospheric delay for the satellites in view from a generic GNSS single frequency receiver, placed at a known distance from the considered reference station. In fact, using the mapping function allows to take in account the different path followed by the signal that, starting from the satellite, is collected by two different receivers [73].

- The original *"Satellite-specific Epoch-differenced Ionospheric Delay (SEID)"* algorithm [35].
  This algorithm involves the assumption that the epoch-differenced ionospheric delay, which determines the parameters from a minimum of three reference stations, is sufficient for ZTD estimation. The parameter estimation is performed by means of a least-squares adjustment for each satellite at each epoch resulting in a satellite- and epoch-specific plane model [35].

- The default implementation of the SEID approach integrated in the goGPS open source software (*goSEID*).
  This algorithm takes up the principles of SEID but the plane interpolation is replaced by a linear interpolation; this makes it possible to use a lower number of reference stations (even just one).

All processing was handled with the goGPS software, applying the PPP method.

Test analysis

The experiment was carried out at a local scale over Lazio Region, in Central Italy, using six geodetic receivers nearby Rome, i.e. Figure 3.5:

- M0SE from EUREF Permanent GNSS Network (Network of continuously operating GNSS reference stations, covering the European continent)

- ROUN (35 m from M0SE), RMPO (19 km from M0SE), FIUM (25 km from M0SE), VALM (38 km from M0SE) and CVTV (65 km from M0SE) belonging to Lazio Region Permanent Network

The test was referred to the time period May 11-12th, 2014 and only GPS observations were employed. Starting from dual frequency observational files (RINEX format) collected by geodetic receivers at 30 s rate, the three methods were applied to M0SE observations using only one of its frequencies.
First of all the Geometry-Free combination (GF) was applied. This

Fig. 3.5: Employed dual-frequency receiver map

combination remove the geometric part of the measurement leaving all the frequency-dependent effects (i.e. ionospheric refraction, instrumental delays, wind-up) and so can be used to estimate the ionospheric electron content. In this sense it was possible to evaluate the differences between the ionosphere reconstructions obtained applying in turn the three methods described before.

Results obtained through the application of ANGBAS are shown in Figure 3.6.

The method was applied using as reference in turn four receivers located at increasing distance (35m, 25km, 38km and 65km) from the single frequency receiver. The plot shows the increasing noise of the method as the distance of the single-frequency receiver from the reference, taken into consideration for each case, increases.

The original SEID algorithm produced the result given in Figure 3.7 . In this case, as explained before, it was necessary to use at least three

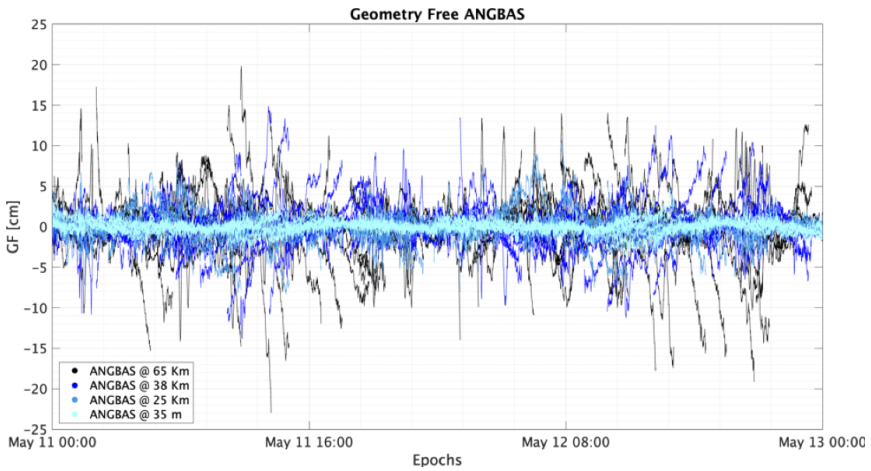

Fig. 3.6: Geometry free output by "A New Ground Based Augmentation Strategy (ANGBAS)"

receivers to reconstruct the observation. Four receivers were considered (19km, 25km, 38km and 65km) and the plane interpolation produced a stable solution. The limit of this approach is that a number of geodetic receivers are necessary and not always, neither everywhere, this is possible.

The last application regarded the goSEID model, Figure 3.8; the default implementation of SEID approach integrated in the goGPS open source software, which differs from the traditional SEID because interpolation does not take place through the reconstruction of a plane, as described before, but by a linear interpolation.

In this case the solution obtained by using only one by one receiver, at increasing distance (35m, 25km, 38km and 65km) from the single-frequency device, was tested and compared to the application of the same procedure involving the configuration of all four receivers available (19km, 25km, 38km and 65km).

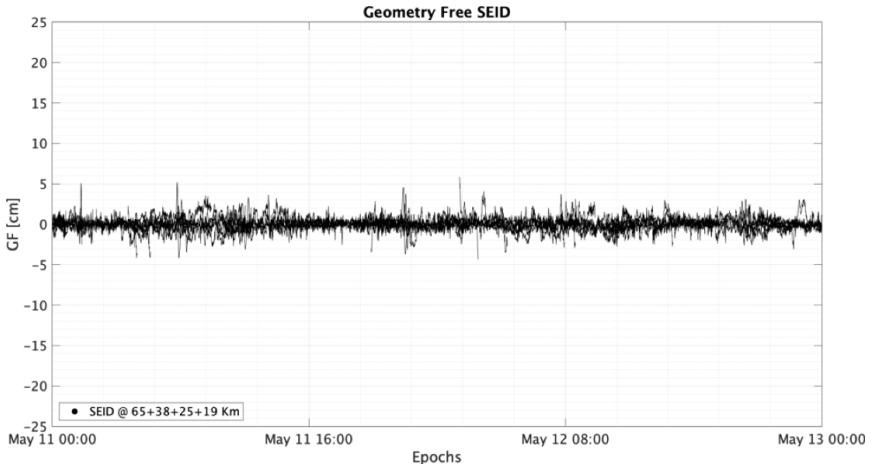

Fig. 3.7: Geometry free output by the original "Satellite-specific Epoch-differenced Ionospheric Delay (SEID)"

The obtained results show great stability, highlighting the versatility of the proposed method that does not have the limits of SEID in terms of number of receivers and shows improvements in statistical terms, for the same application, compared to the ANGBAS method.
In general, it is possible to observe the output variation in relation to the distance between the reference receiver for synthetic L2 observations reconstruction and the target receiver (from here on always M0SE).
A table with a simple statistical analysis is given below, where Standard Deviation values related to GF outputs for each distance are shown (Table 3.1).
In the second phase the PPP technique [121], undifferenced phase observation processing, was applied to daily processing sessions, and ionospheric free combination was used in order to estimate ZTD values for each epoch. For what concerns the ancillary products (ephemeris and

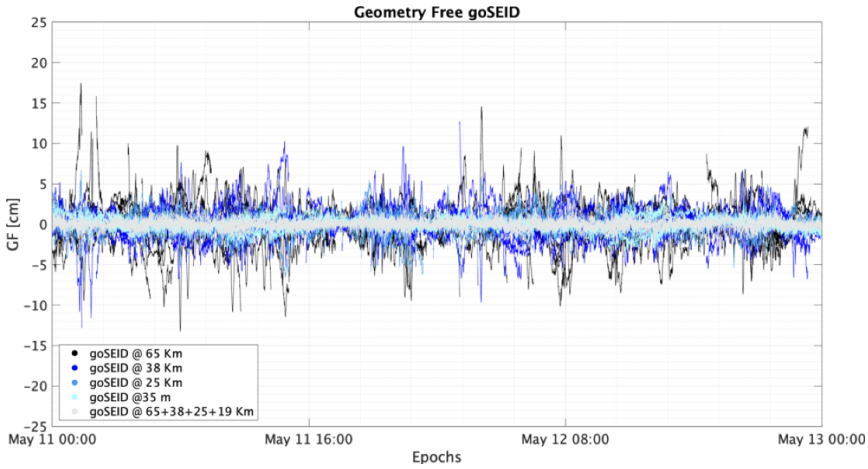

Fig. 3.8: Geometry free output by goSEID model

Tab. 3.1: GF Standard Deviation values related to the different methods applied

ANGBAS @35 m	0.7 cm
ANGBAS @25 km	1.7 cm
ANGBAS @38 km	2.4 cm
ANGBAS @65 km	3.5 cm
SEID @ 65+38+25+19 km	0.7 cm
goSEID @35 m	0.7 cm
goSEID @25 km	1.1 cm
goSEID @38 km	1.6 cm
goSEID @65 km	2.3 cm
goSEID @ 65+38+25+19 km	0.6 cm

clocks), precise products provided by the International GNSS Service (IGS) were employed.

This procedure was followed for the dual-frequency M0SE and for the M0SE with the synthetic L2 observations reconstructed by the three

methods explained above, using receiver located at different distances from the target (Table 3.1).

A validation procedure by atmospheric sounding (Figure 3.9) was conducted only for the output obtained by the original dual-frequency RINEX, which is that used as reference result. In this case the procedure implemented in goGPS software and described in Chapter 4 allowed the calculation of ZTD from atmospheric sounding data [111] obtaining the following results in terms of mean and standard deviation: 0.51 cm and 0.77 cm.

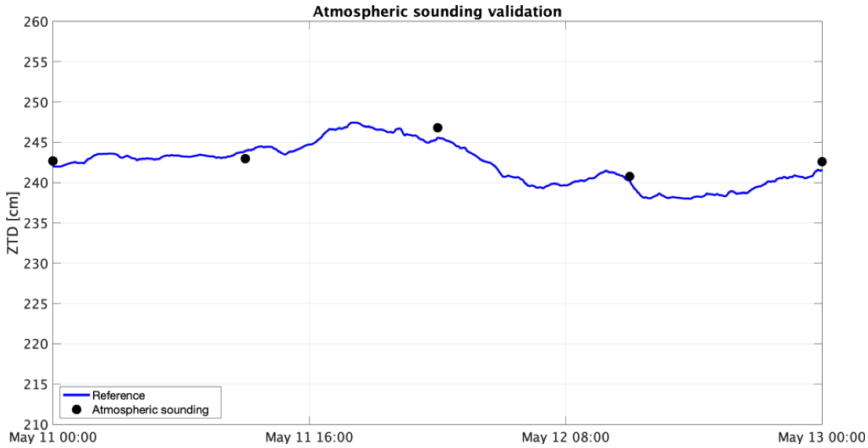

Fig. 3.9: Dual-frequency GPS-ZTD validation by atmospheric sounding

At this point, reconstructed RINEX data were processed and outputs compared each other in order to obtain a statistic of the reconstruction impact on ZTD calculation.

In Figure 3.10, Figure 3.11 and Figure 3.12 it is possible to observe respectively the ZTD values obtained employing the three methods of synthetic L2 reconstruction. In Figure 3.10 outputs related to ANGBAS L2 reconstruction method, applied using receivers at dif-

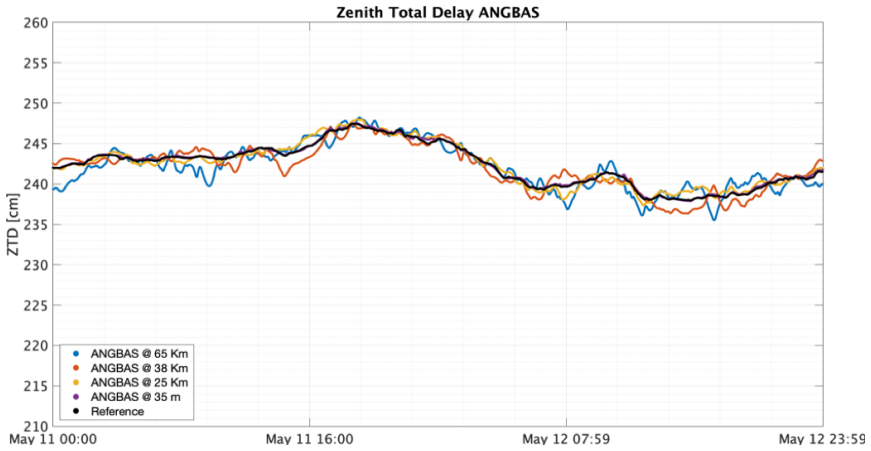

Fig. 3.10: Zenith Total Delay by "A New Ground Based Augmentation Strategy (ANGBAS)"

ferent distances from the target, are given. In Figure 3.11 the result related to SEID, using the four stations (RMPO, FIUM, VALM and CVTV) to interpolate the plane, is shown. Figure 3.12 represents the

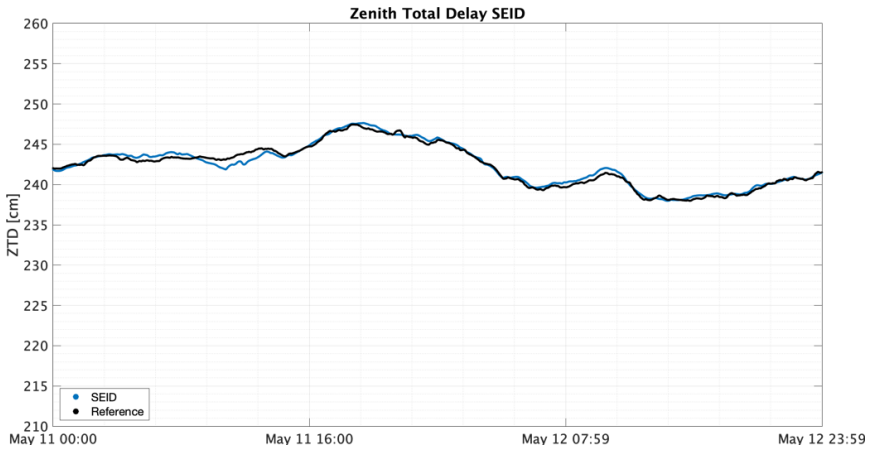

Fig. 3.11: Zenith Total Delay by the original "Satellite-specific Epoch-differenced Ionospheric Delay (SEID)"

results obtained through the use of goSEID; also in this case the four stations configuration involved RMPO (19Km), FIUM (25Km), VALM (38Km) and CVTV (65Km) receivers, whereas the use of one by one receivers regards the increasing distance of ROUN (35m), FIUM, VALM and CVTV devices. In Table 3.2 Zenith Total Delay Standard Devia-

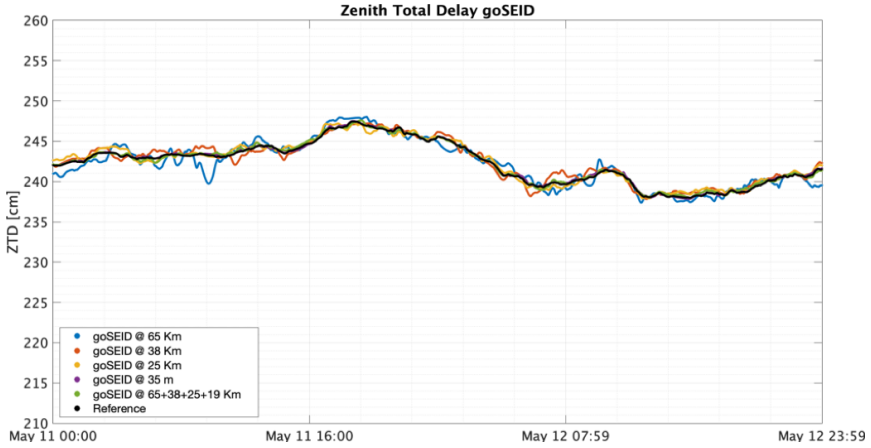

Fig. 3.12: Zenith Total Delay by goSEID model

tion values, referred to the three methods and to receivers at different distances from the target, are given.

The three methods, ANGBAS, SEID and goSEID, have been applied on a single-frequency RINEX and processed by goGPS software using PPP method. Results were studied in terms of geometry-free combination output and ZTD output and compared to the results obtained using the original dual-frequency M0SE's RINEX. In each case a statistical analysis was given in order to quantify the effects. The research deliverables showed a good agreement between the methods and a tangible improvement related to the use of methodology integrated in the goGPS open source software (goSEID); the reason is to be found in

Tab. 3.2: ZTD Standard Deviation values related to the different methods applied

ANGBAS @35 m	0.1 cm
ANGBAS @25 km	0.5 cm
ANGBAS @38 km	0.8 cm
ANGBAS @65 km	1.1 cm
SEID @ 65+38+25+19 km	0.4 cm
goSEID @35 m	0.1 cm
goSEID @25 km	0.4 cm
goSEID @38 km	0.5 cm
goSEID @65 km	0.8 cm
goSEID @ 65+38+25+19 km	0.2 cm

the fact that this method (goSEID) is the result of a reasonable combination of the strengths of the two previous methods (ANGBAS and SEID).

Indeed, the use of more than one receiver, if available, in an optimal configuration for the target RINEX reconstruction (see Figure 3.5), shows a solution improvement if this configuration is used employing an interpolation based on receiver's distance.

Using only one reference device, the solution degrades with increasing distance; however, in critical study area, where no more than one geodetic receiver is available, within certain distances and under known conditions, the application of goSEID can provide good solutions (Figure 3.12).

3.3.2 Bernese 5.2

The Bernese GNSS Software is a scientific, high-precision, multi-GNSS data processing software developed at the Astronomical Institute of the University of Bern (AIUB) [33].
All principal observables recorded by high precision geodetic receivers may be processed and nowadays Bernese 5.2 is considered one of the reference for GNSS data processing. Observation are processed by least squares estimation. Many parameter types are implemented in the Bernese GNSS Software Version 5.2 [33]. In this context a test was

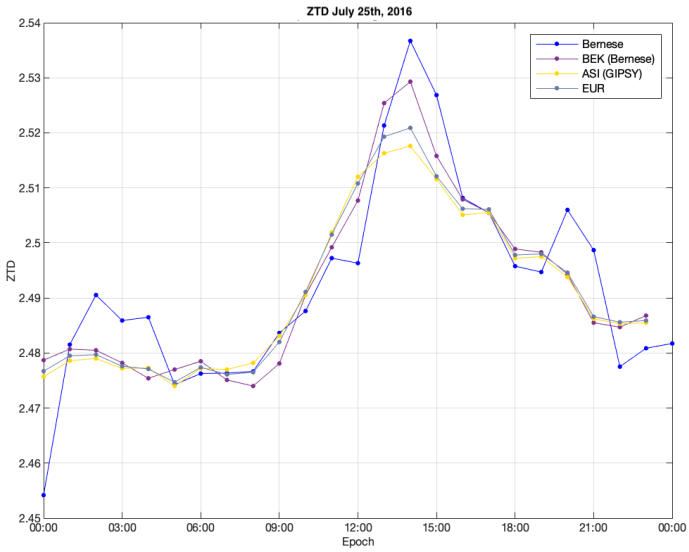

Fig. 3.13: One day (July 25^{th}, 2016) test carried out comparing outputs (ZTD [m]) obtained by Bernese 5.2 and outputs provided by several research centres

carried out in order to evaluate the coherence between official ZTD

estimations and an independent processing.
A one day test was in this sense performed comparing outputs obtained by Bernese application and outputs provided by several research centres. Bernese outputs were obtained applying the PPP (Precise Point Positioning) method, with a 1 hour time rate, using precise products provided by the Center for Orbit Determination in Europe (CODE). The statistical analysis produced the following results, which show a good agreement at the level of 1cm.

Tab. 3.3: Bernese ZTD output statistical analysis [m]

	mean	**st.dev.**	**RMSE**
Bernese-ASI	0.002	0.009	0.01
Bernese-BEK	0.001	0.009	0.009
Bernese-EUR	0.001	0.009	0.009

3.3.3 RTKLIB

RTKLIB is an open source program package for standard and precise positioning with GNSS [103]. Observations are processed sequentially using the extended Kalman filter (EKF) [91].
The program library of RTKLIB provides various functions of positioning algorithms for RTK-GPS [103]. RTKLIB provides also APs for real-time positioning, post-processing analysis, and positioning utilities [103]:

- Real-time positioning (RTKNAVI)
- Post-mission baseline analysis (RTKPOST, RNX2RTKP) - Communication utility (STRSVR)

- Plot graph of solutions and observation data (RTKPLOT) - RINEX converter of receiver raw data log (RTKCONV, CONVBIN)

3.3.4 goGPS

GoGPS software development started as a library of matlab routines for navigational purpouses. To adjust all GNSS related parameters, the software has traditionally used a Kalman Filter; recently the software has been reengineered introducing Object Oriented Programming (OOP) paradigm and optimizing several routines. Beside this, the focus of the software has switched from navigation to quasi static positioning, and the Kalman Filter has been abandoned in favour of a classical least square estimation [90]. After the pre-processing phase and during the processing step, various correction are applied to observations in order to eliminate unwanted physical phenomena from the measurements and remove periodical motions of the station[121].

3.3.5 Software comparison

In order to evaluate the effect on GPS-ZTD solutions, a test was carried out using both RTKLib and goGPS software on an equal dataset. A dual frequency receiver, ROUN, belonging to Lazio Region permanent network and located on the roof of Engeneering Faculty of Sapienza University of Rome, was selected. The test was performed on a week of data, the first of october 2018, with a time rate of 30 seconds. The applied methodology was the PPP and, for what concerns clocks and ephemeris, precise products were used.
As shown in the scatter plot given in Figure 3.14 there is coherence be-

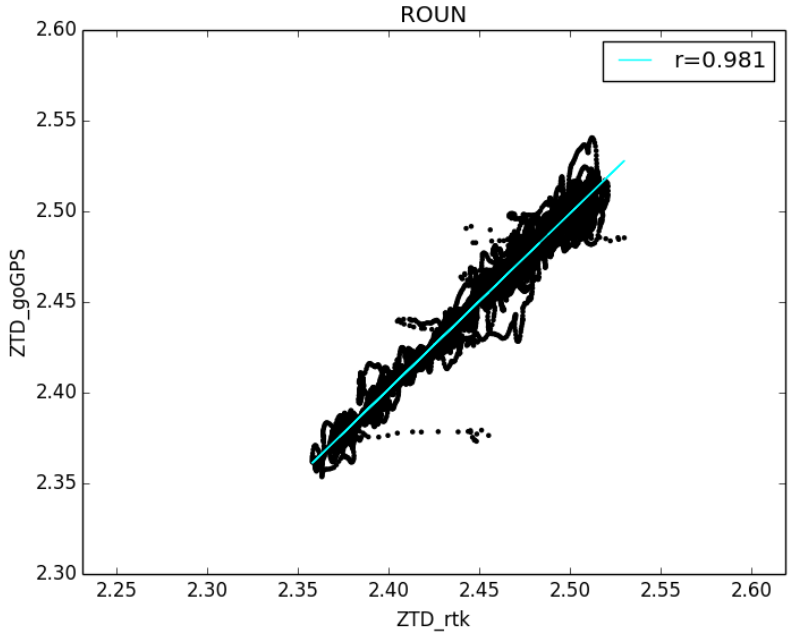

Fig. 3.14: Scatter plot of ZTD output from goGPS and RTKLib software, for ROUN geodetic receiver during the first week of October, 2018

tween outputs obtained using these two open source software (correlation coefficient=0.981), anyway it it possible to observe some patterns which are worth analyzing more carefully; to do this a plot of both trends and of their differences in respect of the epochs was produced in Figure 3.15. The patterns shown in Figure 3.15 point out a common behaviour, which results in a greater deviation between the results obtained with the two software, at about midnight; this attitude could be traced back to the implementation of the Kalman filter in the RTKLib software, which affects the solution in the early hours of the day. This effect is not found in the outputs obtained with goGPS software, as

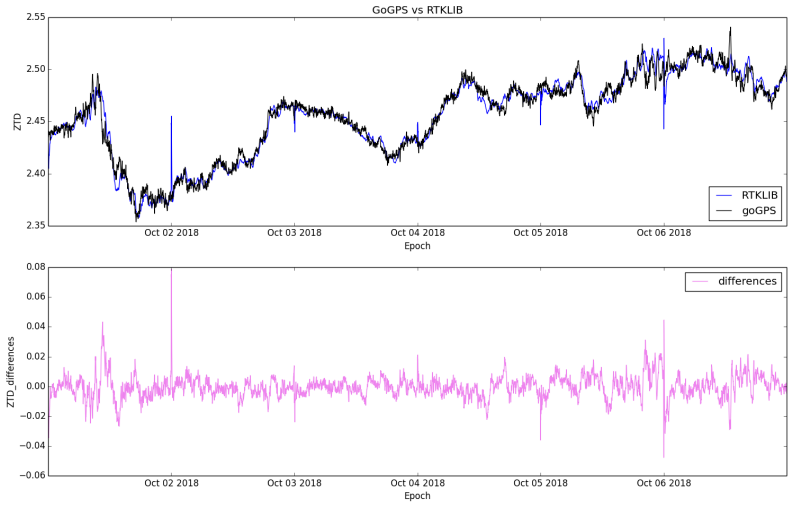

Fig. 3.15: Plot of ZTD output and differences from goGPS and RTKLib software, for ROUN geodetic receiver during the first week of October, 2018

the latter uses the least squares method. To sum up statistical analysis results on differences are given in table below.

Tab. 3.4: Differences statistical analysis

Mean [m]	-0.0002
Std.Dev. [m]	0.008
RMSE [m]	0.008
Median [m]	-0.0004
Max [m]	0.079
NMAD [-]	0.068

Chapter 4

PWV measurement sensors

Water vapor content of the atmospheric low layer is a highly variable component and there are many instruments which are used to assess its presence and study its behavior. The main goal of this section is to compare observations obtained by some of these instruments with those obtained by GPS data analysis. In particular a comparison between GPS output, atmospheric sounding and radiometers data was carried out and sun-sky radiometers' calibration, and validation of results obtained, was considered.

4.1 Radiosounding and Radiometer

4.1.1 Instruments

Radiosounding

Sounding balloons are extensively used in meteorological forecasting and research, to the extent that several hundreds of them are sent

daily into the atmosphere worldwide. They are mostly used to carry radiosondes aloft, enabling for the in situ recording of atmospheric variables with high temporal frequency and precision [48].
A radiosond is a small package hanging under a balloon of about two meters in diameter filled with hydrogen or helium; during the ascent of the radiosonde in the sky, at a speed of about 300 meters per minute, the sensors on board measure pressure, temperature and relative humidity profiles.
The flight of the radiosonda can last even more than two hours, and during this time the radiosonda can go up to more than 30 km of altitude and move more than 200 km from the point of release [1].
The diagram usually used to make plots of radiosonde soundings is one of the most common thermodynamic diagrams used in weather analysis: the nomogram of Herlofson.
The nomogram of Herlofson, commonly used by meteorologists, represents on the x-axis the temperature in linear scale, in the y-axis the natural logarithm of the pressure (Skew T - log P diagram).
The radiosond analysis involves the study of some thermodynamic indices which indicate the potential predisposition of the atmosphere to the onset of weather phenomena. The diagram is complex and rich in indices and information; it shows the state curve (temperature), the dew point curve (dew temperature), the wind speed line in knots and the saturated adiabatic line.
Two of the most interesting indices are the CAPE (Convective Available Potential Energy), a very useful index to calculate the instability of the atmosphere because it indicates the possibility that the particle of hot air rises to higher altitudes triggering convective motions, and the CINH (Convective Inhibition), which shows the energy available

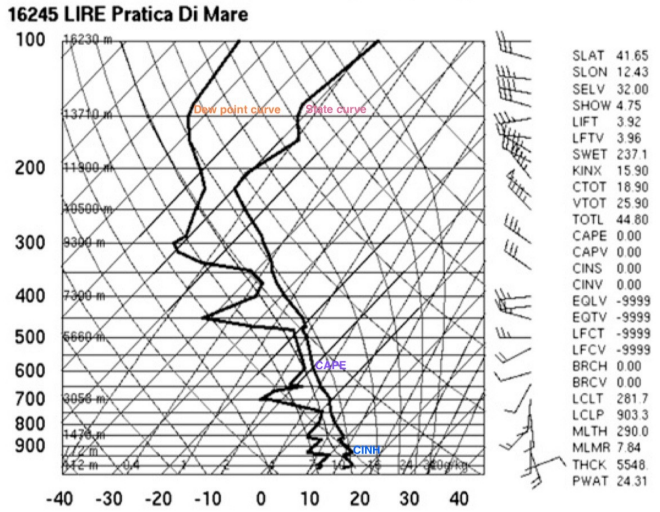

Fig. 4.1: Skew T–logP diagram, including wind characterization and indices, at 0000 UTC October 25^{th}, 2013 for Pratica di Mare [86].

(expressed in joules) in the low troposphere to prevent the occurrence of spontaneous vertical motions. If, for instance, the CAPE area is much larger than the CINH one, the conditions are favorable to the development of thermo-convective activity, given the considerable energy involved.
In Figure 4.2 an example of a radiosounding table output file is given.

In order to compare atmospheric sounding output with GNSS data, it is necessary to obtain a ZTD_{RAOBS} (ZTD RAdiosond OBServation) dataset.
From literature, analyzing the radiosonde accumulated water vapor as a function of altitude, a threshold value was determined; 99% of the total accumulated water vapor was reached at an altitude between 8 and 9 km [93].

PRES hPa	HGHT m	TEMP C	DWPT C	RELH %	MIXR g/kg	DRCT deg	SKNT knot	THTA K	THTE K	THTV K
1006.0	32	20.6	17.9	85	12.99	60	4	293.2	330.4	295.5
1005.0	41	20.4	17.9	86	13.01	62	4	293.1	330.3	295.4
1000.0	88	21.4	17.6	79	12.82	70	6	294.6	331.4	296.8
997.0	114	23.0	17.0	69	12.37	81	7	296.4	332.3	298.6
988.0	193	23.0	16.0	65	11.70	112	8	297.2	331.3	299.3
976.0	300	22.9	14.4	59	10.70	155	10	298.1	329.5	300.1

Fig. 4.2: 16245 LIRE Pratica Di Mare Observations at 00 12 Jun 2019; indices shown represent: Atmospheric Pressure, Geopotential height, Temperature, Dew point temperature, Relative humidity, Mixing ratio, Wind direction and speed, Potential temperature, Equivalent potential temperature, Virtual potential temperature.

In our case a threshold value of 8.9 km was set in order to consider empirical evidences and make a precise comparison between radiosonde and GPS-derived ZTD.

Considering that the ZTD is the integral of the refractivity over a vertical column of neutral atmosphere, it is possible to write the equation given below (which is analogous to Equation 3.6, but for a vertical path) [15]:

$$ZTD = 10^{-6} \int_{Z_{site}}^{Z_{top}} \left(k_1 R_d \rho_d + \left(k_2 + \frac{k_3}{T} \right) R_w \rho_w \right) dz \tag{4.1}$$

where ρ means density, z geometric height, R gas constant, whereas subscripts d and w mean dry and wet and the k's are empirically determined constants. Mindful that the available data from radiosonde are referred to meteorological parameters like pressure, temperature and specific humidity, it is possible to transform the integral for ZTD

into [111]:

$$ZTD = 10^{-6} \int_0^{p_{site}} k_1 \frac{R_d}{g} \delta p + 10^{-6} \int_0^{p_{site}} \frac{R_d}{g\epsilon} q \left((k_2 - k_1 \epsilon) + \frac{k_3}{T} \right) \delta p \tag{4.2}$$

where the integral extremes are the pressure at the site and the zero pressure, indicating that we are considering values until the radiosonde provides them; the first integral is called hydrostatic or dry delay (ZHD), the latter wet delay (ZWD); $R_d = 287[J*kg^{-1}*K^{-1}]$ [85] is the dry gas constant, g is the local vertical acceleration due to gravity and non inertial forces (including variation with height, that corresponds to using proper geometric heights for z), p is the pressure, T is the temperature, q is the specific humidity, ϵ is the ratio of the molecular weight of water vapor to that of dry air and k coefficients are constants empirically determined, which quantify the refractivity of the lower neutral atmosphere for radiowaves in the GPS range and derive from the widely used formula for atmospheric refractivity N [99] [24] [15]:

$$N = k_1 \frac{P_d}{T} + k_2 \frac{P_v}{T} + k_3 \frac{P_v}{T^2} \tag{4.3}$$

where P_d and P_v are the partial pressure of dry air and water vapor, respectively, and T is absolute temperature [15].
The values of these physical constants, indicated for instance in Bevis et al. 1994 [15], are listed below:

$k_1 = 77.60[K/mb] = 7.76 * 10^{-1}[K/Pa]$
$k_2 = 70.4[K/mb] = 7.04 * 10^{-1}[K/Pa]$

$k_3 = 3.739 * 10^5 [K^2/mb] = 3.739 * 10^3 [K^2/Pa]$

Using ZTD equation it is important to include the variation of g with height; the effect of not doing so is around $5mm$ in ZTD at mid latitudes[111].
Moreover, the ZHD integral contains significant contributions up to about $80km$ above the geoid, consequently an expression for the contribution to the dry delay (due to the part of troposphere which extends from the radiosounding higher measure point upwards), based on an assumption of hydrostatic equilibrium, was derived [111]:

$$\Delta ZHD \approx \frac{k_1 R_d p_1}{g_1} \left[1 + 2\frac{R_d T_1}{r_1 g_1} + 2\left(\frac{R_d T_1}{r_1 g_1} \right)^2 \right] \tag{4.4}$$

where T_1, g_1 [109], r_1 and p_1 are the values at the top of the radiosounding profile.
This contribution has to be added to the numerical integral of the profile data when calculating the delays:

$$ZTD_{RAOBS} = ZTD + \Delta ZHD \tag{4.5}$$

The contribution to ZWD can be considered negligible, because at such high altitudes $q \approx 0$ [111].
Once ZTD values corresponding to the radiosonde launch at the time of interest have been obtained, ZTD data from GPS processing, of receivers already corrected by a quadratic function of height, are elaborated through a natural neighbor interpolation at the radiosonde launch coordinates.

The algorithm, implemented in goGPS software, is based on the Sibson theory [95] of Natural Neighbours coordinates, associated to the principle of Natural Neighbours (NN) and to the Voronoi polygons. According to this geometric theory, the experimental data are honoured and no subjective criteria are introduced in the realization of the map [82].

Referring to Figure 4.3, in order to interpolate the value at point X,

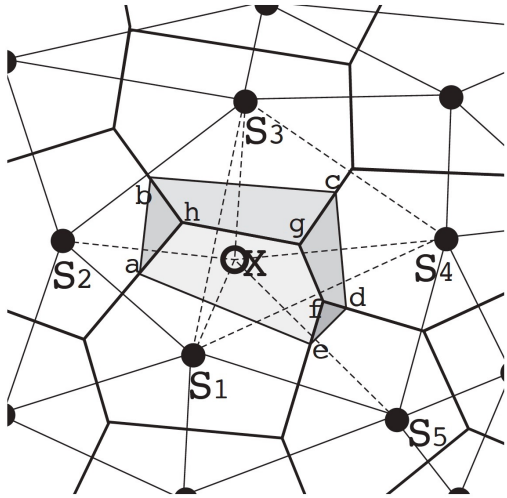

Fig. 4.3: Interpolation scheme with Natural Neighbor coordinates [96] [82]

its Natural Neighbours S_i are considered.

The NN interpolation method is based on the attribution of weights, for each point of observation, based on the concept of "area of influence". The algorithm uses a partition of the plane based on Voronoi polygons (or Thiessen polygons).

In the case of the plane, given a finite set of points S, the Voronoi diagram for S is the partition of the plane which associates a region

V(S_i) to each point S_i in S, so that all points of V(S_i) are closer to S_i than to any other point in S.
For the estimation of the value in node X, this is temporarily entered in the input value dataset (S). Taking into account the new value (X), the polygons are redefined, thus creating a new polygon and redefining the adjacent ones.
The new polygon (related to X) is characterized by having a surface partly borrowed from the pre-existing polygons.
The estimated value at the node X is equal to the sum of the values in the adjacent points (S_i) each multiplied by a weight. As an example, referring to the Figure 4.3, the weight of observation in S_1 used to predict the value in X, is the ratio between the area borrowed from the pre-existing polygon (e.g. ahgfe) and the area of the polygon referred to the node X (e.g. abcde).

Radiometer

The radiometer is a passive sensor that bases its performance on the laws of thermal-electromagnetic emission of bodies.
In the absence of scattering, as it happens in rain-free conditions, under the hypothesis of local thermodynamic equilibrium [115], the PWV (as well as the integrated cloud liquid water content, ILWC) can be estimated from brightness temperature measurements using at least two frequency channels, one of which (f_1) must be mainly sensitive to water vapor, and the other one (f_2) more to the liquid water content in clouds. To this aim, first the total path attenuation at frequency f_i (for a link with elevation angle θ) is calculated from the brightness

temperature T_B as:

$$A(f_i,\theta) = 10\log_{10}\frac{T_{mr}(f_i,\theta) - T_C}{T_{mr}(f,\theta) - T_B(f,\theta)} \tag{4.6}$$

where $T_C = 2.73K$ is the cosmic background temperature and $T_{mr}(f_i,\theta)$ is the so called mean radiating temperature [71], whose monthly values, in turn, can be calculated, for instance in the experiment described in the next paragraph, by regressing the results obtained from 10 years of Linate Airport RAOBS-derived vertical profiles of pressure (P), relative humidity (RH) and temperature (T) used as input first to the TKK cloud detection method [89] and then to the Liebe MPM93 mass absorption model [68]. In non-rainy conditions, $A(f_i,\theta)$ can also be written as:

$$A(f_i,\theta) = A_{OX}(f_i,\theta) + a_V(f_i)PWV(\theta) + a_L(f_i)ILWC(\theta) \tag{4.7}$$

where $A_{OX}(f_i,\theta)$ is the mean monthly path attenuation due to oxygen at frequency f_i, while $a_V(f_i)$ and $a_L(f_i)$ are the monthly water vapor and liquid water mass absorption coefficients computed by combining RAOBS profiles and mass absorption models [68] [71].
The two unknowns PWV and ILWC can be retrieved by using Equation 4.6 for both radiometric channels (f_1 = 23.84 GHz and f_2 =31.4 GHz) and by solving the resulting system of two equations, thus yielding:

$$PWV(\theta) = a_0 + a_1 A(f_1,\theta) + a_2 A(f_2,\theta) \tag{4.8}$$

where $a_0 = -0.0298, a_1 = 53.626$ and $a_2 = -32.488$ are function of $A_{OX}(f_i,\theta), a_V(f_i)$ and $a_L(f_i)$.

4.1.2 Validation test

A comparative analysis of results provided by GNSS, radiosounding (RAOBS), the ECWMF model (operational products) and radiometer (RAD) was performed.
Time series of PWV obtained with these different methods are compared for a case study in Milan, over a period of about one year (March 1^{st}, 2018-February 11^{th}, 2019) in order to consider different seasonal variation and instruments coherence on long time period.
A four-channel Ka-band/W-band radiometer located in the main campus of Politecnico di Milano was employed.
In association to this, a GNSS dual-frequency receiver (MILA), belonging to SPIN Network and installed in the same campus, 280 m from the radiometer, was used. GPS data were processed applying the PPP strategy [121], implemented in goGPS software [56]. Starting from the dual-frequency observational files collected by MILA at 30 s rate, the PPP technique was applied to ionosphere free combination in order to estimate both coordinates and ZTD values. As regards ephemeris and clocks, precise products provided by the International GNSS Service (IGS) were used.
At this point, a preliminary comparison was carried out with ZTD derived by atmospheric sounding (16080 Milano-Linate) (Equation 4.5).
After the preliminary test, comparisons in terms of PWV were performed between radiometer, GPS, atmospheric sounding (16080 Milano-Linate) and ECWMF model (operational products).
If radiometer provides PWV estimates as output and the same parameter can be directly derived from radiosoundings and ECMWF model, regards GPS, starting from meteorological data of pressure and tem-

perature, after appropriate adjustments related to the difference in altitude between meteorological sensors and GPS receivers (Equation 3.8; Equation 3.9) [5] [9] [85] , PWV patterns can be properly obtained from ZTD values [16] [4] [34]. The table summarizes the results of the

Tab. 4.1: Statistics of the comparisons between PWV values derived from different sources, in terms of minimum (min) and maximum (max) differences, mean difference (mean) and standard deviation (std)

STATISTICS	**RAD-GNSS**	**RAD-ECMWF**	**RAD-RAOBS**
# samples	347135	1040	529
Min [mm]	-8	-7	-5
Max [mm]	5	4	5
Mean [mm]	-1	-0.8	-0.6
St.Dev. [mm]	1	1.5	1.5

statistical comparison of the differences between the radiometer and the three other sources of PWV values.

As shown by the values, the radiometer tends to underestimate PWV values, but differences have a standard deviation that is below 2 mm for every case.

The high variability in the number of samples used for each case is due to the significantly different measurement rates of the four techniques: the ECMWF model values are available every 6 hours, radiosondes are launched from Linate station every 12 hours, GNSS PWV is computed every 30 seconds and radiometer PWV every second.

It is also worth reminding that PWV estimates from the radiometer are reliable only under rain-free conditions, i.e. approximately 93% of the yearly time in Milan. Although the statistical comparison shows a

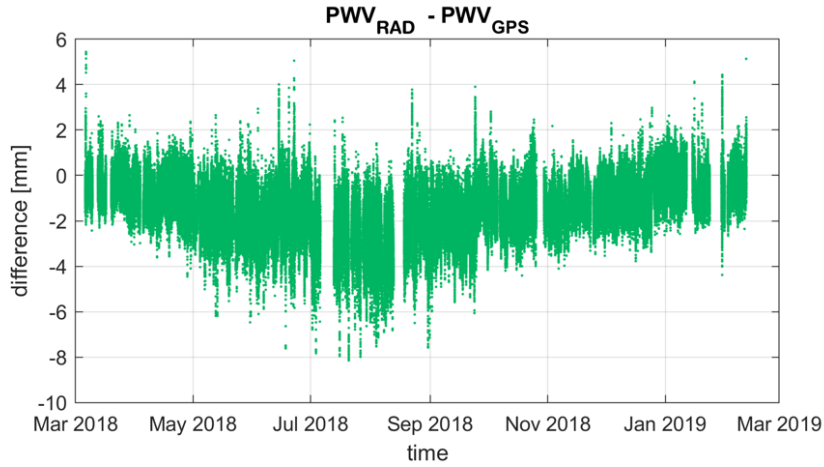

Fig. 4.4: Time series of differences between radiometer PWV values and GNSS PWV values

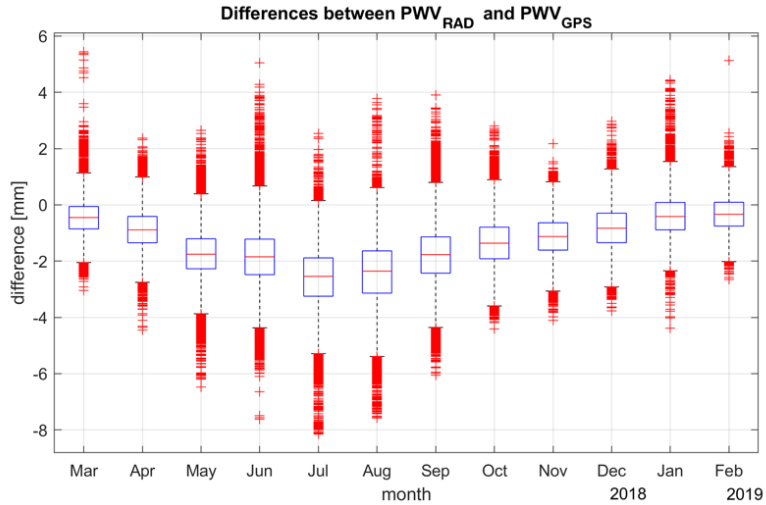

Fig. 4.5: Boxplot of monthly differences between radiometer PWV values and GNSS PWV values

good agreement between the different sensors' values, a further analysis on the time series of differences was performed, to highlight patterns related to seasonal variations.
Figure 4.4 shows the differences between radiometer and GNSS PWV. These differences increase during seasons with higher water vapor content (i.e. spring and summer).
This behaviour can be noticed also from the boxplot in Figure 4.5: monthly averages of the differences (symbolized by the boxes) reach their peaks in July and August.
Data gaps are associated to the lack of radiometer values during rainy days.
As shown in table above, results highlight a statistical agreement between the various data sources, confirming that a synergistic use of all these instruments is feasible.

4.2 Sun-sky radiometer

4.2.1 Instruments

Sun-sky radiometer

Sun–sky radiometers, or sun-photometers, operating in several international networks, are instruments able to provide PWV estimations with high temporal resolution.
A sun–sky radiometer is a narrow band filter photometer able to perform measurements of direct solar and diffuse sky irradiances at some selected wavelengths and at several scattering angles.
However, the great problem of this methodology is the estimation of

Fig. 4.6: POM-01 Sky Radiometer

the sun-photometric calibration parameters. In this sense, the aim of the test described in the following paragraph, is to validate a new methodology based on the hypothesis that the calibration parameters characterizing the atmospheric transmittance at 940 nm are dependent on vertical profiles of temperature, air pressure and moisture typical of each measurement site.
To obtain the calibration parameters some simultaneously seasonal measurements of PWV, from independent sources, taken over a large range of solar zenith angle and covering a wide range of PWV, are needed.
For this purpose, GPS data are particularly useful.

4.2.2 Calibration and validation test

In this test, yearly GPS datasets were used for obtaining a table of photometric calibration constants.

The methodology was applied and validated in three European ESR-SKYNET network sites, characterized by different atmospheric and climatic conditions: Rome, Valencia and Aosta.
Results were validated against the GPS and AErosol RObotic NETwork (AERONET) PWV estimations.
The three European ESR-SKYNET network sites are equipped with standard SKYNET network instrument, that is a sun– sky radiometer model POM-01 or POM-02, produced by PREDE Co., Ltd, Japan.
Although mainly used for studying atmospheric aerosol optical and physical properties in clear sky conditions, these instruments also perform irradiance measurements at 940 nm for water vapor studies.
The methodology used in this work has been specifically developed for estimating columnar water content from POM sun– sky radiometers (PWV_P), but can also be applied to other spectral radiometers.
A CIMEL CE318 sun–sky radiometer, part of the AERONET network (often called simply sun photometer), has operated in Valencia since 2007 and has been co-located with the ESR-POM since 2008. This instrument, also aimed at characterizing atmospheric aerosols, performs the same kind of measurements as the POM model but has some technical differences that require a further calibration for the diffuse radiance, which is not needed in the POM model [25]. Precipitable water vapor content from this instrument (PWV_{AER}) is calculated using the official AERONET inversion algorithm [98] and successive updates, also providing the aerosol products [26].
Three dual-frequency GNSS receiver stations were used for estimating the PWV_{GPS} content: M0SE receiver, located on the roof of the Faculty of Engineering, University of Rome "La Sapienza", about 2 km far from the sun–sky radiometer position; AOST receiver, part of the

NetGEO network, located in Valle d'Aosta region, about half a kilometer from the sun–sky radiometer position; and VALE receiver, located on the roof of the Escuela de Cartografia y Geodesia of Universidad Politecnica de Valencia, Spain, about 7 km east from the sun–sky radiometer position.
As regards the VALE device, it is part of the EUREF Permanent GNSS Network, and ZTD data are available, with time interval of 1 h, from the EUREF website (http://www.epncb.oma.be) [19].
For what concerns M0SE and AOST devices, starting from observational files with a time rate of 30s, PWV_{GPS} with a temporal resolution of 15 min was retrieved. In this case, the selected software was the Bernese GNSS Software version 5.2 and ancillary files were those provided by CODE.
Concerning the M0SE receiver, being part of the EUREF Permanent GNSS Network, the coordinates provided by CODE in the SINEX format files are known and the PPP absolute positioning and constrained coordinates methodology were used in the analysis.
Regarding the AOST receiver, the SINEX files are not available and the PPP and free network solution methodology were used, allowing the Bernese GNSS Software to estimate the station coordinates.
From the ZTD values, PWV_{GPS} can be calculated using pressure (P) and temperature (T) (Equation 3.13) predicted by a numerical weather prediction model or measured at the surface by weather stations located nearby the GNSS station. In this case, datasets were provided by the Agenzia Regionale per la Protezione Ambientale (ARPA) Lazio for M0SE station and by Regione Valle d'Aosta for AOST receiver. For station VALE, the surface pressure values from ECMWF reanalysis (ERA-Interim) were used.

The height difference between receivers and weather stations has been corrected (Equation 3.8; Equation 3.9) [85].
At this point, ZTD data were converted to PWV_{GPS} by the method described before (Equation 3.13) [16] [4] [34].
Many studies have assessed the accuracy of GPS-IWV estimates by comparison with measurements from other sensors (e.g. microwave radiometers, radiosondes, lidars). It is well recognized that results are dependent on the IWV itself, and thus on the geographic location (cold–warm climates) and on time (cold–warm or dry–wet season), but also on GPS processing options and of course on the quality of measurements from the reference sensor. Recent measurement campaigns performed at mid-latitudes have demonstrated root mean square differences < 0.1 cm [18] [22] [80], which can be considered as representative for this test [26].
PWV_{GPS} obtained by the three GPS receivers in Rome, Aosta and Valencia was used as an independent dataset for calculating the calibration constants of the co-located ESR/PREDE-POM sun–sky radiometers.
The cloud screening of radiometers measurements was performed by selecting those measurements whose root mean square deviation (RMSD) between measured and reconstructed diffuse sky irradiance at all the wavelengths, used for aerosol study, and all angles is lower than 20%. For the Rome site, an additional procedure was applied consisting in intercomparing the selected measurements with those provided by a co-located Multi-Filter Rotating Shadowband Radiometer (MFRSR), whose cloud screening was performed [3].
The closest PWV_{GPS} retrievals within 30 min, 15 min before and after the sun-sky radiometer measurements, were selected.

Then the simultaneous [PWV_{GPS}, V (direct solar irradiance measured by the POM sun–sky radiometer at the 940 nm wavelength in clear sky conditions)] dataset was divided in two parts by picking every other day among the available days: one part [$PWV1_{GPS}$, $V1$] was used for the application of the methodology and then the estimation of the calibration constants, while the other part of GPS estimations ($PWV2_{GPS}$) was used to validate the PWV_P retrievals. The two GPS datasets were found to be equally populated and with similar frequency distributions, and the statistical independence between the $PWV2_{GPS}$ data used for the validation and PWV_P was ensured.

Because a and b parameters (calibration parameters characterizing the atmospheric transmittance at 940nm wavelength) are supposed to depend on the total amount of water vapor, the entire yearly independent $PWV1_P$ dataset was divided in three classes: [0–10] mm, [10– 20]mm and [20–40]mm; an insufficient number of points were found with water vapor larger than 40mm for the three sites.

This methodology considers that a and b are dependent on vertical profiles of temperature, air pressure and moisture typical of each measurement site, and therefore allows for the calculation of pairs of (a, b) values for classes of PWV .

The sun–sky radiometer calibration parameters (a, b and V0) for each site and class were calculated, Figure 4.7. In the first application of this methodology [27], performed to calibrate a sun–sky radiometer at a Japanese site characterized by a wide yearly range of PWV (from a few millimetres up to about 60 mm), nearly parabolic opposite behaviours of a and b as a function of PWV were found. The similar behaviour of the boundary PWV classes (being two maxima of the distribution) was demonstrated to be linked to two different atmospheric regimes, with

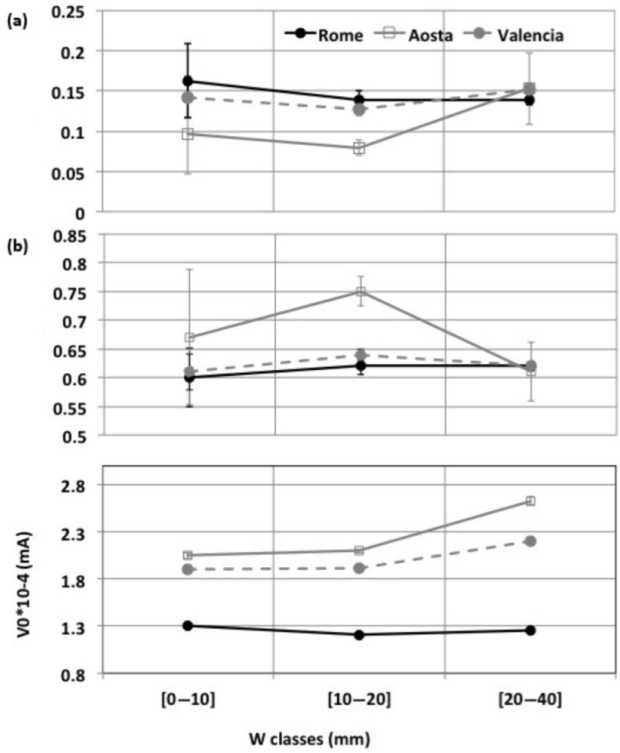

Fig. 4.7: Behaviour of the estimated calibration parameters compared to PWV (for the sake of brevity W in plots) classes. The errors bars are the errors affecting the parameters as evaluated using a Monte Carlo method

similar PWV vertical distribution: trapping of PWV due to winter inversion and occurrence of convection in summer. Both these regimes have a vertical structure with a well-mixed layer at the bottom and a rapid decrease upward.

This behaviour is recognizable in Aosta for the higher PWV class. In this season, in fact, the well-mixed layer at the bottom is likely due to humid polluted air masses transported from the Po Valley region,

starting from late afternoon and staying in the atmosphere up to the morning. This advection was observed by the ceilometer, which measured the increase of suspended particles in the atmosphere, and by hygrometers for the growth of absolute humidity [36]. Unfortunately there are no vertical profile measurements of PWV at this site to verify this statement.

Conversely in Rome and Valencia all the classes seem characterized by similar synoptic situations.

Looking at Figure 4.7, a slight tendency of V0 (solar calibration constant) on the water vapor class is recognizable. It should be noted that the retrieved V0 in this methodology should be considered as an effective calibration constant whose variation could not be related to a real instrumental drift. Nevertheless, its total uncertainty (estimated as the standard deviation of the assumed values in each class divided by their average) resulted to be about 4, 8 and 14 % for Rome, Valencia and Aosta, respectively.

One must bear in mind that this uncertainty is a statistical measure but not the total uncertainty of PWV retrieval, which should include instrumental uncertainties, errors introduced at different steps of the method and their spread, and any other systematic errors.

The estimated uncertainties values are comparable with that of AERONET retrievals [80], i.e. approximately 10 %, with the exception of Aosta, where a value of 20 %, with a RMSD of 2.7 mm, is obtained. This is probably related to the performance of GPS measurements in sites with rough orography. In fact, the methodology used for the calculation of ZTD assumes an azimuthal isotropy of the atmosphere above the antenna, within a conical field of view with an angular aperture of about 170° (since the elevation angle cut-off was set to 5°) centred

in the site where the antenna is located. However, the orography can make the distribution of air velocity quite complex and not uniform at high levels; the rougher the orography, as that surrounding the Aosta site, the greater is the atmospheric anisotropy and therefore, in principle, the error introduced by the failure of the hypothesis assumed by GPS methodology. This degradation of the quality of GPS retrieval, not quantifiable, together with the missing of a large amount of GPS data in Aosta during the summer months, makes the fitting procedures used for the retrieval of calibration constants less stable and therefore increased the uncertainty in their estimation [26].
As told before, in this test the GPS dataset was divided in two parts by picking every other day from the available days: one part was used for the calibration of the sun–sky radiometer and the other part for the validation.
The obtained PWV_P values were characterized by an uncertainty ΔWP below 10 % for Rome and Valencia and of 20% for Aosta.

The yearly time pattern of PWV_P for each site was then validated against the part of the GPS dataset not used for the calibration and against an AERONET sun photometer co-located in Valencia.
In the former case for Rome and Valencia the agreement was found to be within the uncertainty ΔWP when all the classes together are analysed, whereas for Aosta a % RMSD of about 14% was found.
Investigating separately the three classes, the greatest difference was found for the first class in terms of % RMSD: 9.18, 14.51 and 18 %, for Rome, Valencia and Aosta respectively.
When compared against the AERONET retrieval, the agreement was found to be very good and within the uncertainties of both methodologies when all the classes together are considered.

However, analysing the results by classes, and after a cross-check among PWV_P, GPS and AERONET estimates, it was highlighted that the present methodology is able to generally improve PWV estimation, particularly for low PWV content in term of % bias, bringing the agreement with the GPS (considered the reference) from a % bias of 5.76 to 0.52.

This finding is in agreement with what was already demonstrated and available in literature [27], where the assumption of variable a and b parameters was compared with the results from the assumption of fixed a and b.

The presented methodology can be easily applied to other kind of sun photometers or radiometers measuring the solar direct radiation at 940 nm wavelength. The calibration table containing a and b values for each PWV class can be used until the instrument is moved to another location or is submitted to maintenance. In these cases all the calibration parameters must be recalculated.

The problem in the application of this methodology is, however, the availability of an independent, simultaneous PWV dataset to be used for calibrating the sun–sky radiometer or any other similar sun-photometer.

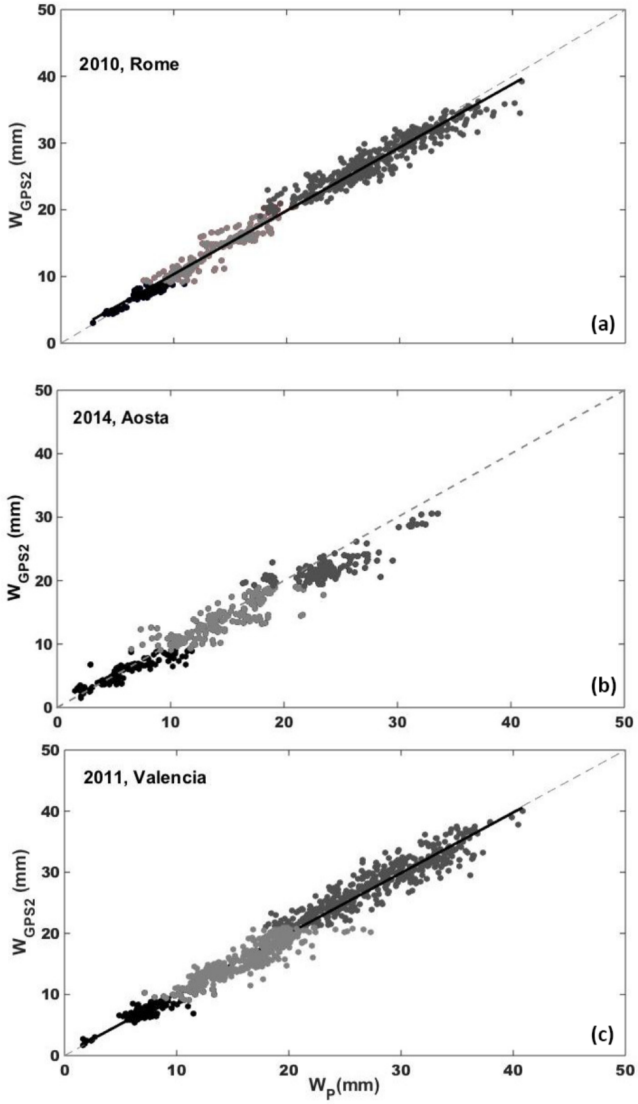

Fig. 4.8: Scatter plot of $PWV2_{GPS}$ and PWV_P (for the sake of brevity WGPS2 and WP in plots). Alternations of black and greys indicate the three water vapor classes

Chapter 5

GPS assimilation

GNSS data can be very useful for meteorological purposes and one of the most impactful applications is related to the assimilation in numerical weather prediction models [110] [42] [83] [8] [69].
There are several examples, available in the scientific literature, which in relation to this application have provided encouraging results as it is reported below.

- Assimilation of GPS-ZTD into the HIRLAM (High Resolution Limited Area Model), using 3D-Var, showed improvements for the high precipitation forecast [110]

- Assimilation of GPS-ZTD over Italy, using the MM5 model at 9 km horizontal resolution and 3D-Var, gave improvements in the precipitation forecast during the transition from winter to spring [42]

- Assimilation using 4D-Var and the Météo-France ARPEGE (Action de Researche Petite Echelle Grande Echelle) global model

showed the positive impact of the GPS-ZTD data on the synoptic-scale circulations forecast and improvements on the precipitation forecast in spring and summer [83]

- A positive impact of the GPS-ZTD assimilation on precipitation forecast for heavy precipitation events occurred over France was found also using a limited area model at about 2.5 km horizontal resolution [119] [23]

- Assimilation by both 3D-Var and 4D-Var, using the Met Office NAE model [84] at 12 km and 24 km horizontal resolutions, depending on the specific numerical experiment, showed that the assimilation of GPS-ZTD increased the relative humidity at the levels considered for the analysis, resulting in an improvement of the cloud forecast. However, using the 4D-Var instead of 3D-Var, it had a limited impact on the forecast [8]

- GPS-ZTD data assimilation, into the HARMONIE-AROME model run at 2.5 km horizontal resolution, was performed by 3D-Var and improved the forecast up to one and half day, especially for humidity [69]

Taking into account what has been mentioned so far, in this chapter the assimilation of GPS-ZTD, from both geodetic (dual-frequency) and single-frequency receivers, in the Regional Atmospheric Modeling System at the Institute for Atmospheric Sciences and Climate (RAMS@ISAC), is shown.
The data assimilation was performed by 3D-Var, extending the methodology of Federico [44] and its impact on the analysis and Very Short-

term Forecast (VSF), of vertically integrated water vapor (IWV), is shown by numerical experiments [73].

5.1 GPS assimilation by 3D-var

In general, the purpose of the data assimilation is to (optimally) use all the available information, to determine as accurately as possible the state of the atmosphere [44] [42] [8] [19].
The RAMS 3D-Var is able to assimilate vertical profiles of temperature, relative humidity and winds [44].
New features of the 3D-Var include the assimilation of radar reflectivity and GPS-ZTD, while lightnings are assimilated through a technique called nudging.
Finally, surface observations are assimilated by Optimal Interpolation [62] [43].
In this thesis, however, only GPS-ZTD estimates are considered observations for the RAMS 3D-Var and are assimilated [73].
In this case, the observed GPS-ZTD and the ZTD estimates given by the RAMS meteorological model, which depends on the simulated temperature (T) and humidity (more specifically we consider the mixing ratio (q) 3D-fields), are used.
The (q,T) model fields entering the analysis are called the "background". The analysis adjusts the (q,T) fields so that ZTD computed from the analysis is closer to the observed ZTD compared to the ZTD computed from the background.

Variational data assimilation involves the minimization of a cost func-

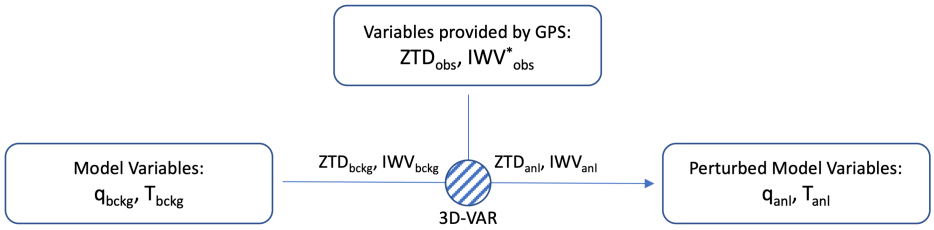

Fig. 5.1: The water vapor mixing ratio (q) and temperature (T) given by the RAMS model (background) are adjusted according to the assimilation of the GPS-ZTD with the purpose of improving the representation of the humidity and temperature fields.

tion:

$$J(x) = 1/2(x-x_b)^T B^{-1}(x-x_b)+1/2[y_o-H(x)]^T R^{-1}[y_o-H(x)] \quad (5.1)$$

where x_b is the background state vector, B is the background error matrix, y_o is the observation vector, R is the observation error matrix and H is the forward observation operator, transforming the state vector into the observed variable (simulated ZTD in correspondence of the GPS receivers in this case) [73].
In this sense, $J(x)$ provides the variations to be made to the primary variables of the model $x = (q, T)$, starting from modeled ZTD (H(x)) and observed ZTD (y_o). It is important to underline that x_b is a column vector whose length is $nvar \times nxyza$, where nxyza is the number of the RAMS grid points, i.e. $nxyza = nnxp \times nnyp \times nnzp$ (where nnxp, nnyp and nnzp are the grid points numbers splitted in three

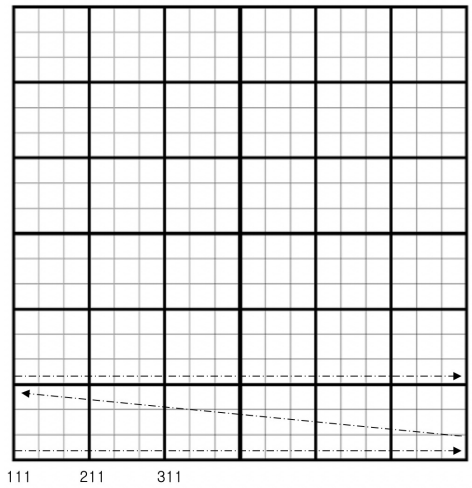

Fig. 5.2: The model and analysis horizontal grids. The thick lines show the analysis grid, while the thin lines show the native model grid. The analysis can be performed on a reduced grid

components), and nvar is 2, the mixing ratio of water vapor and temperature for each node.

Stated in other terms, the model values of water vapor mixing ratio and temperature are ordered in a column vector, where the first nxyza components refer to water vapor mixing ratio and the second nxyza values refer to temperature.

Each of the variables is ordered starting from the SW corner of the first model vertical level and moving first towards east and then to the north.

Once the first level is completed we pass to the second level, and so on until the NE grid corner of the last level is reached. x_b represents the initial value of x provided by the model.

$$\vec{x_b} = \left(q_{111}q_{211}q_{311}...T_{111}T_{211}T_{311}...\right)^T \quad \vec{x_b} = \begin{pmatrix}\vec{q}\\ \vec{T}\end{pmatrix} \tag{5.2}$$

If we call nxa, nya and nza the grid point numbers of the analysis used in the algorithm and nx, ny and nz the grid points of the model, which has a horizontal resolution of 4 km, in general we could have that:
$nza = nz$ (because it is not possible to undersample vertically)
$nxa < nx$
$nya < ny$
The analysis domain has the same extension of the model domain, but it can have a lower horizontal resolution.
In the results shown in this chapter, for example, the model has 4 km of horizontal resolution, whereas the analysis has 16 km of resolution.

The minimization algorithm, which uses the conjugate gradient method, minimizes the function $J(x)$ and gives as output the value of x minimizing $J(x)$. We will therefore have q and T values for each point of the analysis grid.
y_o is a column vector whose length is np, i.e. the number of observations available at the assimilation time after the quality control procedure applied to the GPS-ZTD data (from here on out considered as observations: $\vec{y_o} = (n_p)$)

A selection of observations, which results 0 or 1 depending on whether the station is usable or not, is made taking into account the following criteria:

- the stations must belong to the domain

- $H_{model} - H_{GPS} < 300m$ (H are orthometric heights at the respective points)

- the stations must have enough data to calculate significant values for the statistics in Table 5.1 (N is at least 10)

Tab. 5.1: Statistical indices

Bias $[m]$	$\sum_{i=1}^{N}(ZTD_{Ri} - ZTD_{Gi})/N$
Absolute error measure $[m]$	$\sum_{i=1}^{N}\lvert ZTD_{Ri} - ZTD_{Gi}\rvert/N$
Root mean square error $[m]$	$\sqrt{\sum_{i=1}^{N}(ZTD_{Ri} - ZTD_{Gi})^2/N}$
Correlation coefficient $[-]$	r
ZTD-GPS$_{mean}$ $[m]$	$\sum_{i=1}^{N} ZTD_{Gi}/N$
Root-mean-square error (GPS) $[m]$	$\sqrt{\sum_{i=1}^{N}(ZTD_{Gi} - \overline{ZTD}_G)^2/N}$

$R(n_p \times n_p)$ matrix is the combined observation and forward operator error covariances. It is assumed diagonal (the observation error covariances are neglected).

$$R = \begin{pmatrix} \sigma_1^2 & 0 & ... & 0 \\ 0 & ... & ... & 0 \\ 0 & ... & ... & 0 \\ 0 & ... & 0 & \sigma_{n_p}^2 \end{pmatrix} = \begin{pmatrix} RMSE_{G1}^2 & 0 & ... & 0 \\ 0 & ... & ... & 0 \\ 0 & ... & ... & 0 \\ 0 & ... & 0 & RMSE_{G_{np}}^2 \end{pmatrix} \tag{5.3}$$

$$R^{-1} = \begin{pmatrix} 1/RMSE_{G1}^2 & 0 & ... & 0 \\ 0 & ... & ... & 0 \\ 0 & ... & ... & 0 \\ 0 & ... & 0 & 1/RMSE_{G_{np}}^2 \end{pmatrix} \tag{5.4}$$

B matrix is the Background error matrix and it is the model error matrix. B matrix is really big, its dimension is [nxyz, nxyz] where $nxyz = nx \times ny \times nz = 101 \times 101 \times 36 = 367236$ (for instance); this means that the inversion of the B matrix is not actually computationally feasible.

To remedy this problem, it is possible to split the matrix in the horizontal plane (B_h) and in the vertical direction (B_z).

Using this decomposition, B is given by the application of two operators; because of the form of matrices, if it had been considered the problem as separate since the beginning the result would have been the same. It is important to note that the product $B = B_z \times B_h$ is not analytically correct, in fact because of their dimension these matrices cannot be multiplied. It is, then, possible to proceed only with a sequential application of the two operators to the vector $x - x_b$.

$$B_z \times B_h \times \begin{pmatrix} n_z \\ \dots \\ n_{xy} \\ \dots \\ n_z \\ \dots \\ n_{xy} \\ \dots \\ n_z \\ \dots \end{pmatrix} \tag{5.5}$$

where, for instance:
$B_z[n_z, n_z] = B_z[36, 36]$
$B_h[n_{xy}, n_{xy}] = B_h[101 \times 101, 101 \times 101]$

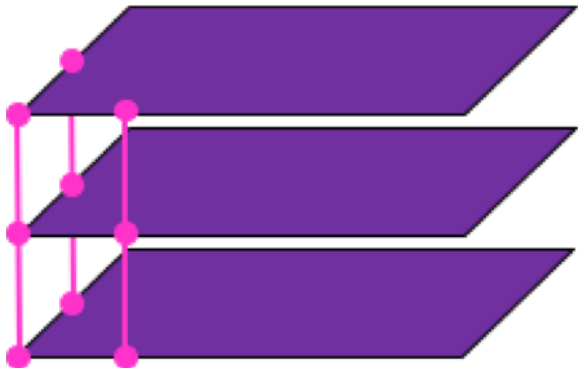

Fig. 5.3: Graphic representation of the operational phases

In addition to this, matrix B is splitted for moisture and temperature as if they were independent variables.
Operational phases:

- Application of B_h operator to each of the 36 levels (purple domain), as far as moisture is concerned (q)
- Application of B_h operator to each of the 36 levels (purple domain), as far as temperature is concerned (T)
- Application of B_z operator to each of the grid points on the entire columns (pink dots), as far as moisture is concerned (q)
- Application of B_z operator to each of the grid points on the entire columns (pink dots), as far as temperature is concerned (T)

$H(x)$ matrix transforms model variables (q,T) into observed variables (ZTD at the receivers' position). Once the ZTD values are obtained at the grid points, these must be predicted to the position of the receivers, in this algorithm, by a bilinear spatial interpolation.
Also $H(x)$ is given by the application of two operators in sequence:
$H = H_S \times H_{ZTD}$
where:
$H_{ZTD}[n_{xy}, n_{xyzvar}]$ in which var represents the number of variables (in this case 2: q,T)
$H_S[n_p, n_{xy}]$
To clarify, below are given the main steps of the operation, with the sequential application of the two operators:

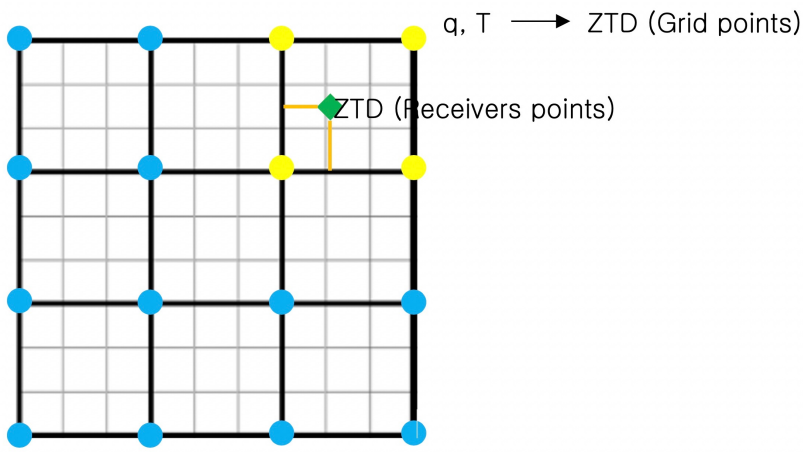

Fig. 5.4: Example transformation grid

- The application of H_{ZTD} matrix to x vector allows the model to obtain, from q and T values in each point of the grid and in each level, the ZTD values in each point (2D grid). In this way, starting from 3D field it was possible to obtain a 2D ZTD field

$$[H_{ZTD}] \times [x] = [H_{ZTD}(x)] \tag{5.6}$$

$$\begin{pmatrix} n_{xy} & n_{xyzvar} \end{pmatrix} \times \begin{pmatrix} n_{xyzvar} \\ \end{pmatrix} = \begin{pmatrix} n_{xy} \\ \end{pmatrix} \tag{5.7}$$

- The application of H_S matrix performs a space interpolation (bi-linear) that extracts the values of ZTD at the np receivers

$$[H_S] \times [H_{ZTD}(x)] = [H(x)] \tag{5.8}$$

$$\begin{pmatrix} n_p & n_{xy} \end{pmatrix} \times \begin{pmatrix} n_{xy} \\ \end{pmatrix} = \begin{pmatrix} n_p \\ \end{pmatrix} \tag{5.9}$$

Until now $J(x)$ function has been defined, now it is necessary to rewrite it in incremental form [32], before minimization. This ensures a better balance of the analysed field and an improved numerical stability of the solution.
For this purpose, it is useful to introduce a new variable ν.
Indicating with x' the difference between the final analysis and the background, or the increment (positive or negative) we should add to the background to have the analysis, the following equations are obtained:

$$x - x_b = x' \tag{5.10}$$

$$x = x' + x_b \tag{5.11}$$

The new variable ν is introduced by:

$$x' = U \times \nu \tag{5.12}$$

where U is a transformation to be determined and is chosen to satisfy the relationship:
$B = U \times U^T$
this means:
$B^{-1} = (U^T)^{-1} \times U^{-1}$
As a consequence of the above transformation the cost-function J(x) becomes a function of ν, i.e $J(\nu)$.

$$2J(\nu) = \nu^T U^T B^{-1} U\nu + (H(x' + x_b) - y_o)^T R^{-1}(H(x' + x_b) - y_o \tag{5.13}$$

Consequently

$$J(\nu) = 1/2\nu^T U^T (U^T)^{-1} U^{-1} U\nu + 1/2(H(x'+x_b)-y_o)^T R^{-1}(H(x'+x_b)-y_o) \tag{5.14}$$

As the product between a matrix and its inverse is the identity matrix, the equation becomes:

$$J(\nu) = 1/2\nu^T\nu + 1/2(H(x'+x_b)-y_o)^T R^{-1}(y_o - HU\nu) \tag{5.15}$$

At this point the model error term in $J(x)$ has been diagonalized. It is now possible to develop by Taylor series:
$H(x'+x_b) = H(x_b) + (\delta H/\delta x)x'$
where $j = (\delta H/\delta x)$ is the jacobian of the transformation H.
Actually, it is possible to write:

$$2J(\nu) = \nu^T\nu + (H(x_b) - y_o + jU\nu)^T R^{-1}(H(x_b) - y_o + jU\nu) \tag{5.16}$$

where $H(x_b) = FG$ (First Guess) and $\nu[n_{xyzvar}]$ is equal to 0 at the initial iteration of the minimization of the cost-function.
It is, now, advisable to put: $H(x_b) - y_o = -y'_o$, or rather $y'_o = y_o - FG$
This implies that the expression becomes:

$$2J(\nu) = \nu^T\nu + (-y'_o + jU\nu)^T R^{-1}(-y'_o + jU\nu) = \tag{5.17}$$

$$= \nu^T\nu - (y'_o - jU\nu)^T R^{-1}[-(y'_o - jU\nu)] = \tag{5.18}$$

$$= \nu^T\nu + (y'_o - jU\nu)^T R^{-1}(y'_o - jU\nu) \tag{5.19}$$

With $x' = U\nu = x - x_b$ and $x = x_b + U\nu$.

The minimization of the function $J(\nu)$ results in obtaining ν value, and consequently x' (by the application of U). By adding x_b to x' it is possible to obtain the analysis x (for reasons of simplicity from here on out x_a).
U transformation has a really big dimension $[n_{xyzvar}, n_{xyzvar}]$which means [734472, 734472]. This matrix is not even dimensionable by computer. To solve this problem, it is appropriate to decompose it: $U = U_\nu \times U_h$; this is not a simple matrix product (block diagonal form) and:
$U_\nu[n_z, n_z]$
$U_h[n_{xy}, n_{xy}]$
It is fundamental to remind that $B = U \times U^T$.
B_h matrix has only correlation coefficients (pure correlation error on the horizontal component); its dimension is $[101^2, 101^2]$.
To discuss more in detail the above transformation it is possible to note that the B matrix is decomposed in the three spatial directions $B = B_z B_y B_x$. The B_x and B_y matrices depend on the spatial distance between two grid-points and represent the background error correlation length scale.
For these matrices, a Gaussian form is assumed:

$$B_x = e^{x^2/2L_x^2}; B_y = e^{y^2/2L_y^2} \tag{5.20}$$

where L_x and L_y are the background error length-scales that are determined by the National Meteorological Center (NMC) method [79]. The B_x and B_y matrices are symmetric and positive defined.
In this sense it is possible to describe B_h correlation matrix as:

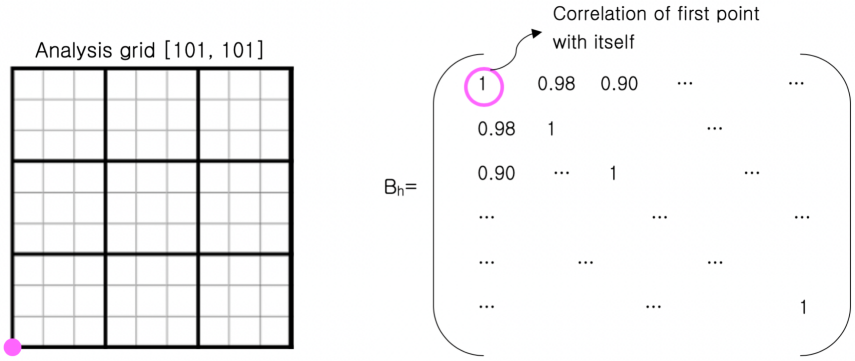

Fig. 5.5: B_h matrix

$$e^{-dist^2/2\sigma^2} \tag{5.21}$$

where dist is the distance between the 2 points in km, and σ is the typical distance of Gaussian decay in km ($\sigma_q = 60km, \sigma_T = 100km$). B_h is therefore symmetrical and defined as positive, which means it has an orthonormal basis:
$B_h = E_h \times \lambda_h \times E_h^T$
where E has all eigenvectors placed in columns; each eigenvector is a column of $101 \times 101 = 10201$ values.
It is clear that the envisaged procedure can be conceptually reduced to one of the many applications of the Bayesian approach to estimation when both the prior distribution and the error law are normal. Indeed, in this case

$$p(x) = ce^{-1/2(x-x_b)B^{-1}(x-x_b)} \tag{5.22}$$

plays the role of the prior, while

$$L(y_o|x) = ce^{-1/2\epsilon^T R^{-1}\epsilon} \tag{5.23}$$

$$\epsilon = y_o - H(x) \tag{5.24}$$

plays the role of the observational wise distribution, for a likelihood of the above form. Therefore B represents the covariance of the prior information summarized into the background vector x_b, while R represents the covariance of the observation errors. The second is relatively small and in any way can be approximated by a known diagonal matrix to a sufficient degree of approximation, whereas the first is neither small, nor well known. Indeed, x_b synthetizes the prior (background) information that comes from the processing of pure meteorological data, where noise and its propagation are not under control. Therefore the procedure hereafter outlined is to rely on a simple empirical covariance summarizing the known properties of the error in the meteorological prediction. This can be represented by two parameters, the variance of the point prediction and the correlation lenght of the error. These will be incorporated into B, as derived from a Gaussian covariance, according to the discussion.
λ_h is a matrix characterized by having all eigenvalues on the diagonal, elsewhere zeros:

$$\lambda = \begin{pmatrix} \lambda_1 & 0 & 0 \\ 0 & ... & 0 \\ 0 & ... & \lambda_{nxy} \end{pmatrix} \tag{5.25}$$

At this point since clearly

$$\lambda_h^{1/2} = (\lambda_h^{1/2})^T \tag{5.26}$$

it is possible to write

$$\lambda_h = \lambda_h^{1/2} \times \lambda_h^{1/2} = \lambda_h^{1/2} \times (\lambda_h^{1/2})^T \tag{5.27}$$

therefore

$$B_h = E_h \times \lambda_h^{1/2} \times (\lambda_h^{1/2})^T \times E_h^T = U_h \times (U_h)^T \tag{5.28}$$

As regards the vertical component(B_ν matrix), it is possible to apply a similar procedure including, this time, the model error.
B_ν has dimension $[n_z, n_z] = [36, 36]$ and has the following form.

$$B_\nu(z_1,z_2) = \sigma_1 \times \sigma_2 \times e^{-((z_2-z_1)/0.5Km)^2} \tag{5.29}$$

where: z_1, z_2 are two generic levels.
σ_q related to generic level is $\sigma_q(z)$ [kg/kg], which is obtained as follows by a sensitivity test.

$$\sigma_q(z) = 8 \times 10^{-3} \times e^{-\sqrt{z/2}} \tag{5.30}$$

This formula has the purpose of limiting the rate of decrease of sigma with the altitude and is graphically illustrated in the Figure 5.6. σ_T is always $4°C$ for each level (we are overestimating, but lowering this threshold reduces too much the correction).
Therefore:

$$B_\nu = \begin{pmatrix} \sigma_1^2 & \sigma_1\sigma_2 e^{-(...)^2} & ... \\ \sigma_2\sigma_1 e^{-(...)^2} & \sigma_2^2 & ... \\ ... & ... & \sigma_{nz}^2 \end{pmatrix} \tag{5.31}$$

This is a symmetric positive defined matrix; it is a covariance matrix

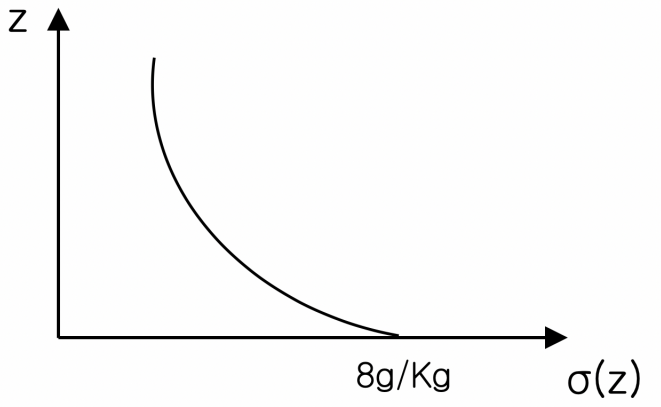

Fig. 5.6: $\sigma - z$ relation for the water vapor mixing ratio

and contains the information about model errors.

$$B_\nu = E_\nu \times \lambda_\nu \times E_\nu^T = \tag{5.32}$$

$$= E_\nu \times \lambda_\nu^{1/2} \times (\lambda_\nu^{1/2})^T \times E_\nu^T = U_\nu \times U_\nu^T \tag{5.33}$$

Moreover:

$$2J(\nu) = \nu^T \nu + (y_o' - jU_\nu U_h \nu)^T R^{-1} (y_o' - jU_\nu U_h \nu) \tag{5.34}$$

where:
$U_\nu = E_{nu} \times \lambda_\nu^{1/2}$
$U_h = E_h \times \lambda_h^{1/2}$
$j = j_S \times j_{ZTD}$

The application of j_{ZTD} matrix to $U_\nu \times U_h \times \nu$ allows the model to obtain:

$$[j_{ZTD}] \times [U_\nu \times U_h \times \nu] = [j_{ZTD} \times U_\nu \times U_h \times \nu] \tag{5.35}$$

$$\begin{pmatrix} n_{xy} & n_{xyzvar} \end{pmatrix} \quad \times \begin{pmatrix} n_{xyzvar} \\ \end{pmatrix} \quad = \begin{pmatrix} n_{xy} \\ \end{pmatrix} \tag{5.36}$$

The application of j_S matrix performs a space interpolation that extracts the values of $j \times U \times \nu$

$$\begin{pmatrix} n_p & n_{xy} \end{pmatrix} \quad \times \begin{pmatrix} n_{xy} \\ \end{pmatrix} \quad = \begin{pmatrix} n_p \\ \end{pmatrix} \tag{5.37}$$

By the method of conjugated gradient [107] it is possible to obtain the minimum value of $J(\nu)$ and the value ν_{min} which minimizes the J function.

At this point it is simple to get x_a value by the following procedure:

$x' = U \times \nu = U_\nu \times U_h \times \nu_{min}$

$x_a = x = x' + x_b$

To minimize the function $J(\nu)$ it is necessary to calculate its gradient in order to use the conjugate gradient method.

If $f(x) = x^T \times x + x^T \times A \times x$, where x is a vector and A is a constant square matrix with dimensions compatible with the vector x, it is possible to write:

$$\nabla_x f(x) = 2x + 2Ax \tag{5.38}$$

Actually, taking into account the above equation:

$$\nabla_\nu J(\nu) = \nu - (jU_\nu U_h)^T R^{-1}(y'_o - jU_\nu U_h \nu) = \tag{5.39}$$

$$= \nu - U_h^T U_\nu^T j_{ZTD}^T j_S^T R^{-1}(y'_o - j_S j_{ZTD} U_\nu U_h \nu) \tag{5.40}$$

5.2 Regional Atmospheric Modelling System

RAMS model in a version maintained and developed, starting from the RAMS 6.0 model [31], at ISAC-CNR was used. This version implements the WRF Singlemoment Microphysics Scheme 6 (WSM6, [58]) [45] and predicts lightning [46]. The list below resumes the physical parameterization schemes used in this research:

- **Parametrized cumulus convection** - Modified Kuo scheme [75]
- **Explicit precipitation parameterization** - Bulk microphysics with six hydrometeors (cloud, rain, graupel, snow, ice, water vapor) [58]
- **Exchange between surface, biosphere and atmosphere** - LEAF3 [112]. LEAF includes prognostic equations for soil temperature and moisture for multiple layers, vegetation temperature and surface water, including dew and intercepted rainfall, snow cover mass and thermal energy for multiple layers, and temperature and water vapor mixing ratio of canopy air
- **Sub-grid mixing** - The turbulent mixing is parameterized in the horizontal [97] and vertical directions [74]
- **Radiation scheme** - The scheme accounts for condensate in the atmosphere, but not for specific optical properties of ice hydrometeors [29]

The grid configuration for the numerical experiments uses two one-way nested grids.
The vertical levels extend from surface to the lower stratosphere and the vertical coordinate is terrain following.

Chapter 6

Near Real-Time transition

The operational system from NRT GNSS meteorology is crucial for supplying information about climate and meteorological activities [76]. In this sense, this is one of the most impactful application; considering, indeed, the advantage of the GPS post-processed data assimilation (e.g. Chapter 7), the operational application of GNSS NRT processing would provide a very meaningful input for NWP models.
Capturing with high spatio-temporal resolution the content of atmospheric water vapor [76], NRT data can be particularly fruitful in case of early warning systems related to intense meteorological events, in order to reduce the risk, providing prompt information on the hazard and thus giving useful indications to limit the injuries.

6.1 Data processing

The methodology for data management described in this chapter is related to the use of GPS constellation only and, in order to process

NRT GPS data, goGPS software was employed.
The main concept of this kind of processing is the application of a 12h moving window (MW), which shifts one by one hour, working in batch (editing multiple data at the same time).

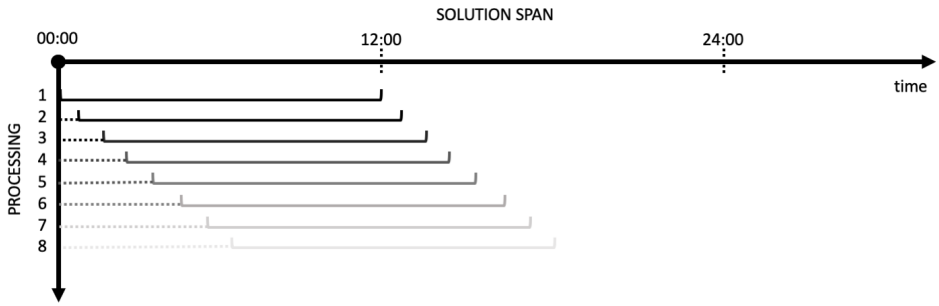

Fig. 6.1: 12h moving window, which shifts one hour by one, working in batch

The method applied is the PPP data processing, which requires high quality products (orbits and clocks) application, since their error directly affect the outputs attributes [53]. To face up this aspect the GNSS orbit and clock correction service, operated by IGS through its Real-time Service (RTS), was employed.
The RTS products consist of GNSS satellite orbit and clock corrections to the broadcast ephemeris.
The product streams available in the RTS are combination solutions generated by processing individual Real Time (RT) solutions from participating Real-time Analysis Centers (RTAC).
In the test described in the following paragraph, the combination experimental product IGS03 (Kalman filter GPS+GLONASS combination), containing GPS and GLONASS corrections was selected.

Data stream is performed by the BNC (BKG NTRIP (Network Transport of RTCM data over IP) Client) which is a program for simultaneously retrieving, decoding, converting and processing real-time GNSS data streams, developed within the framework of the IAG subcommission for Europe (EUREF) and the International GNSS Service (IGS) [114].
A simplified data acquisition scheme is shown in Figure 6.2.

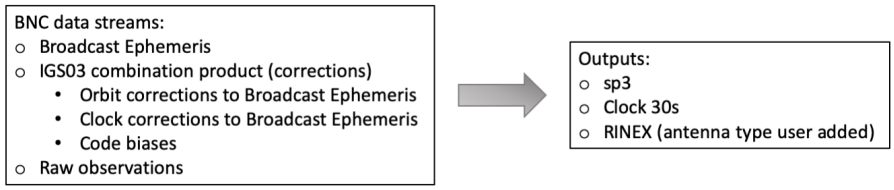

Fig. 6.2: Simplified data acquisition scheme

6.2 Data comparison

For this specific test, two geodetic receivers located in South Africa, respectively at Cape Town (CTWN) and Southerland (SUTM), were used. These two receivers are part of IGS network and for these the CDDIS (Crustal Dynamics Data Information System) provides access to products generated from real-time data streams, in support of the IGS RTS.
To better understand the behaviour of NRT GPS ZTD with respect to

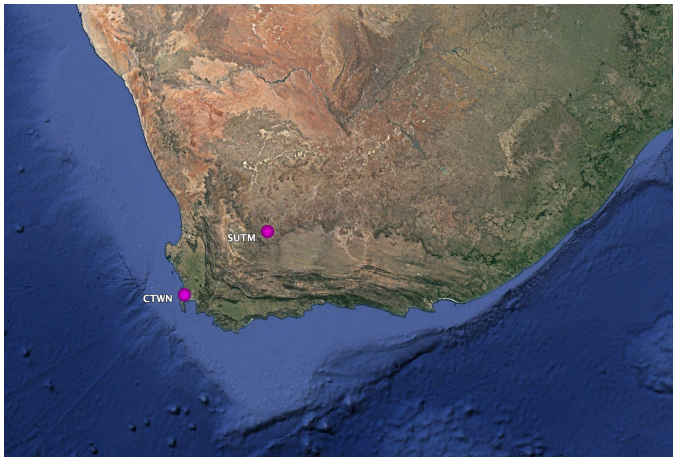

Fig. 6.3: South Africa - Receivers location

post-processed GPS ZTD, two examples are given in Figure 6.4 and Figure 6.5.

Figure 6.4 highlights the peak smoothing in subsequent processing; this peculiar behaviour is closely related to the type of processing, whereas Figure 6.5 shows the case where peaks are not smoothed in subsequent processing; this is mostly due to the orbits effect.

In this sense statistics are provided in order to clarify the two different effects.

Statistics were computed, for each epoch, on differences between NRT GPS ZTD, obtained shifting the 12h moving window, and PP GPS ZTD.

In Figure 6.6 maximum, mean, median and standard deviation plots of differences are given.

As shown in the picture (Figure 6.6), an anomaly may be found at the beginning of the session, then the standard deviation pattern tends to converge in the subsequent one hours. As regards the next hours, it

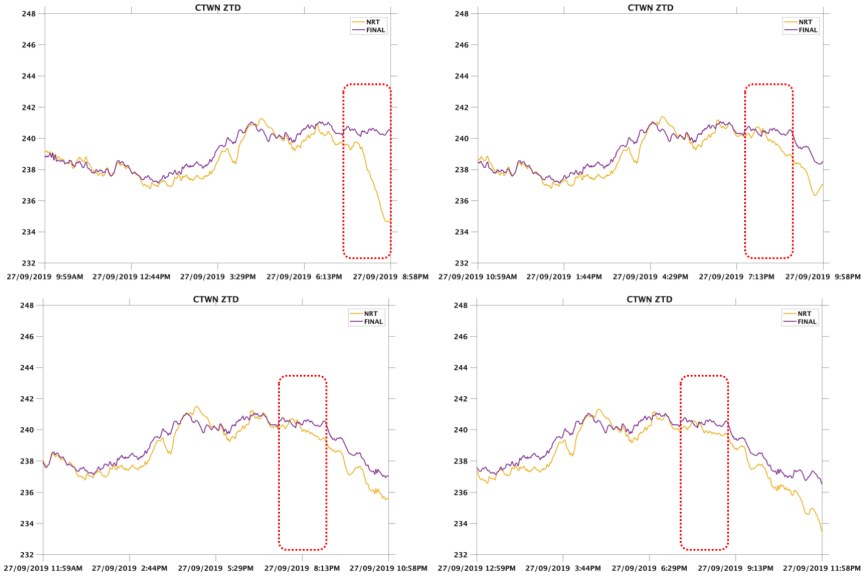

Fig. 6.4: Peak smoothing in subsequent processing

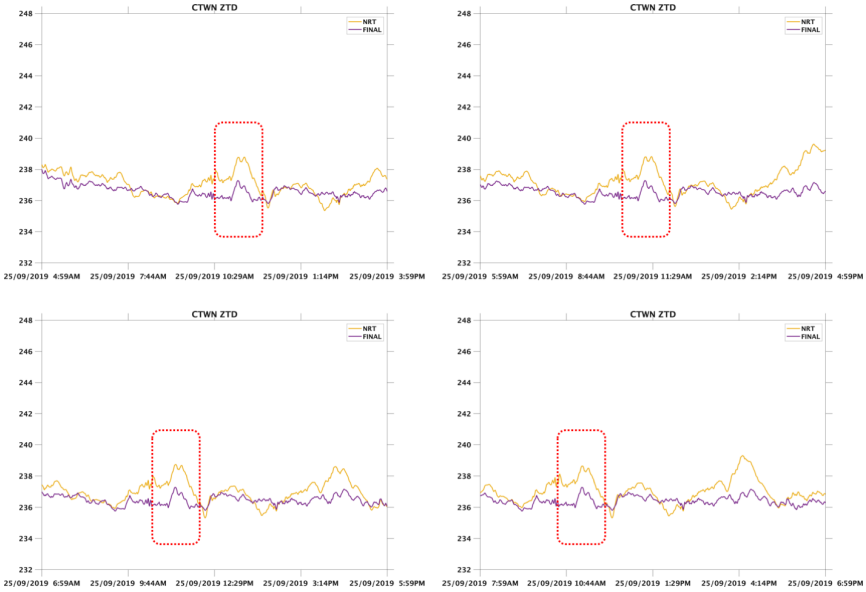

Fig. 6.5: No smoothed peaks in subsequent processing

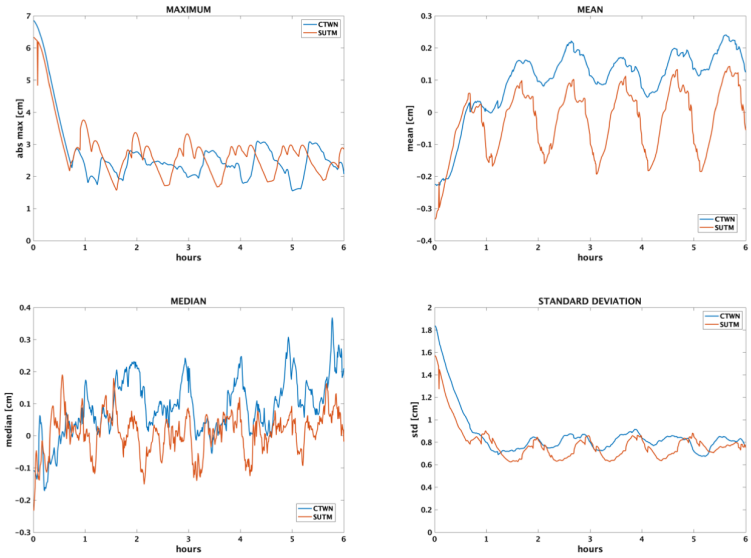

Fig. 6.6: Statistics NRT GPS ZTD - PP GPS ZTD

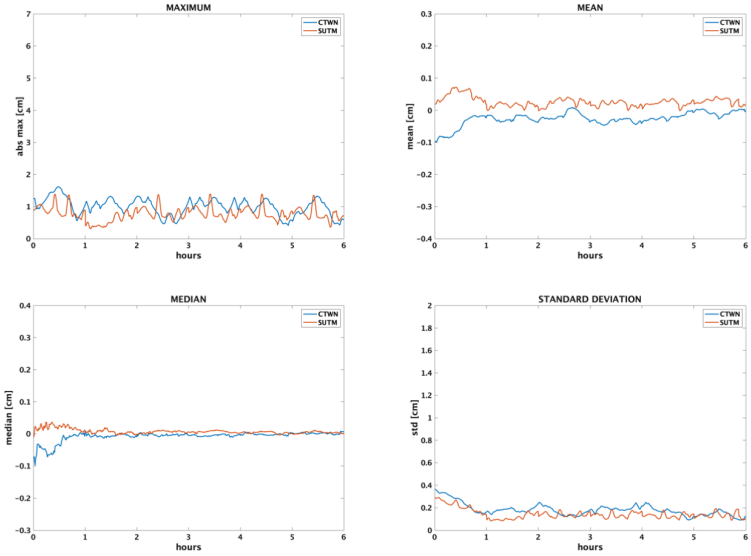

Fig. 6.7: Statistics PPMW GPS ZTD - PP GPS ZTD

is possible to find a periodic behaviour, strictly linked to the moving window approach.
This behaviour was confirmed by a comparison of differences between PPMW GPS ZTD, obtained shifting the 12h moving window, and PP GPS ZTD (Figure 6.7). In this case, indeed, the error threshold is obviously lower but the pattern noticed on differences is consistent with the previous one.
Finally, it can be said that the results obtained match good quality standards, since the RMSE between the solutions obtained in NRT and the PP ones is less than 1 cm starting from the second hour [22]. In scientific literature, indeed, it is possible to find that the accuracy of PP GPS PWV can be as fine as 1.0 mm related to independent techniques, mostly radiosonde [19] [38] [63] [108]; however, some time-critical meteorological applications such as numerical weather prediction nowcasting and severe event monitoring require rapid updates of tropospheric results [39] [37].
The real-time ZTD estimates precision obtained in this test and given in this chapter is characterized with the standard deviation lower than 1 cm starting from the time of convergence (starting from the second hour); this is not far from the target requirements for the operational NWP nowcasting defined as 1 kg/m2 for IWV (6 mm in ZTD) [40] and well below the threshold given in literature by comparing NRT products with respect to the meteorological sensors (PWV≈3mm) [50].

Chapter 7

Case studies

With reference to the themes reported up to this point, it is essential to evaluate the effects of the proposed innovations through case studies aimed at highlighting and quantifying the progress of the branch methodological structure.
Therefore, some examples of the experiments carried out are reported below, accompanied by a brief conceptual introduction and described in their main phases and in the results obtained.

7.1 Data assimilation

Analyses carried out in this paragraph allow to adjust temperature and humidity ranges as a function of additional observations from other sources (e.g. GPS data).
The results obtained in this way make it possible to assess the impact of these innovative technologies in the meteorological field by exploiting validation mechanisms and comparative analysis with data from

sources already widely used.

7.1.1 Lazio Region - July 28th/September 28th, 2017

The knowledge of water vapor distribution is a key element in atmospheric modeling and considerable information, also at the local scale, can be derived from the GPS-ZTD data.
This section shows the assimilation of GPS-ZTD data into the RAMS@ISAC to improve the representation of the water vapor in the meteorological model.
The experiment was performed at a local scale over Lazio Region, in Central Italy, referring to the period July 28^{th}– September 28^{th}, 2017 and using only GPS-ZTD observations for data assimilation.
The network was composed by twenty-nine geodetic receivers from three different permanent networks (ItalPos, Netgeo and Rete Lazio) and three single frequency receivers, which constitute a single frequency receivers pilot network; these receivers are located on the roofs of three buildings in Rome, at inter-distances lower than 15 km: the first one is the Department of Civil, Constructional and Environmental Engineering of Faculty of Civil and Industrial Engineering, Sapienza University of Rome, the second is the Institute of Atmospheric Science and Climate, National Research Council and the last one is the National Institute of Geophysics and Volcanology.
Collected data are processed using RTKLIB software [103] and goGPS software [56].
Starting from the dual-frequency observational files (RINEX Version 3 format) collected by the geodetic receivers at 30 s rate, the PPP tech-

nique [121], undifferenced phase observation processing, was applied using Ionosphere free combination in order to estimate both coordinates and ZTD values for each epoch, by daily processing sessions. As regards the ancillary products (ephemeris and clocks), precise products provided by the CODE were used.
Among the GPS receivers, three are single frequency receivers, able to acquire L1 frequency only.
The same procedure applied for geodetic devices was followed for the three single-frequency receivers, after the reconstruction of L2 synthetic observations, which is achieved by ANGBAS (see Chapter 3) [73]. The validation procedure by other software was conducted only for single frequency devices, whereas for what concerns geodetic receivers, an explanatory test was conducted putting in relation ZTD data obtained by ROUN (one geodetic receiver, belonging to the network used in this study) with official estimations provided by EUREF Permanent GNSS Network for another geodetic receiver, M0SE [73].
These two devices are co-located on the roof of Engineering Faculty of "Sapienza" University of Rome and their comparison, shown in Figure 7.1 reveal great consistency (r=0.99; Mean=-0.0007 m; St.Dev.=0.005 m; RMSE=0.005 m).

As regards the single-frequency validation procedure by goGPS, it was conducted using a PPP batch processing at 30 s rate and ancillary products (ephemeris and clocks) by IGS; in the goGPS processing, the reconstruction of L2 synthetic observations was obtained by SEID (satellite-specific epochdifferenced ionospheric delay) model [120].
The output comparison shows the successful validation of computations (Figure 7.2; Table 7.1) [73].

Therefore, given the consistency of the estimated ZTD at 1 centimeter

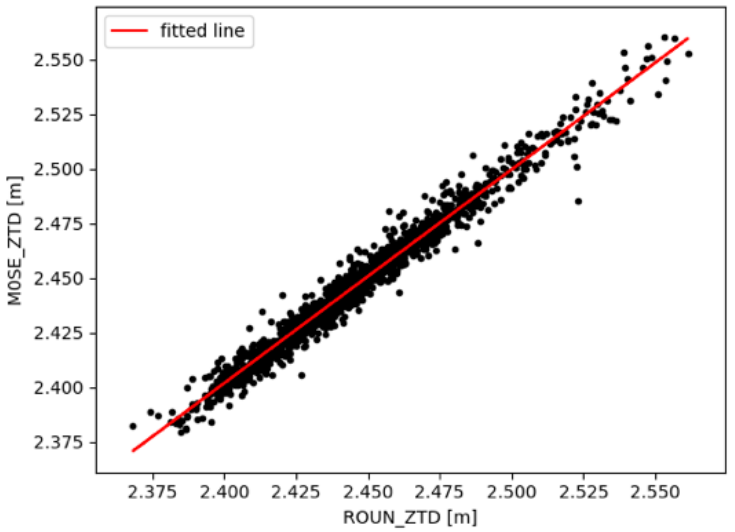

Fig. 7.1: Comparison between ZTD estimation by ROUN and ZTD from EUREF official estimation of M0SE

Tab. 7.1: Statistics related to the difference between goGPS and RTKLIB results

	LOW1	**LOW2**	**LOW3**
Mean (mm)	1	0	-1
St.Dev. (mm)	11	10	12

level, it was chosen to assimilate the results obtained by RTKLIB.

At this point, as an example, a comparative analysis carried out between a single frequency receiver (LOW1) and a geodetic receiver (ROUN), both located on the roof of Engineering Faculty of 'Sapienza' University of Rome, is reported. As it can be seen from the results, LOW1 data show great consistency with those of ROUN, so as to show

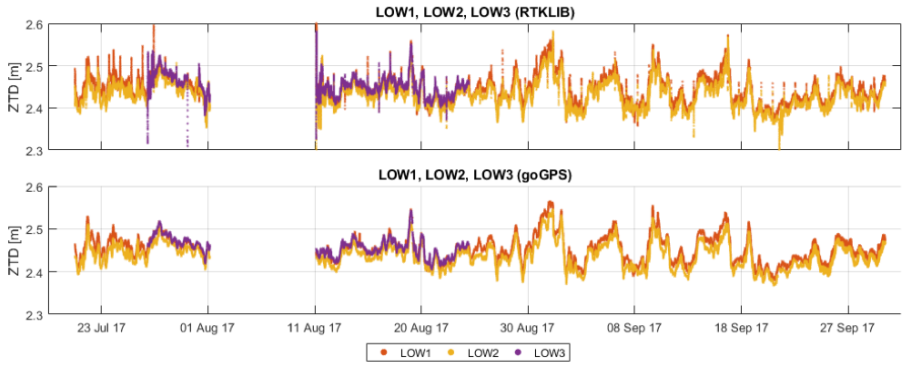

Fig. 7.2: Comparison between single frequency receivers output during the whole period processed by RTKLIB (top) and goGPS (bottom)

a greater agreement between them $[RMSE = 0.61cm]$, compared to the model $[RMSE - LOW1 = 1.87cm, RMSE - ROUN = 1.47cm]$ [73].

Outputs show remarkably that the single frequency receivers can be used in the same way as geodetic devices, in the present context.

RAMS model in a version maintained and developed (starting from the RAMS 6.0 model [31]) at ISAC-CNR was used.

The data assimilation system was based on 3D-Var analysis package (see Chapter 5) [44].

The grid configuration for the numerical experiments uses two one-way nested grids (i.e. Figure 7.4, Table 7.2). The first grid (referred as R10) has 10 km horizontal resolution and covers the Central Mediterranean area.

The second grid (referred as R4) has 4 km horizontal resolution, extends over most of Italy, and it is centered over Central Italy.

The vertical levels are 36 and extend from surface to the lower stratosphere and the vertical coordinate follows territorial topography.

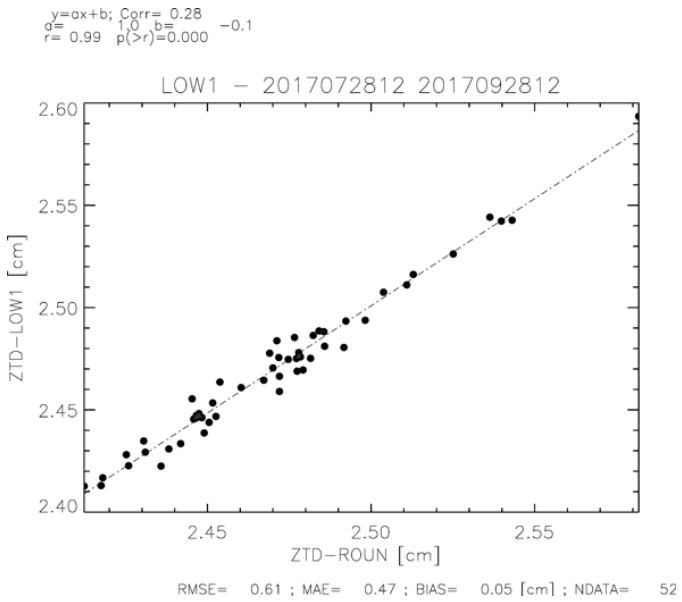

Fig. 7.3: Comparison between ZTD from geodetic receiver (ROUN) and ZTD from single frequency receiver (LOW1)

Using the above configuration, the model run at 10 km horizontal resolution starting at 00 UTC, performing a 15 h forecast on each day of the period considered.

This forecast gave the initial and boundary conditions to the model at 4 km horizontal resolution. More specifically at the 06 UTC on each day, the inner domain was initialized by the R10 model and performed a 9 h forecast (R4 forecast). At 12 UTC, an analysis was made using as background the 6 h short term forecast of R4 and the ZTD data, estimated through GPS, collected at 12 UTC.

Then a short-term 3 h forecast was made, R4_ ANL, and the vertically IWV and ZTD at 12, 13, 14 and 15 UTC were compared between R4 and R4_ ANL, to quantify the benefits of the GPS-ZTD data assimi-

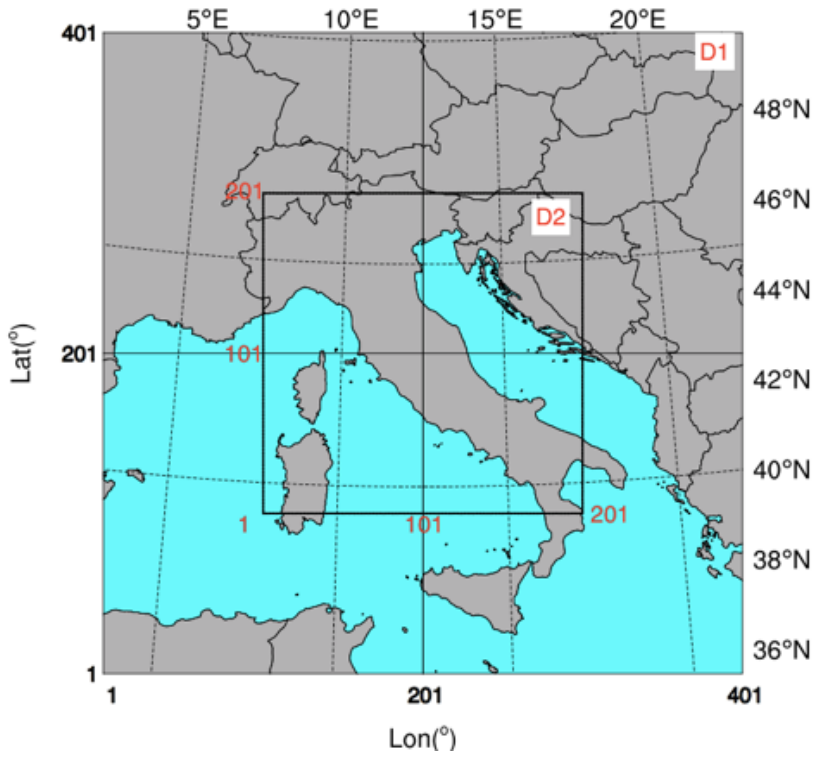

Fig. 7.4: Domains of R10 (D1), R4 and R4_ ANL (D2) forecasts

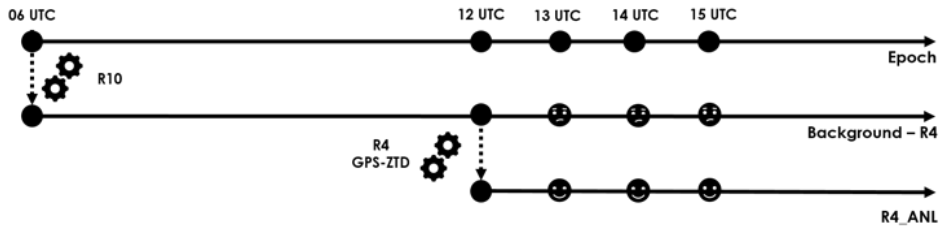

Fig. 7.5: Temporal scheme of the simulations. At 6 UTC of each day a 9 h forecast is performed (R4), using the R10 forecast as initial and boundary conditions. At 12 UTC an analysis is made and a short-term forecast (3 h) starting from this analysis is performed (R4 _ ANL)

lation in the analysis/forecast.
Longer time scales were not considered because the innovations introduced by the GPS-ZTD data are rapidly advected out of the domain where the GPS receivers are located [73]. It is important to remind that in a data assimilation system, the observations are assumed unbiased [70]. In this sense, in order to remove the bias from the observations, the bias between the background and the observations was computed over the whole period and its value for each receiver was determined. After the bias correction, two quality controls were introduced.
This experiment is at 4 km horizontal resolution and the representation of local orography can be rather different from the reality for specific receivers located in complex terrain. To avoid large extrapolation/interpolation of the model output to the receiver location all the receivers having a height that differs by more than 300 m compared to the model surface height were excluded . This left out four receivers belonging to the used permanent network over the Lazio Region, leaving the other twenty-nine receivers of the network.
As stated, among the twenty-nine receivers four were discarded because occurring in the same grid box of other receivers. To avoid introducing excessive departure between the observations and the background, an observation was discarded if its difference with the background was larger than 4 cm. This value, which is more conservative than that used in other studies [8], was found by sensitivity studies, and ensured a reasonable performance of the analysis for days when the background performance was particularly poor [73].
When more than one receiver fall in the same grid cell only one of them is assimilated, however errors are quantified for all receivers, both assimilated and non-assimilated, in order to provide a certain amount of

Tab. 7.2: List of physical parameterizations used for RAMS

Physical parameterization	**Selected scheme**
Parametrized cumulus convection	Modified Kuo scheme [75]. The scheme is applied to R10 only.
Explicit precipitation parameterization	Bulk microphysics with six hydrometeors (cloud, rain, graupel, snow, ice, water vapor) [58].
Exchange between surface, biosphere and atmosphere	LEAF3 [112]. LEAF includes prognostic equations for soil temperature and moisture for multiple layers, vegetation temperature and surface water, including dew and intercepted rainfall, snow cover mass and thermal energy for multiple layers, and temperature and water vapor mixing ratio of canopy air
Sub-grid mixing	The turbulent mixing in the horizontal directions is parameterized [97], vertical diffusion is parameterized [74] and employs a prognostic turbulent kinetic energy
Radiation scheme	The scheme accounts for condensate in the atmosphere, but not for specific optical propertie of ice hydrometeors [29].

crossvalidation.
Performing the analyses, the single frequency receivers were considered the same way as the geodetic receivers.
There are two main reasons for this choice:

- Considering the performance of the background against observations, single frequency receivers did not show any different or specific behavior compared to other receivers (e.g. Figure 7.3).

- An initial test was done where the analyses were performed considering only the geodetic receivers, i.e. without assimilating the single frequency receivers; this test showed that the single frequency receiver observations were closer to the analysis than to the background confirming, indirectly, the possibility to use them the same way as geodetic observations in performing the analysis. This is shown for the LOW1 receiver and for the ZTD in Figure 7.6. The RMSE of the background is 1.74 cm, which reduces to 1.06 cm for the analysis. The correlation coefficient is 0.88 for the background and 0.96 for the analyses [73].

Figure 7.7(a) shows the RMSE of the GPS-ZTD computed for the background and for the whole period at 12 UTC. Its value ranges between 0.9 cm and 2.1 cm, depending on the station.
After the analysis (Figure 7.7(b)), the error is considerably reduced, from 0.3 cm to 1.8 cm.
ZTD error is reduced for all stations.
Similar considerations can be made for the Bias; in particular, the absolute value of the bias decreases for most stations (twenty-one out of twenty-nine) for R4_ ANL compared to R4.

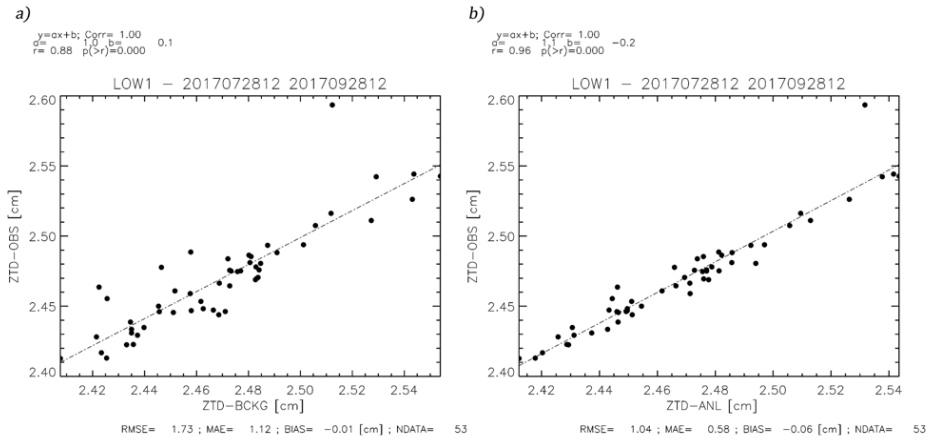

Fig. 7.6: Comparison between the background (Figure 7.6(a)) and analyses (Figure 7.6(b)) with the observations of the LOW1 receiver. For this experiment none of the single frequency receivers were assimilated

The correlation coefficient between R4_ ANL and the observations increases for receivers compared to that between the background and the observations and all the correlation coefficients between R4_ ANL and the observations are larger than 0.9.

The performance of the analysis is quantified also for the IWV, which is computed from the ZTD [16].

The error for the background is shown in Figure 7.7(c), which shows errors ranging from 2.0 mm to 3.6 mm, depending on the station.

The analysis modifies the IWV showing an important impact (Figure 7.7 (d)), with errors ranging from 0.1 mm to 2.4 mm.

For the bias and the correlation coefficient similar considerations to the ZTD can be applied [73].

It is interesting to examine the behavior of the analysis for a specific site for the whole period. In this sense, the ROUN receiver (the posi-

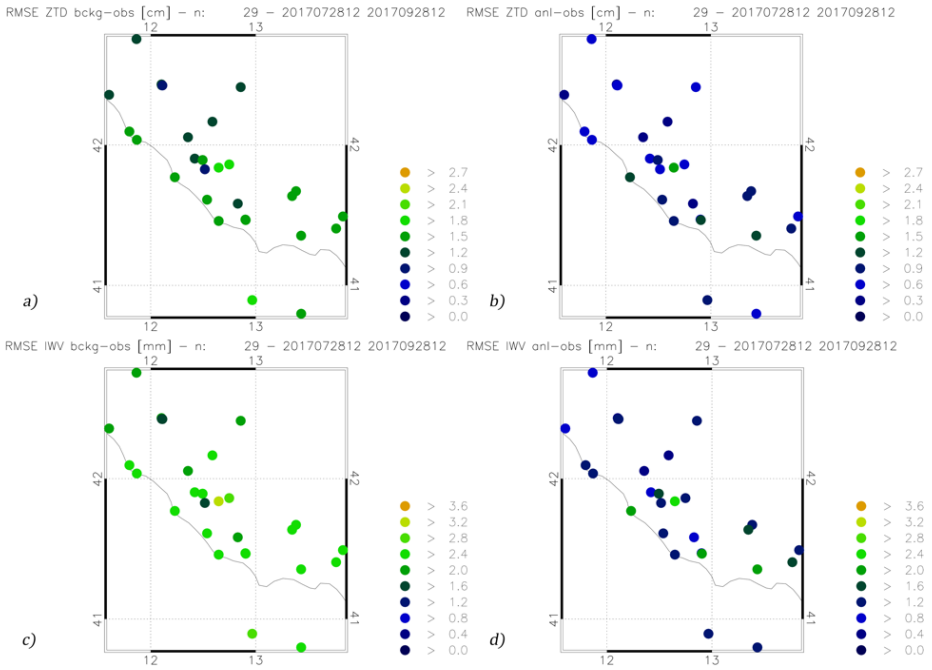

Fig. 7.7: (a) RMSE of the ZTD for the background (R4) computed over the whole period; (b) as in (a) for the analysis (R4_ ANL); (c) RMSE of the IWV for the background (R4) computed over the whole period; (d) as in (c) for the analysis (R4_ ANL).

tion of this station is very close to the LOW1) was chosen because it is representative of the results obtained for most receivers.

Figure 7.8(a) shows the linear regression, for the whole period at 12 UTC, between the ZTD for the background (x-axis) and observations (y -axis).

The correlation coefficient is 0.91, demonstrating the ability of the background to follow the evolution of the ZTD day by day.

There are also outliers of the ZTD estimated by the background, which occur for specific days when the background performance was partic-

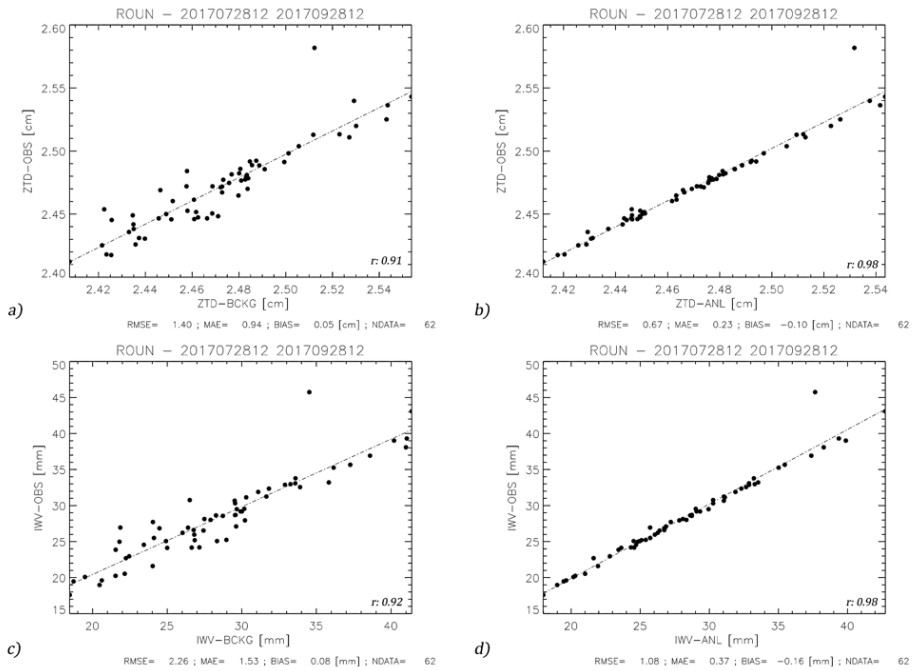

Fig. 7.8: (a) Correlation between the background and the observations for ROUN for ZTD; (b) as in a) for the analysis; (c) correlation between the background and the observations for ROUN for IWV; (d) as in (c) for the analysis

ularly poor.

The correction given by the analysis is significant, as shown in Figure 7.8(b). The correlation coefficient is 0.98 and the RMSE is 0.67 cm, almost halved compared to the background value (Figure 7.8(a)). Figure 7.8(c) and Figure 7.8(d) show the impact of the analysis on the IWV.

The RMSE for the background is 2.3 mm and the correlation coefficient is 0.92, whereas for the analysis the RMSE is 1.1 mm and the correlation coefficient 0.98 [73].

In conclusion all the above results show the important and positive impact of the ZTD data assimilation to define the analysis fields that can be used to initialize the model.

At this point it is possible to show the impact of the assimilation of the GPS-ZTD on the time-series of both the analysis and very short-term forecast (VSF, 1–3 h) of the ZTD and IWV averaged over all the receivers.

For the RAMS simulations, i.e. R4 and R4_ ANL, the fields of ZTD and IWV were first interpolated to the receivers positions, and then the average over all receivers was considered.

For the observations the average over all the receivers was taken into account [73].

Figure 7.9(a) shows the results for the ZTD at the analysis time, i.e. 12 UTC. There is a clear day-to-day dependence, which is caused by the variability of the water vapor over the study area.

For some days (for example day 15 and 35), when the error of the control simulation (R4) is larger, the impact of the GPS-ZTD data assimilation is apparent, however for most days it is difficult to see the difference between simulations and observations.

A similar consideration can be applied to IWV (Figure 7.9(b)) [73].

The time series of IWV for R4 and R4_ ANL shows differences between the two simulations of the order of 1 mm (3%–5% of the IWV depending on the day) and for some days larger than 2 mm (6%–10% of IWV depending on the day).

This variation is not negligible because it represents an average over all the receivers and the differences are higher for specific locations [73].

The difference between the analysis and background for ZTD and IWV before and after the analysis can be represented more clearly consid-

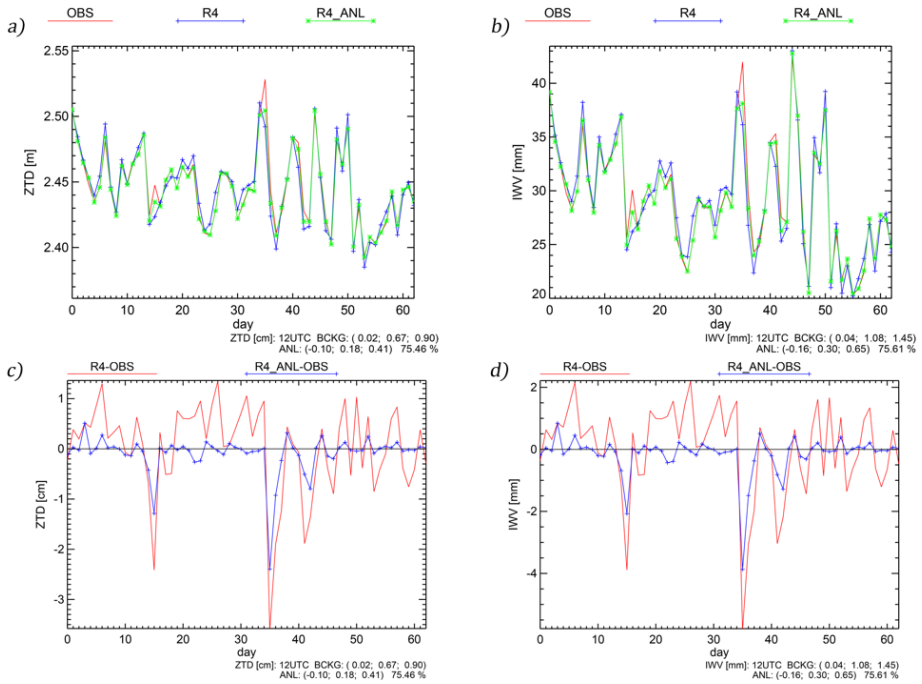

Fig. 7.9: Time series of the R4, R4_ ANL and observations (OBS) for ZTD (Figure (a)), IWV (Figure (b)) and for the differences between R4 and observations and between R4_ ANL and observations for ZTD (Figure (c)) and IWV (Figure (d))

ering the differences between R4 and GPS-derived ZTD and between R4_ ANL and GPS-derived ZTD (Figure 7.9(c) for ZTD and Figure 7.9(d) for IWV).

This representation highlights the improvement of the analysis compared to the background, because the blue line is closer to zero than the red line.

The RMSE for ZTD is 0.90 cm for R4 and 0.41 for R4_ ANL.

For the IWV the RMSE after the analysis is 0.65 mm, while it is 1.45 mm for the background.

The differences between R4 and observations and R4_ ANL and observations at 13 UTC (e.g. for the 1 h forecast) show an improvement of the forecast starting from the GPS-ZTD analysis for both ZTD (Figure 7.10(a)) and IWV (Figure 7.10(b)).

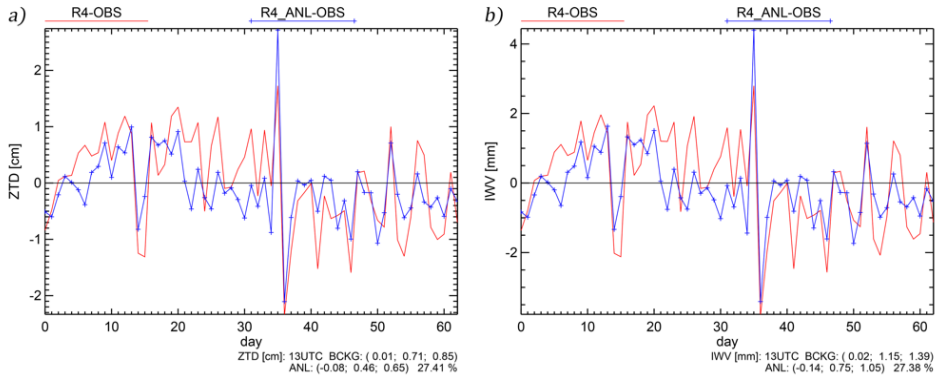

Fig. 7.10: Time series of the differences between R4 and observations and between R4_ ANL and observations for ZTD (Figure (a)) and IWV (Figure (b)). Verification at 1 hour forecast

At this time, there are some days when the forecast starting from the analysis is worse than the background, nevertheless the forecast at 1 h is improved for most days. This is confirmed by the statistics taken over the whole period at 13 UTC (Table 7.4).
For the ZTD, the RMSE is 0.85 cm for R4 and 0.65 cm for R4_ ANL. For IWV, the RMSE at 13 UTC for R4 is 1.4 mm, while it is 1.1 mm for R4_ ANL.
The forecasts at 14 UTC and 15 UTC show characteristics similar to those of 13 UTC, and the forecast starting from the 12 UTC analyses has a lower error compared to the background [73].
Statistics are detailed in Table 7.4.

Tab. 7.3: Basic parameters of the RAMS (R10, R4) grids. NNXP is the number of grid points in the WE direction, NNYP is the number of grid-points in the SN direction, NNZP is the number of vertical levels, DX is the size of the grid spacing in the WE direction, DY is the grid-spacing in the SN direction. L_x, L_y, and L_z are the domain extensions in the NS, WE, and vertical directions. CENTLON and CENTLAT are the coordinates of the grid centres. D1 refers to the first RAMS domain, D2 to the second domain

	D1, R10	**D2, R4/R4_ ANL**
NNXP	301	201
NNYP	301	201
NNZP	36	36
Lx	3000 km	800 km
Ly	3000 km	800 km
Lz	22 400 m	22 400 m
DX	10 km	4 km
DY	10 km	4 km
CENTLAT (°)	43.0 N	43.0 N
CENTLON (°)	12.5 E	12.5 E

The RMSE is reduced by more than 10% of its value for both ZTD and IWV, showing a non-negligible impact of the GPS ZTD data assimilation on the VSF.

In conclusion, results showed that the GPS ZTD data, assimilated by 3D-Var, have an important impact on the analysis of the water vapor field. The effect of the GPS ZTD data assimilation was also evaluated for the VSF (1–3 h), obtaining an improvement of the ZTD and IWV fields for all three hours of forecast [73].

In the end, it is important to point out that he aim to extend the geodetic network with single frequency receivers was to cheaply enhance the

Tab. 7.4: Bias, MAE and RMSE for the analysis and for the three hours of forecast. Statistics are computed for the whole period and are shown for ZTD (Table upper part) and for IWV (Table lower part)

	R4, ZTD (cm)			***R4*$_{ANL}$, ZTD (cm)**		
Time	Bias	MAE	RMSE	Bias	MAE	RMSE
12 UTC	0.02	0.67	0.90	0.10	0.18	0.41
13 UTC	0.01	0.71	0.85	0.08	0.46	0.65
14 UTC	0.20	0.76	0.96	0.14	0.54	0.80
15 UTC	0.12	0.75	0.90	0.07	0.56	0.71

	R4, IWV (mm)			***R4*$_{ANL}$, IWV (mm)**		
Time	Bias	MAE	RMSE	Bias	MAE	RMSE
12 UTC	0.04	1.08	1.45	0.16	0.30	0.65
13 UTC	0.02	1.15	1.39	0.14	0.75	1.05
14 UTC	0.34	1.25	1.56	0.23	0.88	1.30
15 UTC	0.21	1.23	1.47	0.12	0.91	1.16

representation of the atmospheric IWV, which is an important issue over complex terrain, as that considered in this test.
Moreover, the assimilation of GPS-ZTD at the local scale could be important to better predict the precipitation at the local scale.

7.2 Extreme events data comparison

The purpose of following case studies is to improve the knowledge on lightning activity during extreme events by relating it with other parameters such as Precipitable Water Vapor (PWV) and cloud top Brightness Temperature (TB).
The lightning detection is performed by LINET (LIghtning detection

NETwork) [13], a ground network of lightning detectors which covers the entire Italian territory and the seas around it.
Each LINET station has an antenna to detect Very Low Frequency (VLF) and Low Frequency (LF) waves emitted during the flash, a GPS clock, a technical module (amplifier, filter, analog to digital converter) and a transmitter.
Frequency ranges are used to distinguish both Cloud to Ground (CG) and Intracloud (IC) lightning [14].
The events detection is based on a Pseudo-3D algorithm, which consists in three phases: 2D location of the flash through a time of arrival algorithm (TOA), exploitation of the time delay at the sensor nearest to the lightning and time relaxation of the travel path of the radiowave [12].
With the aim of correlating the cloud top temperature with lightning activity, the SEVIRI radiometer has been used.
SEVIRI data were collected every 15 minutes and have been parallax corrected. IR channels 5, 6 and 9 have been used (respectively 6.25, 7.35 and 10.80 μm); in particular, the wavelengths at 6.25 μm and 7.35 μm are centered in the emission spectrum of the water vapor. The two WV channels (channels 5 and 6) determine the water vapor distribution in two distinct layers of the atmosphere and are able to give an indication about the cloud optical depth; the IR channel 9 provide continuous observation of the cloud top temperature.
The last comparison was referred to GNSS; the signal from GPS constellation have been used to estimate the amount of ZTD and, consequently, the PWV.
In this case a post-processing was carried out by RTKLIB, which allowed to obtain ZTD estimations, by a Precise Point Positioning

method, with a time rate of 30 seconds.

7.2.1 Naples - September 5th, 2015

The first case study regards a storm occurred over Naples in September 5^{th}, 2015 which presented a dynamic behaviour.
The convective cell was generated over the sea and then arrived over Naples: the cell covered the area around the GPS dual-frequency receiver, NAPO (part of Campania Region permanent network), from 7:30 to 10:30 UTC.
An intense lightning activity (over 37000 strokes were detected by LINET in 5 hours) and heavy hail were recorded [72]. In Figure 7.11,

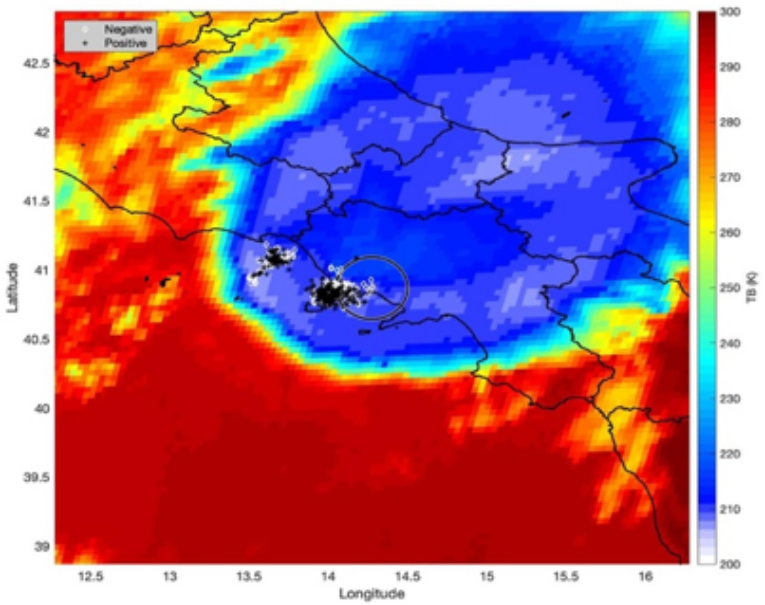

Fig. 7.11: Overview on Naples - September 5^{th}, 2015 09:12 UTC; brightness temperature and strokes

brightness temperature from SEVIRI channel 9 (TBch9) displays in blue the area covered by the cloud with values at the top, below 220K. During the mature phase of the event TBs below 210K, which are considered to be very low in troposphere, are reached.
Red area identifies the clear sky region.
Black and white markers represent positive and negative strokes respectively; their position, always near to the convective cell's border, locate the region of the active updraft which triggers the charging mechanism of the cumulonimbus.
Figure 7.12 shows the comparison between the IC/CG ratio evaluated over the $1°\times1°$ box centred on GPS receiver and the total strokes detected during the storm.
Moreover, grey dashed lines just identify the time interval of interest, while red dashed line represents the mean value of the IC/CG ratio over the $1°\times1°$ box for the whole dataset.
During this event, the IC/CG ratio shows two peaks. Actually, the first at 06:00 UTC occurred with a counting lower than 100 strokes, so it is not meaningful of a strong IC activity. On the other hand, the peak at 09:00 UTC has been reached over a sample of about 2000 strokes and its value, slightly higher than 2.5, evidences the prevalence of IC with respect to CG strokes.
Furthermore, the IC/CG ratio is about 9 times greater if it is compared with the IC/CG ratio mean value over a seven years dataset.
At this point it is possible to discuss the possible relationship existing between ZTD, TB and strokes properties.
Figure 7.13 shows the daily pattern of ZTD (blue line), TBch9 (red line), TB difference between SEVIRI channel 5 and 6 (ΔTB – dotted point light blue line) and total lightning (black line).

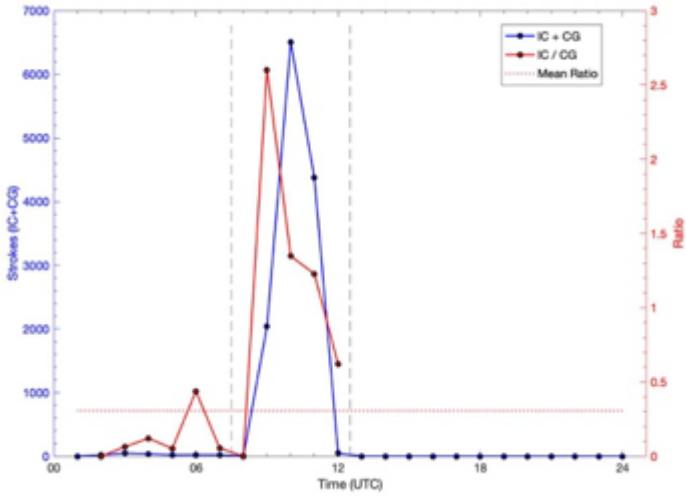

Fig. 7.12: comparison between the IC/CG ratio evaluated over the 1°×1° box centred on GPS receiver and the total strokes detected during the storm

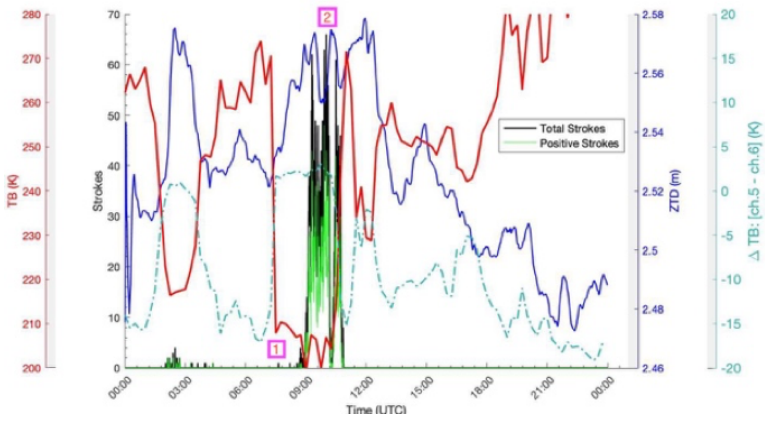

Fig. 7.13: Relationship between ZTD, TB and strokes

It is interesting to observe the presence of two peaks of ZTD, which both coincide with a minimum for the TBch9 and higher values of ΔTB.
It is possible to observe that ΔTB has a similar trend of ZTD and reaches zero or even positive values in two different moments: the first, in coincidence with the low lightning activity around 02:30 UTC, the second around 8:00 UTC, preceding of about one hour the greater lightning activity starting at 09:00 UTC. TBch9 has a specular trend with respect to both ZTD and ΔTB: it reaches its minimum values in coincidence with the lightning activity registered at 02:30 UTC and at 09:00 UTC. The timing of TBch9 starting decreasing is the same of ΔTB starting increasing, as well as the slope of the two curves of that time frame is comparable.

7.2.2 Pineto - September 2nd, 2018

The second case study regards an extreme storm affected Pineto, in Abruzzo Region, in September 2^{nd}, 2018.
The convective cell moved from South-West toward the Adriatic Sea, covering the GPS receiver area between 12:30 and 14:30 UTC, as shown in Figure 7.14.
During its passage, heavy hail caused damages to cars and structures. This storm showed a more static behavior compared to the case study of Naples. Figure 7.14 shows the moment of most intense activity over the GPS antenna, where colder TBs reached values between 240K and 220K.
Black and white markers represent positive and negative strokes respectively.

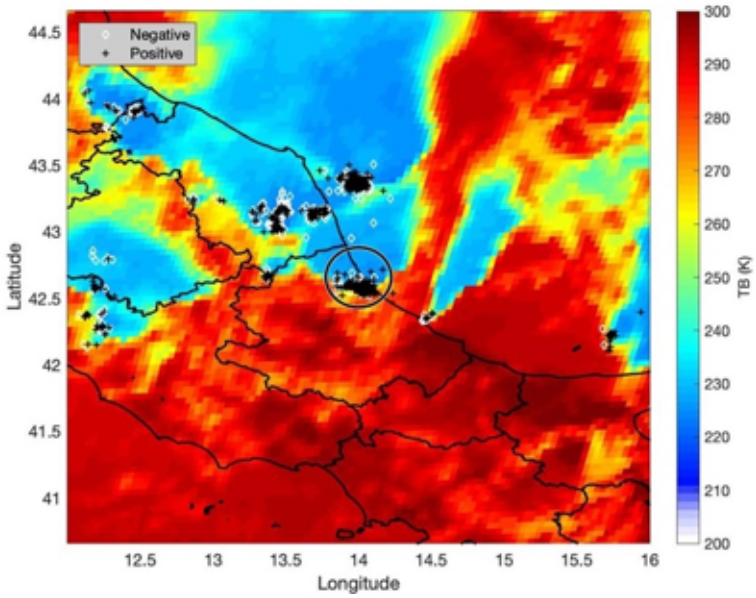

Fig. 7.14: Overview on Pineto - September 2^{nd}, 2018 event; brightness temperature and strokes

Figure 7.15 shows the strokes analysis over the square $1° \times 1°$ for the day of the event (blue line) and the mean IC/CG ratio (red dashed line) evaluated over seven years.
Grey dashed lines just identify the time interval of interest.
This event points out resemblances with the Naples event, indeed in both cases there is one main peak of lightning activity due to a convective cell.

Figure 7.16 shows the result obtained by relating the TB of cloud top for channel 9 (10.8 μm)and the ΔTB between the water vapor channels 5 and 6, as measured by SEVIRI, to both ZTD and total lightning.
During this case study, the peak of lightning activity is preceded by a

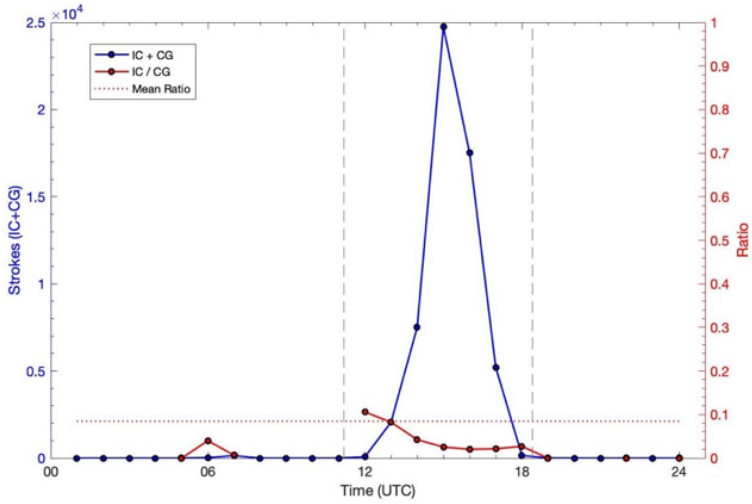

Fig. 7.15: Overview on Pineto - September 2^{nd}, 2018 event; brightness temperature and strokes

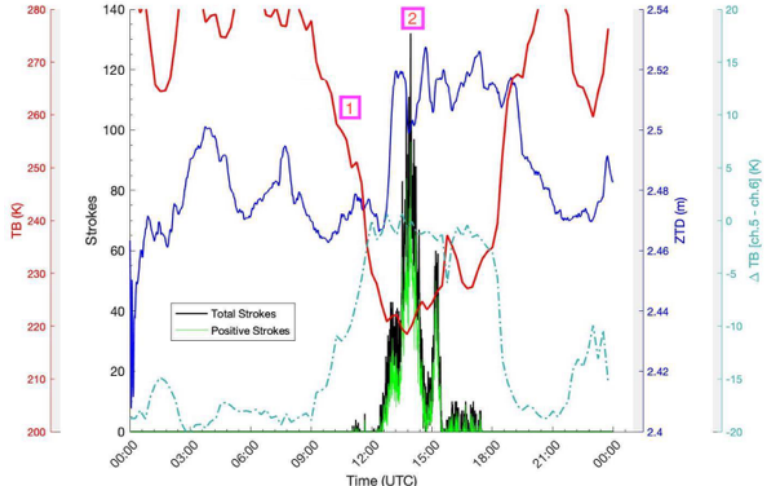

Fig. 7.16: Relationship between ZTD, TB and strokes

drop of TBch9, accompanied by an increase of ΔTB.
The former parameter has a slower decreasing trend if compared with that of the case study of Naples.
This drop of TB goes from 9:30 to 14:00 UTC, while in the previous case study the drop occurred in less than one hour.
This slowness can be explained by the fact that this cell showed a less dynamic behavior compared to that of Naples, where the convective cells passed over the spot during a more mature phase of the storm.

7.2.3 Remarks

This short paragraph had the aim to correlate lightning activity with GPS ZTD data and SEVIRI TB of the cloud top.
The combination of the three parameters shows a pattern in both the considered case studies: the lightning jump is generally preceded by a period in which the ΔTB (i.e. the difference between SEVIRI TB at Channel 5 and Channel 6) shows an almost constant trend with values greater than -5K. When ΔTB reaches this plateau, at the same time (or shortly after), the ZTD starts to increase. The ZTD then reaches a maximum (or a series of maxima) in conjunction with the major lightning activity of the event. This mechanism starts about one hour before the main lightning jump.
Another feature showing similar characteristics among the events is the IC/CG ratio: for both case studies the IC/CG ratio is higher than the mean value calculated over seven years in the same area of study, but presents different magnitudes (going from 0.1 for Pineto up to 2.6 for Naples).
Moreover, the peak of this ratio is reached before the peak of the total

lightning activity.
It is important to remind that the IC detection can be influenced by the neighbourhood of an antenna network (i.e. a LINET antenna). Interesting results were reached and future studies in this topic could help to clarify the most relevant aspects.

Chapter 8

Conclusions

"Migliorare sempre, peggiorare mai."
Daniele Sampietro

GNSS meteorology represents nowadays an impactful application of GNSS technology.
Troposphere, the site of typical weather phenomena, is the atmospheric layer characterized by the presence of water vapor which, interacting with the GNSS signal, can provide interesting information for a number of meteorological applications.
In this thesis, GNSS was proposed as a tool for measuring the tropospheric content of water vapor [16] [15] [4] [100] [21] [66] and several kinds of applications were performed in order to show the great potential of this technique.
The high variability of water vapor [78], both in space and time, requires very dense networks with homogeneous distribution in order to map water vapor with high resolution, also suitable for local level fore-

casting.

In this sense, a pilot permanent network of single-frequency GNSS receivers was installed to densify GNSS permanent networks of geodetic receivers; the performed test, carried out in order to evaluate the data quality and relevance, showed the possibility of using this type of receiver without particular difficulties, using appropriate arrangements (Chapter 3).

Single-frequency data processing, indeed, has opened up interesting investigations about methods of synthetic L2 observations reconstruction. After a benchmarking of methods, performed tests showed that in critical study area, where no more than one geodetic receiver is available, under known conditions, the application of goSEID method can provide good solutions up to about 40 km of distance between geodetic and single-frequency device (ZTD St. Dev.=0.5 cm).

Also a software comparison was performed, highlighting the potential of open source software (Chapter 3).

A reliability analysis of the GPS results was carried out through comparisons with precipitable water vapor measurement sensors (e.g. atmospheric sounding and radiometers), outputs showed PWV St. Dev.$\approx$1 mm in line with mentioned literature [108] [19] [38] [63].

Three calibration and validation tests of sun-sky radiometers (Chapter 4) were performed, also in this case outputs revealed consistence with measurement campaigns performed at mid-latitudes (PWV RMSE $<$ 1 mm) [18] [22] [80].

As regards the comparison with Linet network (Chapter 7), a recursive behaviour in the relationship between occurrence of lightning, SEVIRI TB and ZTD was found. The lightning jump is generally preceded by a period in which the ΔTB (i.e. the difference between SEVIRI TB at

Channel 5 and Channel 6) shows an almost constant trend with values greater than -5K; when ΔTB reaches this plateau, at the same time (or shortly after), the ZTD starts to increase. The ZTD then reaches a maximum (or a series of maxima) in conjunction with the major lightning activity of the event. This interesting aspect, certainly requires further investigation also in view of a possible multi-instrumental assimilation in NWP models.

In this sense, an overview on GPS data assimilation in NWP models (one of the most impactful application of GNSS meteorology [110] [42] [83] [8] [69]) was given (Chapter 5) and a specific case study was analysed (Chapter 7). In the performed test, results showed that the GPS-ZTD data, assimilated by 3D-Var, have an important impact on the analysis of the water vapor field. The effect of the GPS ZTD data assimilation was evaluated for the VSF (1–3 h), obtaining an improvement of the ZTD and IWV fields, with an RMSE reduction of more than 10% of its value, for all three hours of forecast [73].

In order to highlight the great potential and the ongoing development of the presented technology, the near real time data processing was described with a short evaluation of results (Chapter 6). In this case, real-time ZTD estimates precision obtained were characterized by a St. Dev. lower than 1 cm, in accordance with the target requirements for the operational NWP nowcasting (1 kg/m2 for IWV) [40] and well below the threshold given in literature by comparing NRT products with respect to the meteorological sensors (PWV St. Dev.$\approx$ 3mm) [50].

Finally, results provide an overall assessment of the data quality obtained through GPS post-processing and a milestone for NRT processing, also in view of early warning systems.

References

[1] G. A. Una guida completa per capire e leggere un radiosondaggio, 2008. 54

[2] D. Adams, R. Fernandes, K. Holub, S. Gutman, H. Barbosa, L. Machado, A. J. Calhlheiros, R. Bennett, E. Kursinski, L. Sapucci, C. DeMets, G. Chagas, A. Arellano, N. Filizola, A. Rocha, R. Silva, L. Assuncao, G. Cirino, T. Pauliquevis, B. Portela, A. Sa, J. De Sousa, and L. Tanaka. The amazon dense gnss meteorological network: a new approach for examining water vapor and deep convection interactions in the tropics. *Bulletin of the American Meteorological Society*, 96(12):2151–2165, 2015. 4

[3] M. D. Alexandrov, A. Marshak, B. Cairns, A. A. Lacis, and B. E. Carlson. Automated cloud screening algorithm for mfrsr data. *Geophysical research letters*, 31:l04118, 2004. 69

[4] J. Askne and H. Nordius. Estimation of tropospheric delay for microwaves from surface weather data. *Radio Science*, 22:379–386, 1987. 4, 31, 63, 69, 135

[5] Z. Bai and Y. Feng. Gps water vapor estimation using interpolated surface meteorological data from australian automatic

weather stations. *Journal of Global Positioning Systems*, 2(2):83–89, 2003. 30, 31, 63

[6] R. G. Barry and R. J. Chorley. *Atmosphere, weather and climate*. Routledge, 2009. 3, 7, 8, 10, 11, 15, 17

[7] M. Bender, G. Dick, J. Wickert, T. Schmidt, S. Song, G. Gendt, M. Ge, and M. Rothacher. Validation of gps slant delays using water vapour radiometers and weather models. *Meteorologische Zeitschrift*, 17(6):807–812, 2008. 29

[8] G. V. Bennitt and A. Jupp. Operational assimilation of gps zenith total delay observations into the met office numerical weather prediction models. *Monthly Weather Review*, 140(8):2706–2719, 2012. 2, 30, 77, 78, 79, 114, 137

[9] M. Berberan-Santos, E. Bodunov, and L. Pogliani. On the barometric formula. *American Journal of Physics*, 65(5):404–412, 1997. 30, 63

[10] P. Bergthörsson and B. Döös. Numerical weather map analysis. *Tellus*, 7(3):329–340, 1955. 21

[11] H. Betz and B. Meneux. Linet systems-10 years experience. In *2014 International Conference on Lightning Protection (ICLP)*, pages 1553–1557. IEEE, 2014. 20

[12] H. Betz, K. Schmidt, P. Laroche, P. Blanchet, W. Oettinger, and E. Defer. Linet–a new lightning detection network in europe. In *13th International Conference on Atmospheric Electricity*, 2007. 125

[13] H. Betz, K. Schmidt, P. Laroche, P. Blanchet, W. Oettinger, E. Defer, Z. Dziewit, and J. Konarski. Linet—an international lightning detection network in europe. *Atmospheric Research*, 91(2-4):564–573, 2009. 20, 125

[14] H.-D. Betz, K. Schmidt, P. Oettinger, and M. Wirz. Lightning detection with 3-d discrimination of intracloud and cloud-to-ground discharges. *Geophysical research letters*, 31(11), 2004. 125

[15] M. Bevis, S. Businger, S. Chiswell, T. Herring, R. Anthes, C. Rocken, and R. Ware. Gps meteorology: Mapping zenith wet delays onto precipitable water. *Journal of applied meteorology*, 33(3):379–386, 1994. 4, 56, 57, 135

[16] M. Bevis, S. Businger, T. A. Herring, C. Rocken, R. A. Anthes, and R. H. Ware. Gps meteorology: Remote sensing of atmospheric water vapor using the global positioning system. *Journal of Geophysical Research: Atmospheres*, 97:15787–15801, 1992. `https://doi.org/10.1029/92JD01517`. 1, 4, 28, 30, 31, 32, 63, 69, 117, 135

[17] L. Biagi. *I fondamentali del GPS*. Geomatics Workbooks, Vol. 8, 2006. 23, 24, 25, 26, 28, 29

[18] O. Bock, P. Bosser, T. Bourcy, L. David, F. Goutail, C. Hoareau, P. Keckhut, D. Legain, A. Pazmino, J. Pelon, K. Pipis, G. Poujol, A. Sarkissian, C. Thom, G. Tournois, and D. Tzanos. Accuracy assessment of water vapour measurements from in-situ and remote sensing techniques during the demevap 2011 campaign at

ohp. *Atmospheric Measurement Techniques*, 6:2777– 2802, 2013. 69, 136

[19] O. Bock, P. Bosser, R. Pacione, M. Nuret, N. Fourrieé, and A. Parracho. A high-quality reprocessed ground-based gps dataset for atmospheric process studies, radiosonde and model evaluation, and reanalysis of hymex special observing period. *Quarterly Journal of the Royal Meteorological Society*, 142:56–71, 2016. 2, 68, 79, 105, 136

[20] J. Böhm, R. Heinkelmann, and H. Schuh. Short note: a global model of pressure and temperature for geodetic applications. *Journal of Geodesy*, 81(10):679–683, 2007. 4

[21] S. Bonafoni and R. Biondi. The usefulness of the global navigation satellite systems (gnss) in the analysis of precipitation events. *Atmospheric research*, 167:15–23, 2016. 4, 135

[22] S. Bonafoni, A. Mazzoni, D. Cimini, M. Montopoli, N. Pierdicca, P. Basili, P. Ciotti., and G. Carlesimo. Assessment of water vapor retrievals from a gps receiver network. *GPS Solutions*, 17:475–484, 2013. 69, 105, 136

[23] K. Boniface, V. Ducrocq, G. Jaubert, X. Yan, P. Brousseau, F. Masson, C. Champollion, J. Chéry, and E. Doerflinger. Impact of high-resolution data assimilation of gps zenith delay on mediterranean heavy rainfall forecasting. In *Annales Geophysicae*, volume 27, pages 2739–2753, 2009. 78

[24] G. Boudouris. On the index of refraction of air, the absorption

and dispersion of centimeter waves by gasses. *J. Res. Natl. Bur. Stand., Sect.*, 67:631–684, 1963. 57

[25] M. Campanelli, V. Estelleés, C. Tomasi, T. Nakajima, V. Malvestuto, and J. A. Martiiénez-Lozano. Application of the skyrad improved langley plot method for the in situ calibration of cimel sun–sky photometers. *Applied optics*, 46.14:2688–2702, 2007. 67

[26] M. Campanelli, A. Mascitelli, P. Sanò, H. Dieémoz, V. Estelleés, S. Federico, A. M. Iannarelli, F. Fratarcangeli, A. Mazzoni, E. Realini, M. Crespi, O. Bock, J. A. Martìnez-Lozano, and S. Dietrich. Precipitable water vapour content from esr/skynet sun–sky radiometers: validation against gnss/gps and aeronet over three different sites in europe. *Atmospheric Measurement Techniques*, 11:81–94, 2018. 1, 67, 69, 73

[27] M. Campanelli, T. Nakajima, P. Khatri, T. Takamura, A. Uchiyama, V. Estelleés, G. L. Liberti, and M. V. Retrieval of characteristic parameters for water vapour transmittance in the development of ground-based sun–sky radiometric measurements of columnar water vapour. *Atmospheric Measurement Techniques*, 7:1075–1087, 2014. 70, 74

[28] M. Cavcar. The international standard atmosphere (isa). *Anadolu University, Turkey*, 30:9, 2000. 11

[29] C. Chen and W. Cotton. A one-dimensional simulation of the stratocumulus-capped mixed layer. *Boundary-Layer Meteorology*, 25(3):289–321, 1983. 96, 115

[30] G. V. Cooray. *The lightning flash*. Number 34. IET, 2003. 18

[31] W. Cotton, R. Pielke Sr, R. Walko, G. Liston, C. Tremback, H. Jiang, R. McAnelly, J. Harrington, M. Nicholls, G. Carrio, et al. Rams 2001: Current status and future directions. *Meteorology and Atmospheric Physics*, 82(1-4):5–29, 2003. 96, 111

[32] P. Courtier, J.-N. Thépaut, and A. Hollingsworth. A strategy for operational implementation of 4d-var, using an incremental approach. *Quarterly Journal of the Royal Meteorological Society*, 120(519):1367–1387, 1994. 88

[33] R. Dach and P. Walser. Bernese gnss software version 5.2. 2015. 47

[34] J. Davis, T. Herring, I. Shapiro, and A. Rogers. Elgered geodesy by radio interferometry: effects of atmospheric modelling errors on estimates of baseline length. *Radio Science*, 20:1593–1607, 1985. 32, 63, 69

[35] Z. Deng, M. Bender, G. Dick, M. Ge, J. Wickert, M. Ramatschi, and X. Zou. Retrieving tropospheric delays from gps networks densified with single frequency receivers. *Geophysical Research Letters*, 36(19), 2009. 36, 37

[36] H. Diémoz, T. Magri, G. Pession, M. Zublena, M. Campanelli, G. P. Gobbi, F. Barnaba, L. Di Liberto, and D. Dionisi. Thermally-driven advections of aerosol-rich air masses to an alpine valley: Theoretical considerations and experimental evidences. EGU General Assembly, Vienna, 2016. 72

[37] W. Ding, F. N. Teferle, K. Kazmierski, D. Laurichesse, and Y. Yuan. An evaluation of real-time troposphere estimation

based on gnss precise point positioning. *Journal of Geophysical Research: Atmospheres*, 122(5):2779–2790, 2017. 105

[38] J. Dousa. Towards an operational near real-time precipitable water vapor estimation. *Physics and Chemistry of the Earth, Part A: Solid Earth and Geodesy*, 26(3):189–194, 2001. 105, 136

[39] J. Dousa and P. Vaclavovic. Real-time zenith tropospheric delays in support of numerical weather prediction applications. *Advances in Space Research*, 53(9):1347–1358, 2014. 105

[40] J. Dousa, P. Vaclavovic, G. Gyori, and J. Kostelecky. Development of real-time gnss ztd products. In *EGU General Assembly Conference Abstracts*, volume 15, 2013. 105, 137

[41] G. Elgered, J. Davis, T. Herring, and I. Shapiro. Geodesy by radio interferometry: Water vapor radiometry for estimation of the wet delay. *Journal of geophysical research: solid earth*, 96(B4):6541–6555, 1991. 31

[42] C. Faccani, R. Ferretti, R. Pacione, T. Paolucci, F. Vespe, and L. Cucurull. Impact of a high density gps network on the operational forecast. *Advances in Geosciences*, 2:73–79, 2005. 2, 77, 79, 137

[43] S. Federico. Verification of surface minimum, mean, and maximum temperature forecasts in calabria for summer 2008. *Natural Hazards and Earth System Sciences*, 11(2):487–500, 2011. 79

[44] S. Federico. Implementation of a 3d-var system for atmospheric profiling data assimilation into the rams model: initial results.

Atmospheric Measurement Techniques, 6(12):3563–3576, 2013. 78, 79, 111

[45] S. Federico. Implementation of the wsm5 and wsm6 single moment microphysics scheme into the rams model: verification for the hymex-sop1. *Advances in Meteorology*, 2016, 2016. 96

[46] S. Federico, E. Avolio, M. Petracca, G. Panegrossi, P. Sanò, D. Casella, and S. Dietrich. Simulating lightning into the rams model: implementation and preliminary results. *Natural Hazards and Earth System Sciences*, 14(11):2933–2950, 2014. 96

[47] U. C. for Atmospheric Research. Basic satellite imagery interpretation, 2018. ix, 17

[48] A. Gallice, F. Wienhold, C. Hoyle, F. Immler, and T. Peter. Modeling the ascent of sounding balloons: derivation of the vertical air motion. *Atmospheric Measurement Techniques*, 4(10):2235–2253, 2011. 54

[49] C. Griebler, A. Gunatilaka, and J. Notenboom. Present state and future prospects for groundwater ecosystems. *Environmental Conservation*, 30:104 – 130, 06 2003. ix, 15

[50] G. Guerova, J. Jones, J. Dousóa, G. Dick, S. De Haan, E. Pottiaux, O. Bock, R. Pacione, G. Elgered, H. Vedel, and M. Bender. Review of the state of the art and future prospects of the ground-based gnss meteorology in europe. *Atmospheric Measurement Techniques*, 9:5385–5406, 2016. 30, 105, 137

[51] C. Gueymard. The sun's total and spectral irradiance for solar energy applications and solar radiation models. *Solar Energy*, 76:423–453, 04 2004. 11

[52] G. Gurbuz, S. Jin, and C. Mekik. Effects of ocean tide models on gnss-estimated ztd and pwv in turkey. *The International Archives of Photogrammetry, Remote Sensing and Spatial Information Sciences*, 40(1):255, 2015. 4

[53] T. Hadas, J. Kaplon, J. Bosy, J. Sierny, and K. Wilgan. Near-real-time regional troposphere models for the gnss precise point positioning technique. *Measurement Science and Technology*, 24(5):055003, 2013. 100

[54] G. J. Haltiner and F. L. Martín. *Meteorología dinámica y física*. Number 551.51 HAL. 1957. 15

[55] J. E. Harries, J. Russell, J. Hanafin, H. Brindley, J. Futyan, J. Rufus, S. Kellock, G. Matthews, R. Wrigley, A. Last, et al. The geostationary earth radiation budget project. *Bulletin of the American Meteorological Society*, 86(7):945–960, 2005. 11

[56] A. M. Herrera, H. F. Suhandri, E. Realini, M. Reguzzoni, and M. C. de Lacy. gogps: open-source matlab software. *GPS solutions*, 20(3):595–603, 2016. 62, 108

[57] B. Hofmann-Wellenhof, H. Lichtenegger, and J. Collins. Gps theory and practice, 5a revised edit, 2001. 24, 25, 29

[58] S. Hong and J. Lim. The wrf single-moment 6-class microphysics

scheme (wsm6). *Asia-Pacific Journal of Atmospheric Sciences*, 42(2):129–151, 2006. 96, 115

[59] H. Hopfield. Two-quartic tropospheric refractivity profile for correcting satellite data. *Journal of Geophysical research*, 74(18):4487–4499, 1969. 29

[60] O. International. Types of satellites and applications, 2016. 11

[61] E. R. Jayaratne, C. P. R. Saunders, and J. Hallett. Laboratory studies of the charging of soft hail during ice crystal interactions. *Q. J. R. Meteorol. Soc*, 109:609–630, 1983. 18

[62] E. Kalnay. *Atmospheric modeling, data assimilation and predictability*. Cambridge university press, 2003. 20, 21, 79

[63] A. Karabatić, R. Weber, and T. Haiden. Near real-time estimation of tropospheric water vapour content from ground based gnss data and its potential contribution to weather now-casting in austria. *Advances in Space Research*, 47(10):1691–1703, 2011. 105, 136

[64] F. Kleijer. *Troposphere modeling and filtering for precise GPS leveling*. PhD thesis, Delft University of Technology, 2004. 10, 16, 29

[65] J. A. Klobuchar. Ionospheric time-delay algorithm for single-frequency gps users. *IEEE Transactions on aerospace and electronic systems*, (3):325–331, 1987. 28

[66] L. Labbouz, J. Van Baelen, and C. Duroure. Investigation of the links between water vapor field evolution and rain rate based

on 5 years of measurements at a midlatitude site. *Geophysical Research Letters*, 42(21):9538–9545, 2015. 4, 135

[67] A. Leick, L. Rapoport, and D. Tatarnikov. *GPS satellite surveying*. John Wiley & Sons, 2015. 26

[68] H. Liebe, G. Hufford, and M. Cotton. Propagation modeling of moist air and suspended water/ice particles at frequencies below 1000 ghz. In *In AGARD, Atmospheric Propagation Effects Through Natural and Man-Made Obscurants for Visible to MM-Wave Radiation 11 p (SEE N94-30495 08-32)*, 1993. 61

[69] M. Lindskog, M. Ridal, S. Thorsteinsson, and T. Ning. Data assimilation of gnss zenith total delays from a nordic processing centre. *Atmospheric Chemistry and Physics*, 17(22):13983–13998, 2017. 77, 78, 137

[70] A. Lorenc. Analysis methods for numerical weather prediction. *Quarterly Journal of the Royal Meteorological Society*, 112(474):1177–1194, 1986. 114

[71] L. Luini, C. Riva, C. Capsoni, and A. Martellucci. Attenuation in nonrainy conditions at millimeter wavelengths: Assessment of a procedure. *IEEE Transactions on Geoscience and Remote Sensing*, 45(7):2150–2157, 2007. 61

[72] A. Marra, F. Porcù, L. Baldini, M. Petracca, D. Casella, S. Dietrich, A. Mugnai, P. Sanò, G. Vulpiani, and G. Panegrossi. Observational analysis of an exceptionally intense hailstorm over the mediterranean area: Role of the gpm core observatory. *Atmospheric research*, 192:72–90, 2017. 126

[73] A. Mascitelli, S. Federico, M. Fortunato, E. Avolio, R. C. Torcasio, E. Realini, A. Mazzoni, C. Transerici, M. Crespi, and S. Dietrich. Data assimilation of gps-ztd into the rams model through 3d-var: preliminary results at the regional scale. *Measurement Science and Technology*, 2019. 36, 37, 79, 80, 109, 111, 114, 116, 117, 119, 120, 122, 123, 137

[74] G. Mellor and T. Yamada. Development of a turbulence closure model for geophysical fluid problems. *Reviews of Geophysics*, 20(4):851–875, 1982. 96, 115

[75] J. Molinari and T. Corsetti. Incorporation of cloud-scale and mesoscale downdrafts into a cumulus parameterization: Results of one-and three-dimensional integrations. *Monthly Weather Review*, 113(4):485–501, 1985. 96, 115

[76] M. Norazmi, Y. Opaluwa, and R. Musa, T.and Othman. The concept of operational near real-time gnss meteorology system for atmospheric water vapour monitoring over peninsular malaysia. *Arabian Journal for Science and Engineering*, 40:235–244, 01 2015. 99

[77] R. Notarpietro, M. Cucca, M. Gabella, G. Venuti, and G. Perona. Tomographic reconstruction of wet and total refractivity fields from gnss receiver networks. *Advances in Space Research*, 47(5):898–912, 2011. 29

[78] R. Pacione, A. Araszkiewicz, E. Brockmann, and J. Dousa. Epnrepro2: A reference gnss tropospheric data set over europe. *Atmospheric Measurement Techniques*, 10(5):1689, 2017. 4, 135

[79] D. F. Parrish and J. C. Derber. The national meteorological center's spectral statistical-interpolation analysis system. *Monthly Weather Review*, 120(8):1747–1763, 1992. 90

[80] D. Pérez-Ramìrez, D. N. Whiteman, A. Smirnov, H. Lyamani, B. N. Holben, R. Pinker, M. Andrade, and L. Alados-Arboledas. Evaluation of aeronet precipitable water vapor versus microwave radiometry, gps, and radiosondes at arm sites. *Journal of Geophysical Research: Atmospheres*, 119.15:9596–9613, 2014. 69, 72, 136

[81] M. Petracca. *Studio dell'attività elettrica nelle nubi temporalesche ed utilizzo dei dati di fulminazione per la meteorologia operativa*. PhD thesis, Università degli studi di Ferrara, 2016. 13, 18, 19

[82] F. Pettenati, M. Bobbio, M. Busetti, and L. Facchin. Metodi di contour a confronto. una interpretazione del basamento del victoria land basin (mare di ross-antartide). x, 59

[83] P. Poli, P. Moll, F. Rabier, G. Desroziers, B. Chapnik, L. Berre, S. Healy, E. Andersson, and F. El Guelai. Forecast impact studies of zenith total delay data from european near real-time gps stations in météo france 4dvar. *Journal of Geophysical Research: Atmospheres*, 112(D6), 2007. 77, 78, 137

[84] F. Rawlins, S. Ballard, K. Bovis, A. Clayton, D. Li, G. Inverarity, A. Lorenc, and T. Payne. The met office global four-dimensional variational data assimilation scheme. *Quarterly Journal of the Royal Meteorological Society*, 133(623):347–362, 2007. 78

[85] E. Realini, K. Sato, T. Tsuda, and T. Manik. An observation campaign of precipitable water vapor with multiple gps receivers in western java, indonesia. *Progress in Earth and Planetary Science*, 17:20141, 2014. 30, 57, 63, 69

[86] N. Rebora, L. Molini, E. Casella, A. Comellas, E. Fiori, F. Pignone, F. Siccardi, F. Silvestro, S. Tanelli, and A. Parodi. Extreme rainfall in the mediterranean: What can we learn from observations? *Journal of Hydrometeorology*, 14(3):906–922, 2013. x, 55

[87] W. Rohm and J. Bosy. The verification of gnss tropospheric tomography model in a mountainous area. *Advances in Space Research*, 47:1721–1730, 2011. 1

[88] J. Saastamoinen. Contributions to the theory of atmospheric refraction. *Bulletin Géodésique*, 107.1:13–14, 1973. 28, 29

[89] E. Salonen and S. Uppala. New prediction method of cloud attenuation. *Electronics Letters*, 27(12):1106–1108, 1991. 61

[90] F. Sansò. *La teoria della stima.* Cittàstudi, 1996. 49

[91] F. Sansò. *Navigazione geodetica e rilevamento cinematico.* Polipress, 2006. 48

[92] P. Sarti, M. Negusini, C. Tomasi, B. Petkov, and A. Capra. Thirteen years of integrated precipitable water derived by gps at mario zucchelli station, antarctica. *Annals of Geophysics*, 56(2):0221, 2013. 4

[93] K. Sato, E. Realini, T. Tsuda, M. Oigawa, Y. Iwaki, Y. Shoji, and H. Seko. A high-resolution, precipitable water vapor monitoring system using a dense network of gnss receivers. 2013. 55

[94] Y. Shoji. Retrieval of water vapor inhomogeneity using the japanese nationwide gps array and its potential for prediction of convective precipitation. *Journal of the Meteorological Society of Japan. Ser. II*, 91(1):43–62, 2013. 4

[95] R. Sibson. A vector identity for the dirichlet tessellation. In *Mathematical Proceedings of the Cambridge Philosophical Society*, volume 87, pages 151–155. Cambridge University Press, 1980. 59

[96] L. Sirovich, F. Cavallini, F. Pettenati, and M. Bobbio. Natural-neighbor isoseismals. *Bulletin of the Seismological Society of America*, 92(5):1933–1940, 2002. x, 59

[97] J. Smagorinsky. General circulation experiments with the primitive equations: I. the basic experiment. *Monthly weather review*, 91(3):99–164, 1963. 96, 115

[98] A. Smirnov, B. N. Holben, A. Lyapustin, I. Slutsker, and E. T. F. Aeronet processing algorithms refinement. *Proceedings of AERONET workshop, NASA/GSFC AERONET project, El Arenosillo, Spain*, pages 10–14, 2004. 67

[99] E. K. Smith and W. Stanley. The constants in the equation for atmospheric refractive index at radio frequencies. *Proceedings of the IRE*, 41.8:1035–1037, 1953. 14, 57

[100] S. Steinke, S. Eikenberg, U. Löhnert, G. Dick, D. Klocke, P. Di Girolamo, and S. Crewell. Assessment of small-scale integrated water vapour variability during hope. *Atmospheric Chemistry and Physics*, 15(5):2675–2692, 2015. 4, 135

[101] M. Stolzenburg, W. D. Rust, and T. C. Marshall. Electrical structure in thunderstorm convective regions. 3. synthesis. *Journal of Geophysical Research: Atmospheres*, 103:14097–14108, 1998. ix, 19

[102] T. Takahashi. Riming electrification as a charge generation mechanism in thunderstorms. *J. Atmos. Sci.*, 35:1536–1548, 1978. 18

[103] T. Takasu and A. Yasuda. Development of the low-cost rtk-gps receiver with an open source program package rtklib. In *International symposium on GPS/GNSS*, pages 4–6. International Convention Center Jeju Korea, 2009. 48, 108

[104] O. Talagrand. Assimilation of observations, an introduction (gtspecial issueltdata assimilation in meteology and oceanography: Theory and practice). *Journal of the Meteorological Society of Japan. Ser. II*, 75(1B):191–209, 1997. 20

[105] T. A. Talay. *Introduction to the Aerodynamics of Flight*. Scientific and Technical Information Office, National Aeronautics and Space Administration, 1975. 10

[106] U. Tammaro, U. Riccardi, F. Masson, P. Capuano, and J. Boy. Atmospheric precipitable water in somma-vesuvius area during extreme weather events from ground-based gps measurements. In

International Symposium on Earth and Environmental Sciences for Future Generations, pages 293–302. Springer, 2016. 4

[107] S. A. Teukolsky, B. P. Flannery, W. H. Press, and W. T. Vetterling. Numerical recipes in c. *SMR*, 693(1):59–70, 1992. 95

[108] J. Van Baelen, J.-P. Aubagnac, and A. Dabas. Comparison of near-real time estimates of integrated water vapor derived with gps, radiosondes, and microwave radiometer. *Journal of Atmospheric and Oceanic Technology*, 22(2):201–210, 2005. 105, 136

[109] H. Vedel. Conversion of wgs84 geometric heights to nwp model hirlam geopotential heights, danish meteorological institute. *DMI scientific report*, pages 00–04, 2000. 58

[110] H. Vedel and X. Huang. Impact of ground based gps data on numerical weather prediction. *Journal of the Meteorological Society of Japan. Ser. II*, 82(1B):459–472, 2004. 5, 77, 137

[111] H. Vedel, K. Mogensen, and X. Huang. Calculation of zenith delays from meteorological data comparison of nwp model, radiosonde and gps delays. *Physics and chemistry of the earth, part A: solid earth and geodesy*, 26(6-8):497–502, 2001. 43, 57, 58

[112] R. Walko, L. Band, J. Baron, T. Kittel, R. Lammers, T. Lee, D. Ojima, R. Pielke Sr, C. Taylor, C. Tague, et al. Coupled atmosphere–biophysics–hydrology models for environmental modeling. *Journal of applied meteorology*, 39(6):931–944, 2000. 96, 115

[113] P.-H. Wang, P. Minnis, B. A. Wielicki, T. Wong, and L. B. Vann. Satellite observations of long-term changes in tropical cloud and outgoing longwave radiation from 1985 to 1998. *Geophysical Research Letters*, 29(10):37–1, 2002. 11

[114] G. Weber and L. Mervart. Bkg ntrip client (bnc) version 2.9 manual. *Federal Agency for Cartography and Geodesy, Frankfurt, Germany*, 2013. 101

[115] E. Westwater and F. Guiraud. Ground-based microwave radiometric retrieval of precipitable water vapor in the presence of clouds with high liquid content. *Radio Science*, 15(05):947–957, 1980. 60

[116] P. Wielgosz, S. Cellmer, Z. Rzepecka, J. Paziewski, and D. Grejner-Brzezinska. Troposphere modeling for precise gps rapid static positioning in mountainous areas. *Measurement Science and Technology*, 22(4):045101, 2011. 4

[117] K. Woo. Optimum semicodeless carrier-phase tracking of l2. *Navigation*, 47(2):82–99, 2000. 26

[118] V. Wulfmeyer and I. Henning-Müller. The climate station of the university of hohenheim: analyses of air temperature and precipitation time series since 1878. *International Journal of Climatology: A Journal of the Royal Meteorological Society*, 26(1):113–138, 2006. 5

[119] X. Yan, V. Ducrocq, P. Poli, M. Hakam, G. Jaubert, and A. Walpersdorf. Impact of gps zenith delay assimilation on

convective-scale prediction of mediterranean heavy rainfall. *Journal of Geophysical Research: Atmospheres*, 114(D3), 2009. 78

[120] X. Zou, Z. Deng, M. Ge, G. Dick, W. Jiang, and J. Liu. Gps data processing of networks with mixed single-and dual-frequency receivers for deformation monitoring. *Advances in Space Research*, 46(2):130–135, 2010. 5, 109

[121] J. F. Zumberge, M. B. Heflin, D. C. Jefferson, M. M. Watkins, and F. H. Webb. Precise point positioning for the efficient and robust analysis of gps data from large networks. *Journal of geophysical research: solid earth*, 102(B3):5005–5017, 1997. 36, 41, 49, 62, 109

Acknowledgement

"The mind is like a parachute... It only works if we keep it open."
A. Einstein

Foremost, I would like to express my sincere gratitude to my advisor Prof. Mattia Crespi, who firmly believed in my potential. Thank you for the patience, enthusiasm and immense knowledge. I could not have imagined having a better mentor for my PhD.

Besides my advisor, I would like to thank my co-advisors Dr. Stefano Dietrich, Dr. Stefano Federico and Prof. Augusto Mazzoni for their continuous support. Their guidance helped me in all the time of research.

My sincere thanks go to Prof. Fernando Sansò and Prof. Giovanna Venuti for their motivation and knowledge.

I am grateful to GReD group, in particular to Dr. Eugenio Realini and Dr. Andrea Gatti for their fundamental support in the most critical moments. Working with them is not only constructive, but also fun.

Last but not least, I would like to thank AGG (Geodesy and Geomatics Division - Sapienza University of Rome), ISAC (Institute of Atmospheric Sciences and Climate - CNR), INGV (National Institute of Geophysics and Volcanology), DICA (Department of Civil and En-

vironmental Engineering - Politecnico di Milano) and DEIB (Dipartimento di Elettronica, Informazione e Bioingegneria - Politecnico di Milano) groups for their support and availability.

Ringraziamenti

"Eppure il vento soffia ancora,
spruzza l'acqua alle navi sulla prora
e sussurra canzoni tra le foglie,
bacia i fiori li bacia e non li coglie.
Eppure sfiora le campagne,
accarezza sui fianchi le montagne
e scompiglia le donne fra i capelli,
corre a gara in volo con gli uccelli.
Eppure il vento soffia ancora..."

Pierangelo Bertoli – *Eppure soffia*

Confucio una volta ha detto: "Se vedi un affamato non dargli del riso, insegnagli a coltivarlo." Ebbene, il dono più grande che nella vita si possa avere non è la mera conoscenza, ma la capacità di saperla trasmettere agli altri; insegnando così qualcosa che sui libri non si può trovare, qualcosa di molto più prezioso, il valore della pratica e dell'esperienza, l'importanza del saper tramutare in vita reale l'astratto pensiero. È con queste parole che iniziavano le pagine dedicate ai ringraziamenti della mia tesi di Laurea triennale, quello che è stato il primo traguardo di una navigazione intrapresa con vento al traverso; perché se in calma piatta è possibile manovrare a lentissimo moto e ridurre così al minimo la possibilità di fare danni, con vento forte dobbiamo essere più veloci e l'incertezza domina la scena; ma quando ar-

riviamo in mare aperto, con il vento che riempie le nostre vele, ci rendiamo conto che il vero rischio lo avremmo corso rimanendo in porto. È dunque così che inizieranno queste pagine conclusive, con una rincuorante andatura di bolina. Da quel 21 dicembre 2012 molte cose sono successe, ma sicuramente non ho imparato a navigare, anzi... soffro il mal di mare! Una cosa però l'ho capita ed è che ciò che di buono c'è si moltiplica se viene condiviso.

Il primo grazie va pertanto a te Matt, per non avermi dato quella ciotola di riso, per avermi insegnato a coltivarlo e per aver creduto fermamente nelle mie capacità di imparare a farlo. Per le opportunità, il supporto sempre immancabile e le grandi soddisfazioni.

Grazie a te Augh, perché ti fidi. Perché non hai mai tempo, ma poi se ho bisogno il tempo lo trovi. Perché da "ti concedo solo cinque minuti" a "beh allora servo ancora!" il passo è stato breve ed il merito è stato tuo; mi hai insegnato ad osservare l'arte, ad assorbire e come una spugna, al momento giusto, rilasciare.

Grazie a te Stefano, perché lavorare con te ha implicato crescere. Perché abbiamo ipotizzato ricerche ed ottenuto bei risultati. Grazie per il tempo concesso e la valorizzazione di quanto fatto, grazie per le occasioni e le riunioni, perché quando c'è confronto c'è sviluppo.

Grazie a te Stefano F., perché mi hai sempre supportato, incoraggiato e dato fiducia. Perché mi hai fatto imparare tanto e perché i frutti della nostra collaborazione hanno portato grande soddisfazione.

Grazie a te Giovanna per la fiducia e l'autonomia che mi hai concesso, per la voglia di fare e le opportunità di realizzare.

Grazie al Prof. Sansò e ai "ragazzi di GReD", in particolare ad Eugenio ed Andrea per il grande supporto nei momenti più critici. Grazie perché ogni istante diviene occasione di crescita; perché si con-

divide, si sorride e si realizza. Lavorare con voi è un'esperienza che crea dipendenza.

Grazie all'AGG group, per le storie da raccontare e le giornate trascorse insieme, semplicemente perché siamo tutti parte di qualcosa.

Grazie ai gruppi ISAC ed IRET del CNR, in particolare ad Ale, Leo, Claudia, Bruno, Mario e Pier.

Grazie al DICA e al DEIB del Politecnico di Milano, in particolare a Stefano e Lorenzo.

Grazie all'INGV in particolare a Federica per l'immensa disponibilità e gentilezza.

Grazie a tutti coloro che in un modo o nell'altro hanno incrociato il mio cammino in questi anni di Dottorato, perché l'effetto combinato è maggiore della somma dei singoli effetti.

Grazie a Mamma e Papà perché mi sopportano e supportano, perché ci sono sempre, perché non mi fanno mai sentire sola, anche quando sono lontana. Perché mi hanno reso ciò che sono.

Grazie a Gianluca perché è lui e questo già basta. Perché mi rende la vita un'autentica follia. Perché tutto con lui è semplicemente più bello.

Grazie ai miei nonni, che non ci sono più ma mi hanno reso una persona migliore. Grazie a te Nonna perché mi hai insegnato tutto e non mi hai lasciato mai; e come qualcuno una volta ha scritto: "Beato chi ne gode chi del cuore ha il suo custode, Sempre sarai/In un passo stanco, dentro un salto in alto/Che mette i brividi, Per sempre sarai/In un sorriso inaspettato/O in un appuntamento con il mio destino..."

Grazie a Gaia, perché c'è sempre e comunque. Perché non serve essere vicini per volersi bene.

Grazie a tutti i momenti belli e a quelli che lo sono stati meno, alle

lacrime e ai sorrisi, agli abbracci che ti tolgono il respiro, alle nuvole e agli aerei, ai biglietti dei treni e al caos nelle stazioni, al profumo dei libri e alle parole non scritte, allo zaino sempre pronto e alla musica nelle orecchie, ai vecchi amici e ai nuovi, alle videochiamate e alla pizza del mercoledì di Champions; alla vita che corre veloce e si sente tra le dita, sulla pelle come un alito di vento che suscita un brivido intenso. Perché siamo fatti di emozioni, sogni e sentimenti; siamo fatti di istanti.

Ed infine grazie a te, semplicemente per essere sotto il mio stesso cielo. A te che non hai bisogno di parole, ti basta respirare la mia stessa aria.